

# Lawrence Berkeley National Laboratory

## Lawrence Berkeley National Laboratory

### Title

K- p BACKWARD ELASTIC SCATTERING BETWEEN 476 and 1084 MeV/c

### Permalink

<https://escholarship.org/uc/item/6dv248f4>

### Author

Hamilton, R.P.

### Publication Date

1979-09-01

Peer reviewed

$K^-p$  BACKWARD ELASTIC SCATTERING  
BETWEEN 476 AND 1084 MeV/c

Robert Preston Hamilton

Lawrence Berkeley Laboratory  
University of California  
Berkeley, California 94720

September 1979

Abstract

The differential cross-section for  $K^-p$  backward elastic scattering was measured in steps of 10-20 MeV/c between 476 and 1084 MeV/c at the Brookhaven AGS. A negative kaon beam was focused onto a 21 cm long liquid hydrogen target and the forward scattered protons were identified kinematically by means of a single arm magnetic spectrometer. A Monte Carlo computer program aided in the subtraction of background events and in the calculation of correction factors. The new data have an average statistical precision of 2.5% which is an order of magnitude improvement over previous results. Together with a new partial wave analysis, the new data give additional evidence for a resonance between 1700 and 1725 MeV. The best fit to the data finds this to be a  $D_{13}$  resonance with a mass of 1708 MeV and a width of 27 MeV. Comparable improvement in precision was also obtained in a measurement of the differential cross section for  $K^-p \rightarrow \Sigma^- \pi^+$  in which the  $\pi^+$  emerges at  $0^\circ$ .

*47 references*

To my mother  
Henrietta M. Hamilton  
whose dream this was  
a long time ago

## PREFACE

The experiment described in this thesis is a precision measurement of the  $K^-p$  backward elastic scattering cross-section in the resonance region between 476 and 1084 MeV/c incident kaon momentum (1552 and 1833 MeV center of mass energy). It has long been known from pion-nucleon scattering that the  $180^\circ$  differential cross-section is favorable for the observation of resonances. Unfortunately, the corresponding data for the kaon-nucleon system are of low statistics and mainly represent extrapolations to  $180^\circ$  of Legendre polynomial fits to the  $K^-p$  elastic differential cross-section as measured in bubble chambers. The experiment reported here obtained a factor of 10 improvement in statistics and looked at only a small solid angle ( $\sim 45$  msr) near  $180^\circ$ .

Previous electronics experiments designed to study  $K^-p$  backward elastic scattering have not yielded precise data because of the lack of clean, high intensity kaon beams or because their requirement of a signal from both final state particles failed since the backscattered  $K^-$  usually stops in the target. This experiment was performed in the Low Energy Separated Beam (LESB I) at the Brookhaven AGS, which, after separation, produced a  $\pi/K$  ratio of only 10/1. A Čerenkov counter reduced the pion contamination of the incident kaon flux to less than 1%. Only the forward scattered proton was detected kinematically by means of a single arm magnetic spectrometer. As a result, the  $K^-p$  backward elastic cross-section was measured with a statistical precision of better than 3%. The new data show clearly the structure introduced by the previously known  $S = -1$  baryon resonances and, together with a new partial wave analysis of the  $\bar{K}N$  system, provide evidence for a new  $D_{13}$  resonance

between 1700 and 1725 MeV.

The thesis begins with a discussion of the quark model and how it applies to low energy ( $\lesssim 2$  GeV) resonance physics. The basic ideas of the partial wave analysis are also presented. Next is a discussion of previous  $K^-p$  backward scattering experiments and partial wave analyses of the  $\bar{K}N$  system. Section II explains the experimental method while Section III discusses the data analysis. Finally, Section IV presents the results of the experiment and the evidence for a new  $\bar{K}N$   $I=1$  resonance between 1700 and 1725 MeV. In addition, various appendices discuss such details as the theory of diffractive scattering, calibration of the beam momentum, Monte Carlo calculations of background and correction factors, and the on-line computer program. Appendix 6 contains the results of the measurement of the  $K^-p \rightarrow \Sigma^- \pi^+$  differential cross-section for  $\pi^+$ 's emerging at  $0^\circ$  which was conveniently performed with the same apparatus.

### Acknowledgements

The work described here is the result of the efforts of many people. First, I would like to thank Robert Kenney whose guidance and encouragement in completing my thesis was invaluable. I also owe thanks to Professor A. C. Helmholz, my graduate adviser, for useful discussions on both my research and my thesis.

In addition, I appreciate the assistance of the other physicists who helped design, run, and analyze this experiment: Margaret Alston-Garnjost, Dave Pollard, and Robert Tripp from Lawrence Berkeley Laboratory; Don Lazarus from Brookhaven National Laboratory; and Howard Nicholson from Mt. Holyoke College. I am most appreciative of the efforts of Mike Long and Tim Daly who built most of the apparatus used in the experiment. I am also grateful to Sytko Andreae who helped implement the data acquisition computer program.

The experiment described here could not have been performed without the assistance of the Brookhaven AGS staff. Special thanks must go to Dr. T. Kycia for the loan of the Čerenkov counter.

I would like to thank Peggy Fox for typing the manuscript of this thesis and Tim Daly for drawing the figures.

Finally, I would like to thank my parents, Mr. and Mrs. Preston Hamilton, for their special encouragement during my years as a graduate student.

This work was done under the auspices of the High Energy Physics Division of the U.S. Department of Energy (Contract W-7405-ENG-48).

Table of Contents

I. Introduction	
I.1 Introduction	1
I.2 Previous Data	9
I.3 Partial Wave Analyses	12
II. Description of Experiment	
II.1 Experimental Method	15
II.2 Kaon Beam	19
II.3 Liquid Hydrogen Target	25
II.4 Spectrometer	27
II.5 Hodoscope and Time-of-Flight Counters	30
II.6 Electronics	31
II.7 Data Acquisition	39
III. Data Analysis	
III.1 General Approach	46
III.2 Background Subtraction	49
III.3 Corrections	55
III.4 Summary	55
IV. Results and Conclusions	
IV.1 The New Data	61
IV.2 Discussion of Partial Wave Analysis	66
IV.3 Search for New Resonances	66
IV.4 Conclusions	68
Appendix 1 Diffractive Scattering	72
Appendix 2 Momentum Calibration	74
Appendix 3 Details of Monte Carlo Background Determination	77

Appendix 4	Corrections	
A.	Background scattering in target ( $C_7$ )	82
B.	Corrections to beam flux and $K^-$ track length in target	83
C.	Loss of protons	91
Appendix 5	On-line Computer Program	97
Appendix 6	$K^-p \rightarrow \Sigma^- \pi^+$	
A.	General discussion	100
B.	Experimental description	102
C.	Correction factors	102
D.	Background subtraction	105
E.	Results	108
References and Footnotes		113



## I.1 Introduction

One of the most important aims in physics is to explain the properties of matter in terms of the interactions of a small number of elementary particles. With the discovery of the basic constituents of the atom (protons, neutrons, and electrons) and the photon in the first third of this century along with the successful quantum mechanical explanation of atomic structure there was some hope that this goal had finally been achieved. However, the subsequent discoveries of positrons, neutrinos, muons, pions, strange particles, and the many resonant states of the strong interaction have made it apparent that nature is not as simple as it first seemed.

The most perplexing problem has been a fundamental theoretical explanation of the strong interactions of hadronic matter. In the last few years a number of discoveries have led physicists to believe that all hadrons are composed of the more fundamental quarks. There is even some hope that the fundamental dynamical theory of quark interactions has been found - i.e., quantum chromodynamics (QCD). Just as quantum electrodynamics (QED) can quantitatively predict the many energy levels of atoms so must QCD be able to calculate the masses and other quantum numbers of the many hadrons and hadronic resonances.

In the quark model baryons are constructed out of three quarks while mesons are made up of a quark and an anti-quark. All the particles of ordinary hadronic matter consist mainly of up (u) and down (d) quarks.<sup>(1)</sup> For example, the quark composition of the proton is (uud), the neutron (udd), and the  $\pi^+$  ( $u\bar{d}$ ). It is generally assumed that the up and down quarks are degenerate in mass. Since the strong force ignores the

difference in electric charges (the up quark charge is  $\frac{2}{3}e$  and the down  $-\frac{1}{3}e$ ) particles made of these quarks exhibit an SU(2) isospin symmetry.

The strange particles are constructed by substituting an s quark, also of charge  $-\frac{1}{3}e$ , for an up or down quark (e.g.,  $K^-$  is  $(\bar{u}s)$  and  $\Sigma^+$  is  $(uus)$ ). The strange quark is heavier than the up and down quarks and it is considered an isospin singlet so that there does not exist a one-to-one correspondence between ordinary and strange particles. In the approximation where  $m_s = m_u = m_d$  one obtains the SU(3) unitary symmetry of Gell-Mann. (2)

For an atom there exist a number of excited states of the electrons which are bound to the nucleus by the electromagnetic force. It now seems that the many resonant states of hadrons are evidence of a similar situation for quarks bound by the strong force. Unfortunately, because QCD is a strong coupling theory (i.e., while the strength of the electromagnetic force is measured in terms of  $\alpha = \frac{e^2}{\hbar c} = \frac{1}{137}$  the strength of the strong force is determined by  $\alpha_s \sim 1$ ), (3) there does not exist a non-relativistic potential for the strong force analogous to the Coulomb potential which arises from one photon exchange between two charged particles. Consequently, it is not yet possible to calculate the energy levels of hadronic systems. However, a convenient phenomenological classification of strong interaction resonances is provided by the group SU(6) x O(3) which incorporates the SU(3) symmetry of the u, d, and s quarks, the SU(2) spin symmetry of the quarks which are all spin- $\frac{1}{2}$  fermions, and an O(3) symmetry corresponding to harmonic oscillator interquark forces. Within this framework, hadronic particles and resonances are placed in the multiplets of SU(6) x O(3) just as the proton

and neutron are considered members of an  $SU(2)$  doublet and the nucleons,  $\Sigma$ 's and  $\Xi$ 's form an  $SU(3)$  octet. These multiplets are quite large but this scheme does give an idea of how many resonances to allow for in a partial wave analysis as is discussed in Section I.3. For more detail on  $SU(6) \times O(3)$  see the review by Dalitz.<sup>(4)</sup>

Experimentally the resonant states of baryons can be formed by colliding a meson with a nucleon (e.g.,  $\pi p$  or  $K p$  scattering). The anti-quark of the meson annihilates one of the quarks of the nucleon and, if the center of mass energy of the system is at the mass of a resonance, the remaining three quarks are left in some excited state of a baryon which then decays to more stable particles.

Measurements of total, elastic, and inelastic cross-sections as well as angular distributions from both polarized and unpolarized targets provide information on the mass, lifetime, spin, parity and other properties of hadronic resonant states. These quantities have been extensively measured in the case of the pion-nucleon system and provide information on the energy levels of the three-body bound state of the up and down quarks that make up the  $\pi N$  resonances. Kaon nucleon scattering provides the opportunity to study the bound state properties of the strange quarks. Measurements of the  $\bar{K}N$  system are not as complete as for the  $\pi N$  system mainly because of the lack of clean, high intensity kaon beams. The experiment reported in this thesis is one of a series of experiments designed to remedy this situation.

A partial wave analysis provides a convenient way to parameterize the data from these scattering experiments. The differential cross-section for elastic  $K^- p$  scattering may be written<sup>(5,6)</sup>

$$\frac{d\sigma}{d\Omega} = |f(\theta)|^2 + |g(\theta)|^2 \quad (1)$$

where  $f$  and  $g$  are the spin non-flip and spin flip amplitudes respectively. The complex functions  $f$  and  $g$  are expanded in terms of the eigenstates of angular momentum:

$$f(\theta) = \frac{1}{k} \sum_{\ell=0}^L [(\ell+1)T_{\ell+\frac{1}{2}} + \ell T_{\ell-\frac{1}{2}}] P_{\ell}(\cos\theta) \quad (2)$$

$$g(\theta) = \frac{i}{k} \sum_{\ell=0}^L [T_{\ell+\frac{1}{2}} - T_{\ell-\frac{1}{2}}] \sin\theta P'_{\ell}(\cos\theta) \quad (3)$$

$P_{\ell}(\cos\theta)$  = Legendre polynomial of order  $\ell$

$$P'_{\ell}(\cos\theta) = \frac{dP_{\ell}(\cos\theta)}{d(\cos\theta)}$$

$p = \hbar k$  = center of mass momentum of the incident  $K^-$ .

The two partial wave amplitudes,  $T_{\ell \pm \frac{1}{2}}$ , for each orbital angular momentum  $\ell$  take into account the two possible spin orientations of the proton.

The sums do not extend to  $\ell = \infty$  because the finite range,  $R$ , of the strong interaction restricts  $L \lesssim pR/\hbar$ .

Since both the  $K^-$  and the proton are members of isospin doublets, the partial wave amplitudes in Eqs. (2) and (3) are a superposition of two amplitudes corresponding to  $I=0$  and  $I=1$ . For elastic kaon-nucleon scattering the isospin decomposition of the amplitudes is given below:

<u>Reaction</u>	<u>Isospin Amplitude</u>
$K^- p \rightarrow K^- p$	$T_J = \frac{1}{2} (T_{I=1,J}^{\bar{K}N} + T_{I=0,J}^{\bar{K}N})$
$K^- p \rightarrow \bar{K}^0 n$	$T_J = \frac{1}{2} (T_{I=1,J}^{\bar{K}N} - T_{I=0,J}^{\bar{K}N})$

(4)

$$K^- n \rightarrow K^- n \quad T_J = T_{I=1,J}^{\bar{K}N} \quad (4 \text{ cont.})$$

where  $J = \ell \pm \frac{1}{2}$ . Similar formulae exist for the  $T_{IJ}$  that describe the inelastic channels such as  $\Sigma\pi$ ,  $\Lambda\pi$ ,  $\Sigma\eta$ , and  $\Lambda\eta$ . A convenient spectroscopic notation exists for the partial wave amplitudes,  $T_{IJ}$ . The orbital angular momentum,  $L$ , the total angular momentum  $J$ , and the isospin,  $I$ , of the partial wave are written  $L_{I2J}$  for the  $\bar{K}N$  system. The orbital angular momenta are represented by  $S$ ,  $P$ ,  $D$ , etc. for  $L=0, 1, 2, \dots$ . As an example, the  $\Lambda(1520)$  resonance, which is prominent in  $K^-p$  elastic and charge exchange scattering with  $L=2$ ,  $J=3/2$ ,  $I=0$ , is designated  $D_{03}$ .

In a partial wave analysis each complex amplitude  $T_{IJ}$  is parameterized as the sum of non-resonant background and Breit-Wigner resonance terms.<sup>(5,6)</sup> A smoothly varying function of the momentum is chosen for the background term while the Breit-Wigner resonance is given by<sup>(7)</sup>

$$T_R = \frac{\sqrt{\Gamma_i \Gamma_f}}{2(M-E) - i\Gamma} \quad (5)$$

where  $\Gamma_i/\Gamma$  and  $\Gamma_f/\Gamma$  represent the branching ratios of the resonance into the initial and final channels respectively,  $M$  is the mass of the resonance, and  $E$  is the center of mass energy. The total width of the resonance  $\Gamma$  behaves like

$$\Gamma = \Gamma_0 \left(\frac{p}{p_0}\right)^{2L+1} \quad (6)$$

where  $p$  is the center of mass momentum and  $p_0$  and  $\Gamma_0$  are respectively the momentum and width at  $E=M$ . The term  $(p/p_0)^{2L+1}$  is a result of centrifugal barrier effects.

It is instructive to write Eq. (5) as <sup>(5)</sup>

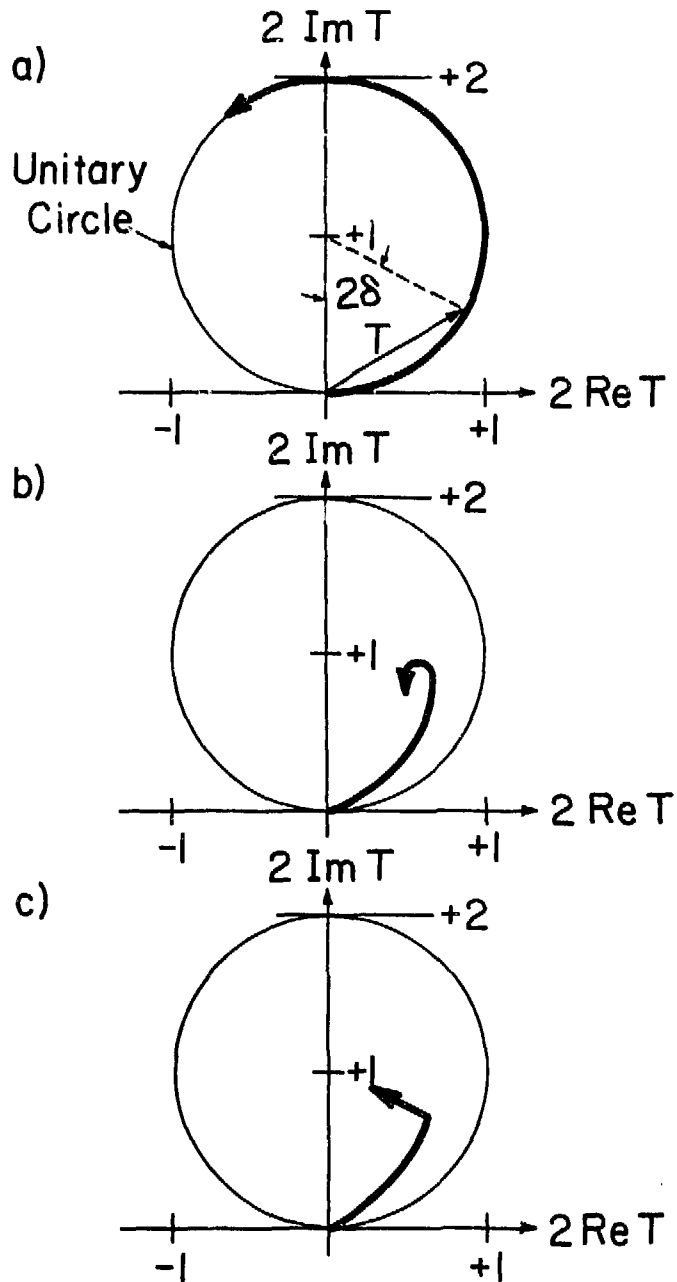
$$T_R = \frac{ne^{2i\delta} - 1}{2i} \quad (7)$$

Then, if only elastic channels are open  $\eta=1$  and

$$\cot \delta = \frac{2(M-E)}{\Gamma} \quad (8)$$

On an Argand plot of  $2 \operatorname{Im}T_R$  versus  $2 \operatorname{Re}T_R$  the resonant amplitude traces out a circle of unit radius. At resonance the phase shift  $\delta$  is  $90^\circ$  and  $|T_R|$  is maximum. From Eq. (8) it is apparent that  $\delta$  increases through  $90^\circ$  quite rapidly near resonance so that, as shown in Fig. 1a, the amplitude  $T_R$  quickly traverses the unit circle in a counterclockwise direction. With the addition of the background amplitude and the fact that  $\eta < 1$  when inelastic channels are open the behavior of the partial wave amplitude on the Argand plot becomes more complicated but a resonance still manifests itself as the rapid counterclockwise turning of the amplitude as the center of mass energy increases through the mass of the resonance (see Fig. 1b). Experimentally one observes either bumps or dips in the cross-section as a function of energy. <sup>(5,6,7)</sup>

In addition to this resonance behavior, the amplitudes  $T_{IJ}$  also exhibit other structure as the threshold energy for a new channel is crossed. Unitarity and the requirement that an amplitude depend analytically on the center of mass energy introduce a singularity in the amplitude which produces a sharp  $90^\circ$  turn to the left in the Argand plot (see Fig. 1c) as the threshold is crossed (see Ref. 8 for an excellent discussion of this behavior). This effect, known as a cusp, may result in a sudden change in the cross-sections for all channels as



XBL 799-11613

Figure 1. Sample Argand plots:

- a) Resonance behavior when only the elastic channel is open (Ref. 7)
- b) Resonance with  $\eta < 1$  (inelastic channels open) superimposed on background amplitude (Ref. 7)
- c) Cusp behavior at a threshold (Refs. 8 and 23)

the threshold is crossed. A procedure which removes this singularity from the analysis and which is useful for studying the behavior of amplitudes close to a threshold is to do the partial wave analysis in terms of a K-matrix which is related to the matrix of T amplitudes used above by:

$$K^{-1} = T^{-1} + i. \quad (9)$$

A detailed discussion of the K-matrix formalism may be found in Refs. 6 and 9.

The above parameterizations of the partial wave amplitudes are fit to the experimental data using formulae such as Eqs. (1-3). Parameters such as the masses and widths of resonances are determined from the  $\chi^2$  minimization techniques used in the fits. In order to satisfy the constraints imposed by unitarity, any complete partial wave analysis should include both elastic and inelastic channels. However, in the  $\bar{K}N$  system the existence of a number of 3-body channels as well as a lack of accurate data on inelastic reactions makes such a multichannel analysis difficult.

As demonstrated in the case of the  $\pi N$  system, measurement of the backward elastic differential cross-section is quite useful in providing evidence for the existence of resonances.<sup>(10)</sup> For  $\theta=180^\circ$  the  $\sin\theta$  term in Eq. (3) causes the spin flip amplitude,  $g(\theta)$ , to vanish. Using Eqs. (1) and (2) the differential cross-section then becomes

$$\frac{d\sigma}{d\Omega}\bigg|_{\theta=180^\circ} = \frac{1}{k^2} \left| \sum_{\ell=0}^L [(\ell+1)T_{\ell+\frac{1}{2}} + \ell T_{\ell-\frac{1}{2}}] (-1)^\ell \right|^2 \quad (10)$$

For the kaon-nucleon system, the existence of a number of inelastic channels makes the amplitudes,  $T_J$ , largely positive imaginary (see Appendix 1). Hence, due to the  $(-1)^\ell$  term in Eq. (10), which comes from



the values of the Legendre polynomials at  $180^\circ$ , the even and odd angular momentum background terms tend to cancel. However, a resonance occurs in only one angular momentum channel and, since the corresponding Legendre polynomial assumes its maximum absolute value of unity, the resonance should appear prominently in the cross-section. From Eq. (5) it is clear that the resonance amplitude,  $T_R$ , is positive imaginary at resonance ( $E=M$ ). Hence, a resonance of even parity, whose amplitude adds constructively to the background, will cause an enhancement in  $\frac{d\sigma}{d\Omega}$  while a resonance of odd parity will cause a depression. The experiment described here was designed to obtain more precise information on the  $K^-p$  backward elastic cross-section in order to more clearly establish the resonant states of the  $\bar{K}N$  system.

### 1.2 Previous Data

Since  $K^-p$  scattering is mainly diffractive (see Appendix 1), most of the elastic cross-section is strongly peaked in the forward direction with the result that the backward scattering cross-section is an order of magnitude less than the forward scattering cross-section. The results of previous measurements of  $\frac{d\sigma}{d\Omega}_{\theta=180^\circ}(K^-p \rightarrow K^-p)$  are shown in Fig. 2. The rather poor statistical accuracy is due to the lack of high intensity  $K^-$  beams coupled with the small cross-section, typically less than 2 mb/sr.

Most of the data in this energy region (1550-1900 MeV in the center of mass) come from bubble chamber experiments, of which the most extensive is that of the CERN-Heidelberg-Saclay (CHS) collaboration. They studied a number of  $K^-p$  final states in two experiments, one covering the momentum region from 436 MeV/c to 793 MeV/c, the other from 777 MeV/c to 1226 MeV/c. At lower momenta the data are those of Armenteros

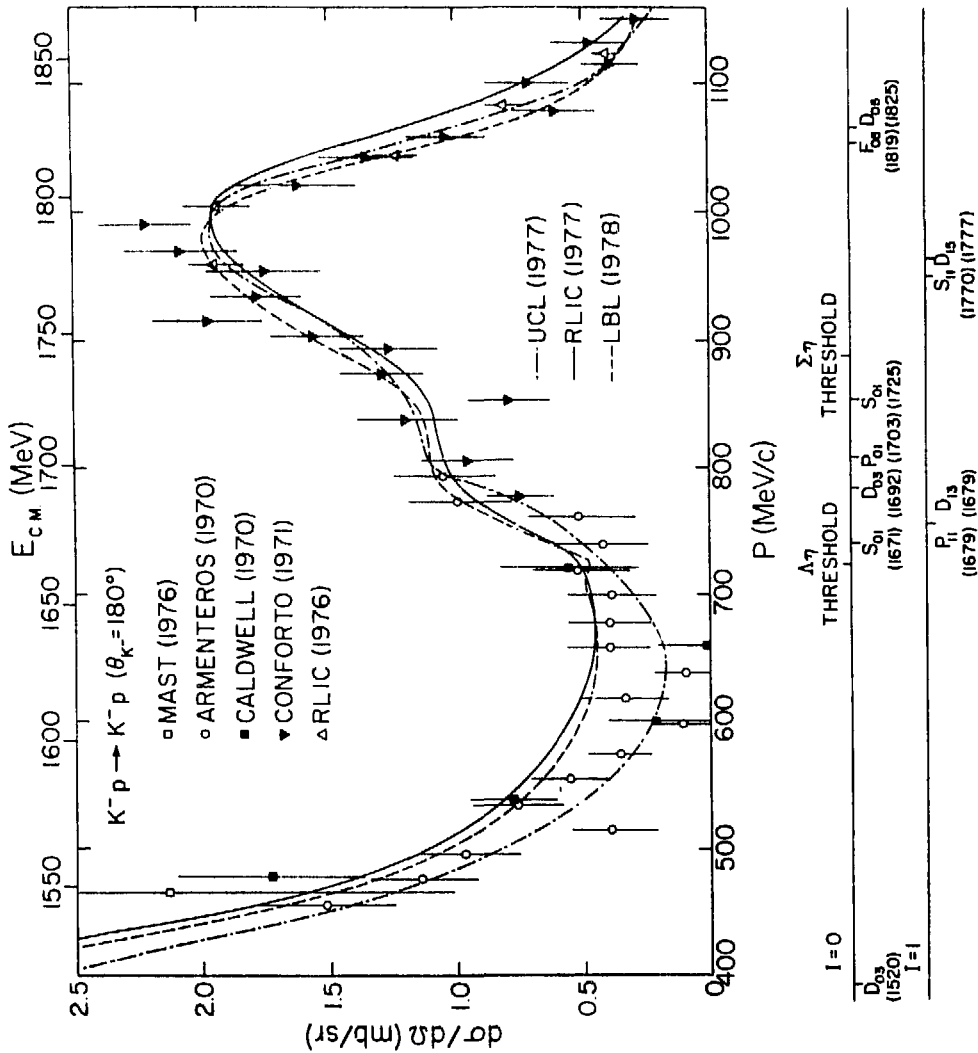


Figure 2. Measurements of  $\frac{d\sigma}{d\Omega} (\theta=180^\circ)$  for  $K^- p \rightarrow K^- p$  (Refs. 11-13, 16,18), and fits to the data by three partial wave analyses (Refs. 9,21-23)

(1970),<sup>(11)</sup> while the higher momentum data were analyzed by a Chicago-Heidelberg (CH) collaboration, Conforto (1971).<sup>(12)</sup> Both sets of data represent extrapolations of Legendre polynomial fits to the measured differential cross-sections to  $\theta=180^\circ$  with an average statistical accuracy of 40% at the lower momenta and 20% at the higher momenta.

The most recent measurement of the  $K^-p$  elastic differential cross-section, a Rutherford Laboratory - Imperial College Collaboration, is a bubble chamber study of eleven incident  $K^-$  momenta between 960 and 1355 MeV/c (RLIC (1976)).<sup>(13)</sup> Again, the data presented in Fig. 2 are extrapolations to  $180^\circ$  with roughly 10% statistical errors.

Electronic experiments have not been very successful in measuring the  $K^-p$  backward elastic cross-section. At incident  $K^-$  momenta less than 1 GeV/c the backscattered kaon is moving so slowly that it stops in the target and either escapes detection entirely or produces  $\pi$ 's or  $\mu$ 's (through decays or nuclear interactions) that misidentify the event. As a result, spark chamber studies of the differential cross-section have been restricted to center of mass angles less than  $160^\circ$  by their requirement of a coincidence between both the proton and the scattered kaon.<sup>(14,15)</sup> The only data from a counter experiment shown in Fig. 2, Caldwell (1976),<sup>(16)</sup> are the results of an Arizona experiment at the Bevatron that identified only the forward scattered proton using a time-of-flight technique. Their data represent only 25% statistical accuracy due to low incident  $K^-$  flux.

With such low statistics only the gross features of the kaon-nucleon system are apparent in Fig. 2. The steeply falling cross-section at lower momenta is the high energy tail of the prominent  $\Lambda(1520)$  resonance.

Between 700 and 900 MeV/c the cross-section begins to rise again as a number of inelastic channels, such as  $\Lambda\eta$  and  $\Sigma\eta$ , open up. The cross-section peaks around 1000 MeV/c due to the presence of a number of resonances including the  $\Sigma(1770)$  and  $\Sigma(1777)$  and the  $\Lambda(1819)$  and  $\Lambda(1825)$ . The experiment reported in this thesis reveals the structure of the backward elastic cross-section in considerably more detail.

### 1.3 Partial Wave Analyses

There exist a number of partial wave analyses of the  $\bar{K}N$  system. However, none of these analyses is as complete as those of the  $\pi N$  system. The lack of accurate data covering a large energy range, in particular data on inelastic channels or on the scattering of kaons from polarized targets, makes an energy independent analysis extremely difficult. Also, the existence of a number of inelastic channels in  $\bar{K}N$  scattering, especially those containing three or more particles ( $\Lambda\pi\pi$ ,  $\Sigma\pi\pi$ , etc.), complicates any multichannel analysis, which is the only way to take full advantage of the constraints imposed by unitarity.

Recently, several high statistics bubble chamber<sup>(17,18)</sup> and electronics experiments, including a precision measurement of the charge exchange partial<sup>(19)</sup> and differential cross-sections,<sup>(20)</sup> have improved this situation somewhat. There are three partial wave analyses that incorporate at least some of these new data.<sup>(9,21,22,23)</sup> Their fits to the backward elastic cross-section are shown in Fig. 2.

The Rutherford Laboratory-Imperial College collaboration (RLIC)<sup>(21)</sup> have made an energy-dependent analysis that covers the energy range between 1480 and 2170 MeV. However, they did not include the charge exchange data which only became available afterwards. They took the

usual approach of modeling the partial wave amplitudes as the sum of a smoothly varying background term and one or more non-relativistic Breit-Wigner resonance terms. Each channel,  $\bar{K}N$ ,  $\Sigma\pi$ , and  $\Lambda\pi$ , was fitted separately to determine the parameters of the resonances. Then, as required by unitarity, the mass and width of each resonance were constrained to the same values in each channel (i.e., a weighted average of the values from all three channels for  $I=1$  resonances and from the  $\bar{K}N$  and  $\Sigma\pi$  channels for  $I=0$  resonances) and the background terms were allowed to vary to obtain a best fit.

The University College London analysis (UCL)<sup>9,22</sup> is a multi-channel energy-dependent partial wave analysis covering 1.54 to  $\sim 2$  GeV. In order to realize the constraints imposed by unitarity the data were fit with a parameterized K-matrix. Resonances were then identified with poles in the K-matrix. In addition to the usual two-body channels,  $\bar{K}N$ ,  $\Sigma\pi$ , and  $\Lambda\pi$ , a fourth channel was made available to accommodate all other inelastic channels including  $\Lambda\eta$  and  $\Sigma\eta$ . This analysis is an extension of a previous one<sup>(24)</sup> but incorporated a number of changes to eliminate the unphysical predictions of the earlier one. In particular, the S-wave dependence of the all inclusive inelastic channel on the  $\eta$  momentum was analytically continued below the  $\Lambda\eta$  and  $\Sigma\eta$  thresholds where the  $\eta$  momentum becomes imaginary. This simulated the cusp-like behavior of the amplitudes at these thresholds. Also, enough freedom was allowed in the fitting program to accommodate those resonances allowed by minimal  $SU(6) \times O(3)$ . However, low energy polarization data are not fit well by this analysis, possibly because recently published low energy bubble chamber<sup>(18)</sup> and polarization data<sup>(25)</sup> were not included.

The most recent analysis is a single channel energy-dependent partial wave analysis of the  $\bar{K}N$  system from 1507 to 1941 MeV by M. Alston-Garnjost et al., (LBL).<sup>(23)</sup> All recent  $K^-p \rightarrow \bar{K}N$  data were included in the fit. Cusps in the S-wave amplitudes were modeled by including an  $\eta$  momentum dependent term in the total widths of the resonances at the  $\Lambda\eta$  and  $\Sigma\eta$  thresholds. An extension of this analysis incorporates the backward elastic data reported in this thesis and is discussed in more detail in Section IV.

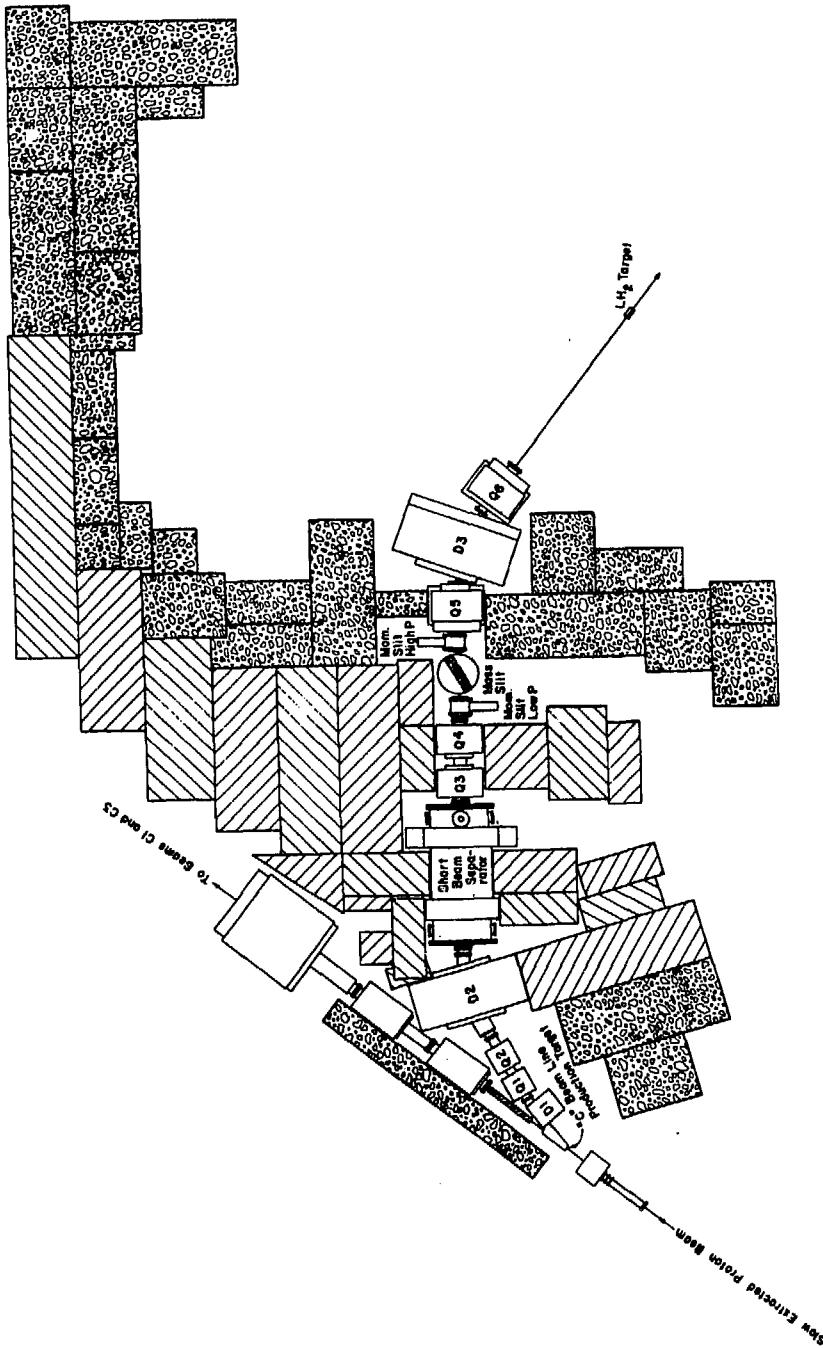
## II. DESCRIPTION OF EXPERIMENT

### II.1 Experimental method

The experiment described in this thesis is a high statistics measurement of the  $K^-p$  backward elastic cross-section between 476 and 1084 MeV/c incident kaon momenta (1552 and 1833 MeV center of mass energy). With the same apparatus we were able to measure the differential cross-section for the reaction  $K^-p \rightarrow \Sigma^- \pi^+$  where the  $\pi^+$  emerges at  $0^\circ$  (see Appendix 6). As mentioned before, two problems have precluded a precision measurement of the  $K^-p$  backward cross-section: the lack of clean, high intensity  $K^-$  beams and the inability to detect the backscattered  $K^-$ , which usually stops in the target, if a two particle ( $K^-$  and  $p$ ) final state trigger is required. In this experiment, the high flux of kaons available from the Low Energy Separated Beam (LESB I) at the Brookhaven AGS made it possible to obtain an average statistical precision of 2.5% in the  $180^\circ$  cross-section, more than a factor of ten improvement over previous results. Also, by identifying only the forward scattered proton with a single arm magnetic spectrometer, the problems associated with detecting the  $180^\circ$   $K^-$  were avoided.

The experiment was performed in the momentum recombined (C4) branch of LESB I which is shown in Fig. 3. The beam, which was designed by Dr. J. Fox<sup>(26,27,28)</sup> and tested by the Kycia Group<sup>(29,30)</sup> at Brookhaven, used an electrostatic separator and a mass slit to reduce the  $\pi/K$  ratio to 10/1 at most momenta. A Čerenkov counter then differentiated between pions and kaons so that the level of pion contamination in the incident kaon flux was typically much less than 1%.

A good incident beam particle was defined by a coincidence of the

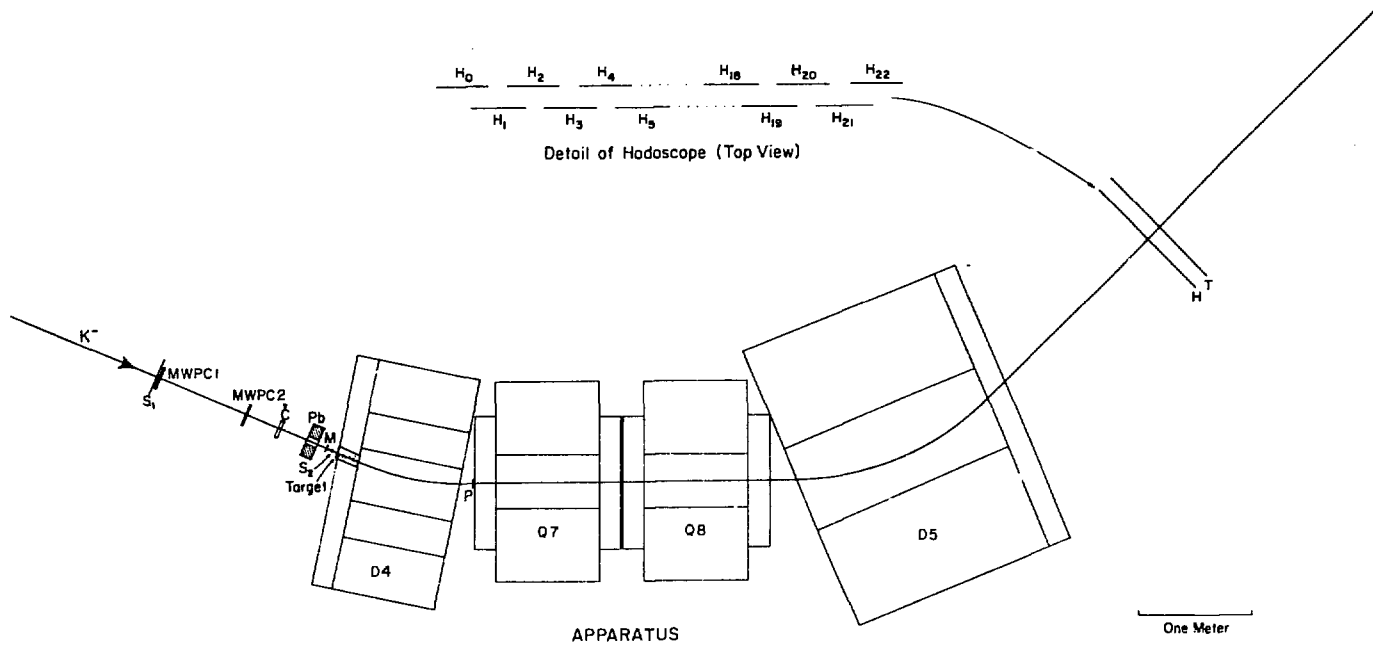


C4 BEAM LINE

Figure 3



Figure 4



XBL 799-11641

three scintillation counters shown in Fig. 4: S1, an anti-counter which served to eliminate any beam halo; M, which set the timing for the electronics; and S2, a three element hodoscope which aided in centering the beam on the target. The momentum resolution of the beam was monitored by two multi-wire proportional chambers (designated MWPC 1 and 2 in Fig. 4) and found to have  $\Delta p/p \sim 2.5\%$  (FWHM).<sup>(31)</sup>

The kaon beam was focused at the center of a 21 cm liquid hydrogen target and the forward scattered protons were detected by means of the single arm spectrometer and scintillator hodoscope arrangement shown schematically in Fig. 4. The first bending magnet, D4, swept away the negatively charged kaons; the two quadrupoles, Q7 and Q8, focused the forward scattered protons on the hodoscope, H; and the last bending magnet, D5, provided the final momentum dispersion of the protons at the hodoscope. At the exit of D4 a scintillation counter, P, mainly determined the solid angle acceptance for the differential cross-section to be 9.8 msr in the laboratory frame.

Immediately in the shadow of the hodoscope, three overlapped timing counters, T, discriminated against all final state particles except protons on the basis of the time between the arrival of a  $K^-$  at M and the detection of a secondary at T. Thus the only background events on the hodoscope would be from protons that did not come from backward  $K^-p$  scatters but instead from inelastic reactions, such as  $K^-p \rightarrow \Lambda\pi$  with the resulting decay  $\Lambda \rightarrow p\pi^-$ , or from wide angle scattered protons that managed to find paths to the hodoscope other than along the spectrometer central ray. The momentum acceptance of the hodoscope was made considerably larger than the momentum bite spanned by protons from backward elastic  $K^-p$  events in order to allow an accurate determination of this

background.

The information from a proton event detected by the hodoscope was fed into appropriate CAMAC<sup>(32)</sup> modules which were then read by a PDP 11/34 computer (see Appendix 5). The raw information from CAMAC was first put into more manageable form before being written to tape. In addition, the computer program provided on-line monitoring of various aspects of the experiment including histogram displays of the distribution of events on the hodoscope.

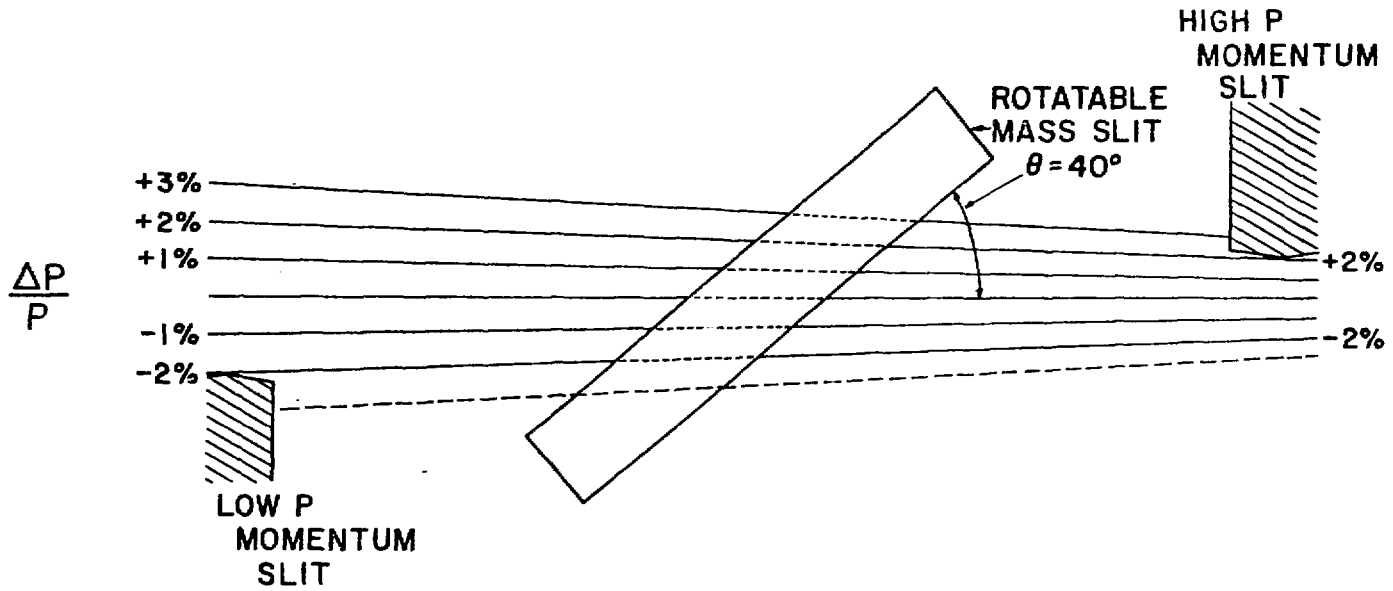
## II.2 Kaon Beam

The C4 beam line at the Brookhaven AGS is shown in detail in Fig. 3. Since complete quantitative descriptions of LESB I may be found elsewhere<sup>(26-30,33)</sup> only the more important features of the beam line will be discussed here.

A variety of secondary particles, including pions, kaons, and anti-protons, were made by illuminating the 4/5 interaction length "C" beam line production target (platinum, 76.2 mm thick, 5.08 mm high, and 2.54 mm wide) with  $\sim 2 \times 10^{12}$  protons per pulse of the AGS slow extracted beam (SEB) at 29.4 GeV/c. Those particles emitted at 10.5 degrees were deflected an additional 11.5 degrees from the primary proton beam by the first bending magnet, D1. The quadrupole doublet, Q1 and Q2 provided a beam that was slightly converging in the vertical dimension at the electrostatic separator. Before the beam entered the separator, the bending magnet D2 made the primary momentum determination and produced a momentum dispersed image of the production target for the momentum slits (see Figs. 3 and 5).

The second quadrupole doublet, Q3 and Q4, focused the beam at the

Figure 5



MOMENTUM STOPS AND MASS SLIT FROM ABOVE

XBL 799-11623

mass slit. Since low momentum particles came to a focus upstream of the high momentum particles, the mass slit was rotated by 40 degrees with respect to the beam axis as shown in Fig. 5. With the electric field in the separator at 50 kV/cm (54 kV/cm for momenta above 890 MeV/c) the magnetic field was tuned so that kaons passed undeflected through the 0.4 cm vertical gap in the mass slit. This reduced the  $\pi/K$  ratio in the beam at the  $LH_2$  target to less than 10/1 at most momenta. After leaving the mass slit the beam was then focused and centered on the hydrogen target by the quadrupole doublet, Q5 and Q6, and the bending magnet, D3.

The currents used in the magnets of the C4 beam line were determined from information available from other experiments that had used LESB I (in particular, the  $K^-p$  charge exchange study<sup>(33)</sup>). It was found necessary to tune only three magnets in going from one momentum to the next. The quadrupole, Q3, which focused vertically on the 10 cm separator gap was adjusted to give maximum kaon flux; the beam separator magnetic field was fine tuned to maximize the number of beam kaons; and, finally, the current in D3 was varied to center the beam on the target. The position of the beam at the target was monitored in the horizontal dimension by the hodoscope counter  $S_2$ , consisting of three vertical 1.27 cm wide scintillator elements, and in the vertical dimension by a hodoscope, consisting of five horizontal 1.27 cm wide scintillator fingers, which was taken out of the beam during data-taking.

As mentioned before, a good incident beam particle was required to pass through the aperture of the  $S_1$  beam halo counter, through M, and through  $S_2$ . The dimensions and locations of these counters, as well as of other scintillation counters used in this experiment, are given in

Table I  
Counter and Wire Chamber Dimensions

a) Scintillation counters

Counter	Thickness (cm)	Width (cm)	Height (cm)	Distance from target centerline *
S <sub>1</sub>	0.32	15.24	2.54	-158.4
M	0.32	10.16	5.08	-22.9
S <sub>2</sub>	0.32	3.81	3.18	-15.2
P	0.32	7.62	25.40	140.4
H	0.32	59.69	30.48	814.3

b) Wire chambers

Aperture (w x h)	28.0 cm x 8.0 cm
Number of wires	96
Wire spacing	2 mm
Wire diameter	20 $\mu$ (gold plated tungsten)
Distances from target centerline *	
Upstream chamber	-180 cm
Downstream chamber	- 97 cm

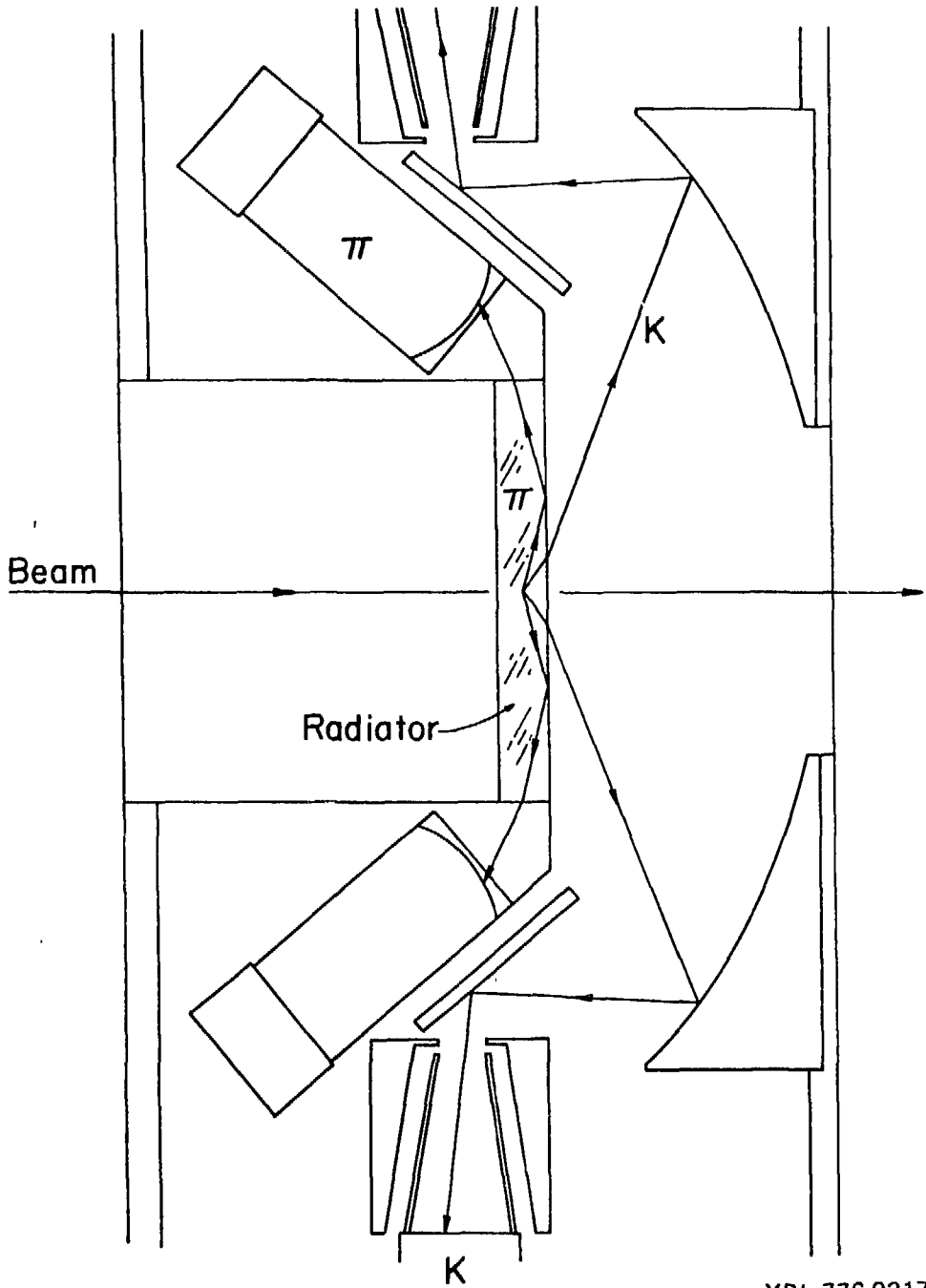
\* A negative distance means that the counter was located upstream of the target.

Table Ia. Table Ib lists the dimensions of the wire chambers which monitored the beam profile and momentum spread.

Beam  $\pi$ 's and  $\mu$ 's were then distinguished from beam  $K^-$ 's by means of the Čerenkov counter shown schematically in Fig. 6.<sup>(34)</sup> Because of their greater velocity,  $\pi$ 's and  $\mu$ 's gave off Čerenkov radiation at a larger angle with respect to the beam axis than did  $K^-$ 's of the same momentum. The Čerenkov cells were chosen with indices of refraction such that pion Čerenkov light was internally reflected at the cell surface into the " $\pi$ " phototubes, while kaon Čerenkov light, which exited the cell, was focused by an annular spherical mirror onto the "K" phototubes. This allowed both a positive identification of  $K^-$ 's and a veto of  $\pi$ 's and  $\mu$ 's. (A more detailed description of the Čerenkov counter may be found in Ref. 33.) As explained in Appendix 4.B.1, the Čerenkov counter reduced the  $\pi$  and  $\mu$  contamination of the incident  $K^-$  flux to much less than 1% at most momenta. At the lowest momentum, 476 MeV/c, the contamination was only 2%.

In order to study as small a solid angle as possible at  $180^\circ$  for  $K^-p \rightarrow K^-p$  it was necessary that both the beam spot size and its convergence be small at the target. The three beam defining counters,  $S_1$ ,  $M$ , and  $S_2$ , limited the horizontal convergence of the beam at the target to 66 mr and the vertical to 20 mr. In fact, the wire chamber information showed the horizontal convergence to be less than 40 mr and the horizontal beam dimension to be less than 4.5 cm at the target. The vertical beam profile hodoscope described above yields a vertical beam dimension of less than 2 cm at the target center.

In addition to the apparatus required for defining the kaon beam it was necessary to place a 10.16 cm thick lead collimator with a  $10.16 \times 5.08$  cm



XBL 776-9217

Figure 6. Čerenkov counter schematic



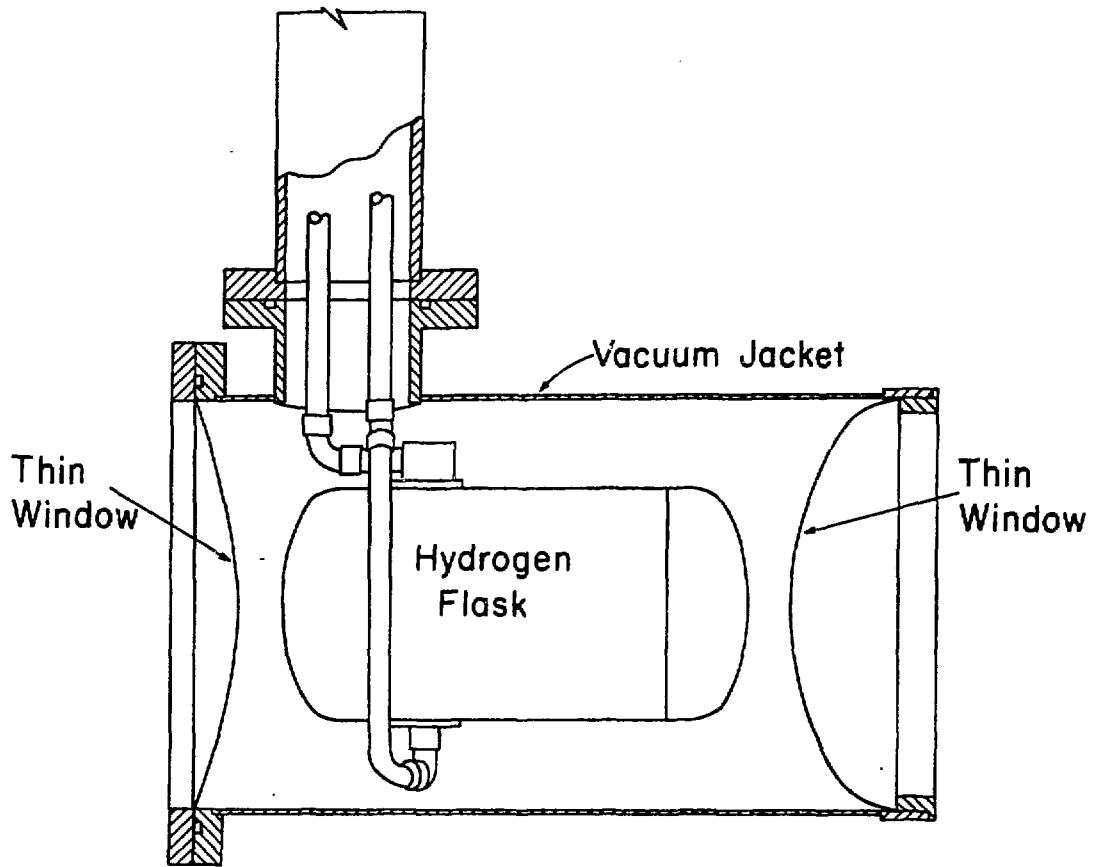
hole for beam passage upstream of the target between the Čerenkov counter and the M counter. Without the lead wall it was possible for backscattered kaons or their charged decay products to enter the Čerenkov counter, produce Čerenkov light that was internally reflected by the cell, and thus activate the pion veto. Hence, the very events the experiment was designed to detect could veto themselves. Most of the particles that went straight back through the small hole in the lead also had to pass through M thereby greatly increasing the pulse height of the output of the M phototube. A high threshold discriminator circuit, described in Section II.6, prevented false vetos of good events by these particles. Monte Carlo calculations (see Appendix 4.C.3) showed that, as a result of the combined effect of the lead wall and the high threshold M counter veto circuit, less than 0.1% of all backward elastic  $K^-p$  events vetoed themselves.

The momentum of the beam was calibrated by a time-of-flight method described in Appendix 2. The results of this calibration are consistent with values obtained by subtracting  $dp/dx$  losses in material upstream of the liquid hydrogen target from the tuned value of the  $K^-$  momentum at the mass slit. All beam momentum values used in this thesis are the mean interaction momentum of the  $K^-$  in the hydrogen target calculated as described above.

### II.3. Liquid Hydrogen Target

The liquid hydrogen target used in this experiment is shown schematically in Fig. 7. The cylindrical Mylar flask, which contained the liquid hydrogen was 20.96 cm long and 10.16 cm in diameter with walls 0.178 mm thick and endcaps 0.089 mm thick. The endcaps were enclosed by

Figure 7



TARGET SIDE VIEW

XBL 799-11640

20 layers of 6.35  $\mu$  aluminized Mylar insulation. The whole assembly was located inside a cylindrical aluminum vacuum jacket with a 0.190 mm Mylar window at the upstream end and a 0.089 mm thick Mylar window at the downstream end. X-ray photographs, taken with the target filled with liquid nitrogen, permitted a measurement of the target's axial length and the curvature of its endcaps while the target was cold.

The average pressure in the hydrogen target when it was full was 1.109 atm, which gives a liquid parahydrogen density of 0.0704 g/cc.<sup>(35)</sup> When the target was empty, residual hydrogen gas contributed 0.0004 g/cc, leaving a net density of 0.070 g/cc.

#### II.4. Spectrometer

Figure 4 shows the layout of the single arm spectrometer used to momentum analyze the protons from backward elastic  $K^-p$  collisions. The first element of the spectrometer, D4, an 18D36 dipole magnet located immediately downstream of the hydrogen target, served mainly to sweep away the negatively charged kaon beam. This bending magnet was 91.44 cm long, 45.72 cm wide, and gapped to 25.4 cm to give a maximum  $\int B \cdot d\ell$  of 2.4 Tesla-meters.

The solid angle acceptance was defined by a thin (0.32 cm) scintillation counter (P), 25.4 cm high, 7.62 cm wide and located 140.36 cm (as measured along the spectrometer central ray) downstream of the hydrogen target center (just upstream of Q7). The acceptance of the P counter was thus 54 mr horizontally and 179 mr vertically or 9.78 msr of solid angle. To maximize the counting rate the P counter was made slightly larger than the geometric acceptance of the spectrometer magnet apertures. Monte Carlo calculations described in Appendix 4.C.1 found

this to be a momentum dependent effect that made the true angle acceptance less than that determined by the P counter by 4-6%. Since the P counter was located between magnets D4 and Q7, each of its two equal area segments was placed at the end of a long lucite light pipe to keep the phototubes, already encased in iron shielding, in regions of low magnetic field. The horizontal division of the counter into two pieces aided in monitoring the vertical positions of the scattered protons.

The next two elements of the spectrometer, Q7 and Q8, formed a quadrupole doublet which focused the forward scattered protons on the hodoscope. Both quadrupoles were 18Q36 magnets, 91.44 cm long with a 45.72 cm diameter bore and a maximum field gradient of 5.12 Tesla/meter. Q7, a vertically focusing magnet, was placed upstream of Q8, a vertically defocusing element, to provide the maximum lever arm for squeezing the secondary proton beam through the narrow vertical gap of the D5 magnet. The resulting vertical and horizontal foci were 50.8 and 152.4 cm respectively downstream of the exit of D5. The final magnet, D5, a 36D72 bending magnet (182.9 cm long, 91.44 cm wide, and gapped to 20.3 cm for a maximum  $\int B \cdot dl$  of 4.0 Tesla-meters), produced a momentum dispersed image of the target at the hodoscope.

The spectrometer magnets were tuned by reversing the currents in each magnet and allowing the incident kaon beam to pass through to the hodoscope. Measurements of the fields in each magnet showed that any asymmetries associated with hysteresis effects in reversing the magnet currents were small. A matrix describing the transport of a proton from the target to the hodoscope was calculated with the beam optics program

Table II

Transformation matrix of spectrometer from target to focus.

The vector, labeled  $x$ ,  $\theta_x$ ,  $y$ ,  $\theta_y$ ,  $\frac{\Delta P}{P}$ , is in units of cm, msr, and per cent.

-0.649	0	0	0	-2.19
-7.28	-1.54	0	0	0
0	0	-3.88	0	0
0	0	-3.50	-0.284	0
0	0	0	0	1

TRANSPORT<sup>(36)</sup> and is presented in Table II.

Virtually all of the empty target events in this experiment were produced in the hydrogenous materials upstream of the target. When the target was full, these protons lost energy in traversing the liquid hydrogen. If the same spectrometer settings were used for an empty target run, such particles, which would then have somewhat higher momenta on entering the spectrometer, would hit the hodoscope at a different position than in a target full run. To allow a channel by channel subtraction of empty target events from the hodoscope distributions the spectrometer currents were set 1-5% higher (depending on the momentum) on empty target runs.

#### II.5. Hodoscope and Time-of-Flight Counters

The spectrometer produced a momentum dispersed image of forward scattered protons at the final hodoscope, H, shown in detail on Fig. 4 and located 814 cm downstream of the hydrogen target center. The hodoscope was made up of 23 scintillator elements each 30.48 cm high, 3.81 cm wide, and viewed by an RCA 8575 2" phototube. Nearest neighbor elements overlapped by 1.27 cm to give 43 channels 1.27 cm wide and two outside channels 2.54 cm wide. The momentum dispersed image of elastically scattered protons was about 13 cm wide, 20 cm high, and centered on the hodoscope while the total  $\Delta p/p$  acceptance of the hodoscope was  $\pm 13.6\%$ .

The time-of-flight array (T) consisted of two counters each 59.7 cm wide and 15.24 cm high placed immediately downstream of the hodoscope. The shadow of the hodoscope was completely contained within the boundaries of these two counters so that any particle accepted by the

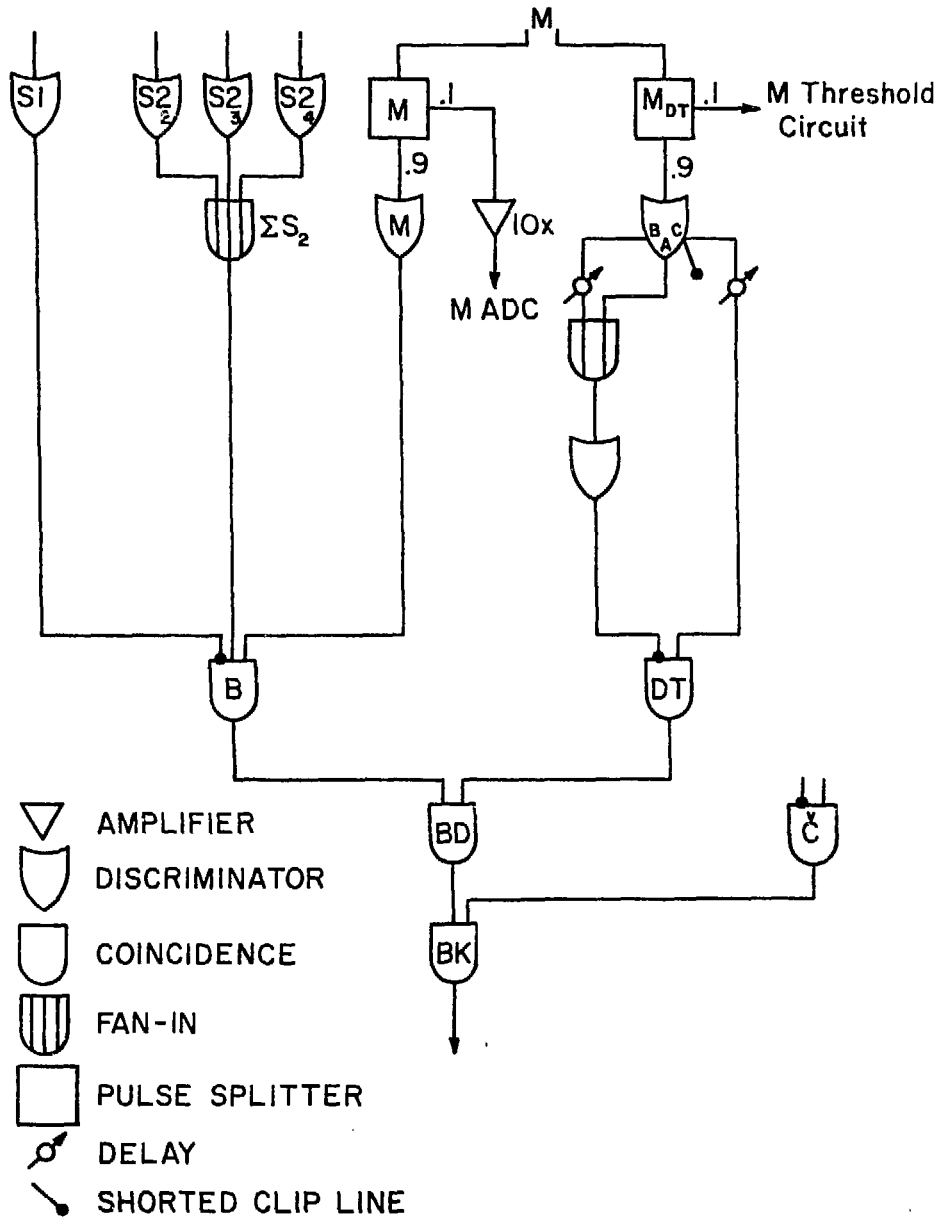
spectrometer that hit the hodoscope also hit one of these two timing counters. A third counter, of the same dimensions, was vertically centered on the junction of the two primary TOF counters and was used for positional tagging. The resulting combination of these three counters divided the vertical region of the hodoscope into 4 channels each 7.62 cm high. The total flight path for the TOF system was 8.5 meters, and the inclusion of cuts on the particle TOF in the electronics resulted in a substantial reduction in the trigger rate due to unwanted particles from background reactions (see Section II.6).

#### II.6. Electronics

The scintillation counters used in this experiment were viewed by RCA 8575 two-inch phototubes. The high voltages on each tube were set so that a normally incident minimum ionizing particle produced a 300 mV signal at the input to that phototube's discriminator. The discriminator thresholds were adjusted to 100 mV (1/3 the minimum ionizing pulse height).

Figure 8 is a schematic of the beam definition electronics. A signal in the S1 beam halo counter vetoed any M · S2 coincidences so that a good incident beam particle was defined by  $B = \overline{S1} \cdot M \cdot S2$ . The RCA 8575 tube on M was chosen for low noise and good pulse height to provide a stable signal to set the timing for most of the fast logic chain. The singles counts on each of the three elements of the S2 hodoscope were scaled to provide an on-line histogram display of the horizontal beam profile at the target.

To provide sufficient time for the wire chambers to recover from the passage of a charged particle, no two beam particles were accepted within 65 ns of each other. This was accomplished by means of the dead time



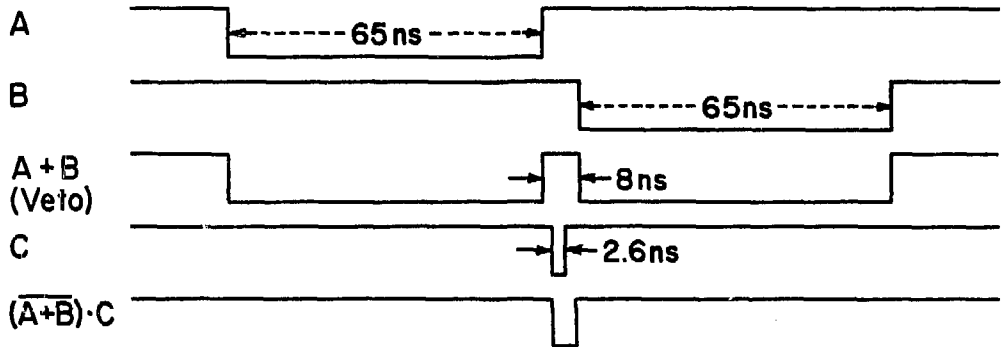
## BEAM DEFINITION ELECTRONICS

XBL 799-11618

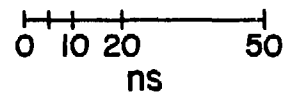
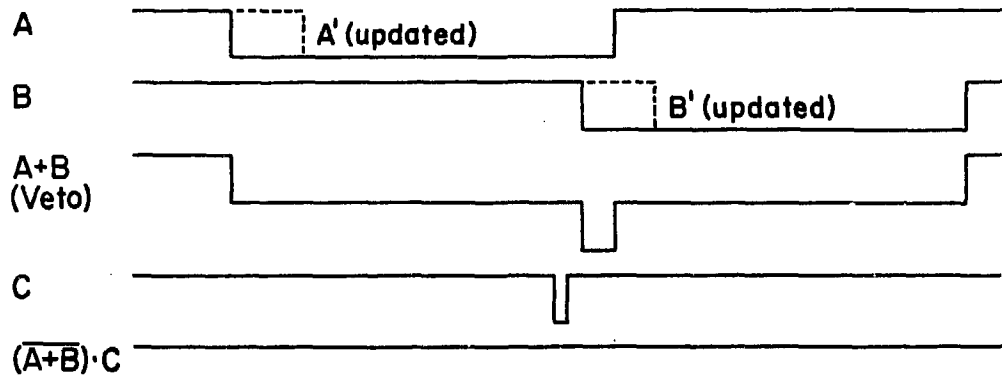
Figure 8



a) No particles within 65 ns.



b) Two particles within 65 ns.

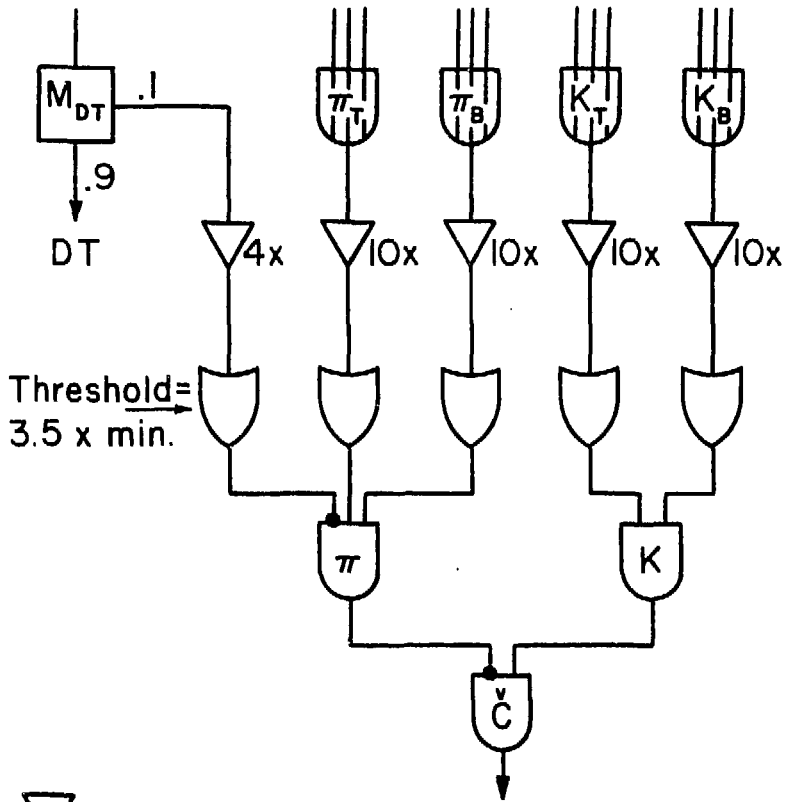


XBL 799-11619






Figure 9. Timing diagram for BD

circuit, DT, shown in Fig. 8; the timing diagram for the DT coincidences is shown in Fig. 9. Ninety per cent of the  $M_{DT}$  signal was fed into a MECL III updating discriminator with three outputs: one with a 1.3 ns shorted clip to yield a sharp 2.6 ns pulse and the other two with 65 ns output widths. One of the longer signals was delayed 73 ns with respect to the other and added passively to it to produce a veto signal at the input of DT. If no other beam particle arrived within 65 ns of the first, the shorter signal would produce an output at DT during the 8 ns the veto was off and thus establish a coincidence at BD. A particle arriving sooner than 65 ns after another produced an updated veto signal that closed the 8 ns gap in the early veto signal and thus produced no output at DT and no coincidence at BD (see Fig. 9). Of course, two particles coming within 8 ns of each other would be counted as one at BD, but, since the rates at B were less than 1.5 MHz this effect amounted to less than 1.2% of the BD coincidences. The effect on the more important kaon flux coincidence, BK (see below), was negligible since the  $\pi/K$  ratio in the beam was at least 10/1. Thus, if an incident kaon was accompanied by another particle within 8 ns that particle was most likely a  $\pi$ . Since the  $\chi$  Cerenkov counter eliminated more than 99% of all  $\pi$ 's from BK (see Appendix 4.B.1) this reduced the probability that a count in BK consisted of a K and a  $\pi$  within 8 ns of each other to less than 0.01%.

The rate independent coincidences, BD, contained both  $\pi^-$  and  $K^-$  signals. The  $\chi$  Cerenkov counter electronics shown in Fig. 10 vetoed essentially all beam pions (see Appendix 4.B.1). The outputs of the  $\chi$  Cerenkov counter " $\pi$ " phototubes were added actively to produce the coincidence  $\pi$  in the logic diagram (Fig. 10), as were the outputs of the



Threshold =  
3.5 x min.

-  AMPLIFIER
-  DISCRIMINATOR
-  COINCIDENCE
-  FAN-IN
-  PULSE SPLITTER

# ČERENKOV COUNTER ELECTRONICS

XBL 799-11620

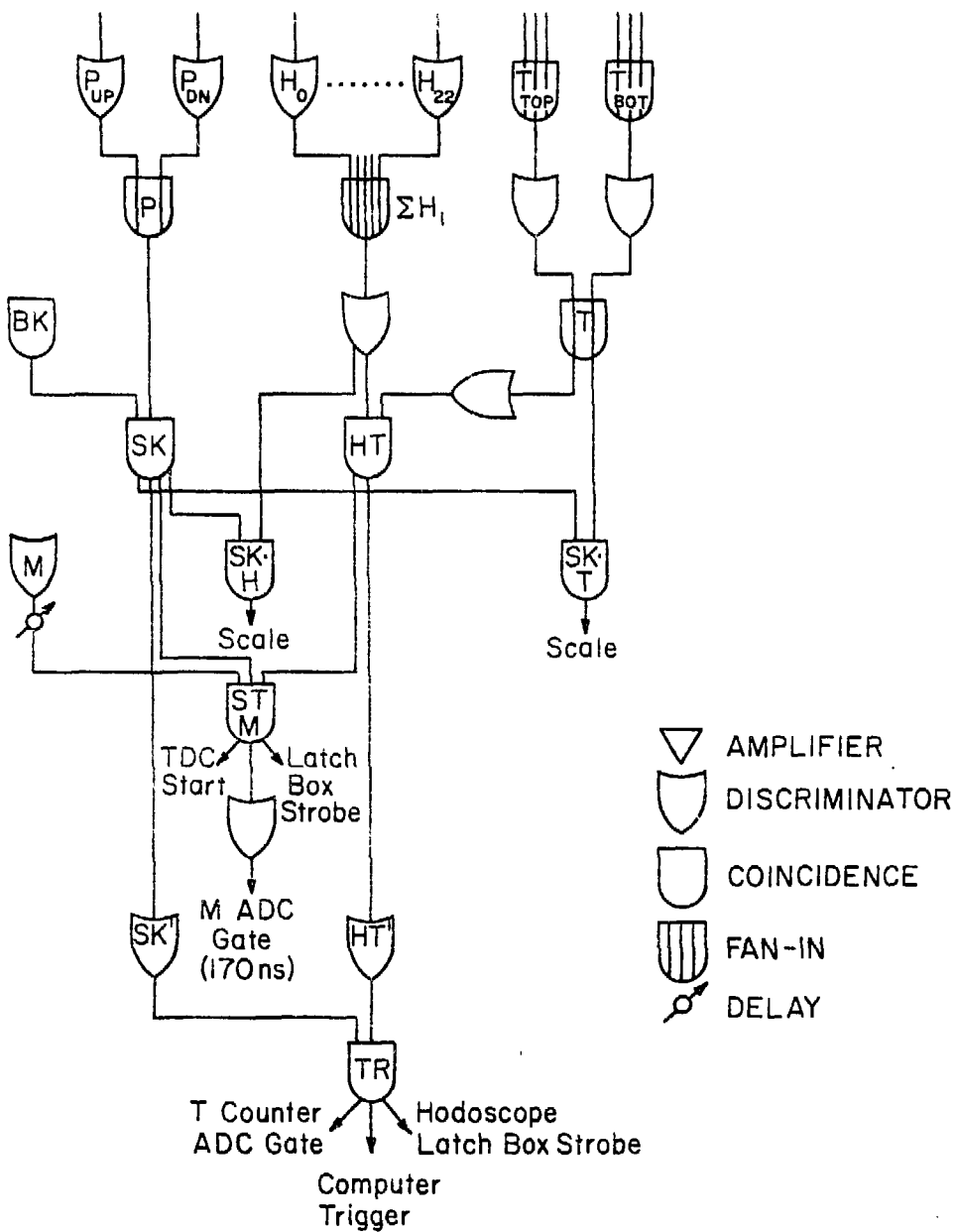
Figure 10

"K" tubes to produce the coincidence K. A legitimate kaon signal defined by  $\bar{C} = \bar{\pi} \cdot K$  was then put into coincidence with BD to produce BK.

As mentioned in Section II.2 a backward going  $K^-$  from a  $K^-p$  elastic collision or its decay products could veto the event by faking a " $\pi$ " signal in the  $\bar{C}$ erenkov counter. Most such backward going K's traversed M again and gave a pulse that overlapped sufficiently with that from the passage of the beam  $K^-$  to yield an exceptionally large (more than 3.5 times "minimum ionizing") signal in the counter. To reduce the number of such false vetoes 10% of the  $M_{DT}$  signal was amplified and fed into a discriminator whose threshold was set at 3.5 times the "minimum ionizing" pulse height. The output of this discriminator could then cancel the  $\bar{C}$ erenkov counter pion signal (see Fig. 10).

In addition to the beam definition system a pair of multiwire proportional chambers (MWPC) placed between S1 and  $\bar{C}$  provided information on the beam profile. Each chamber consisted of 96 vertical gold plated tungsten wires with 2 mm horizontal spacing. The two chambers were separated by about 80 cm. The wire chamber readout system, described in Ref. 37, stored the hit pattern in each chamber in a CAMAC module (Kinetics Systems KS3430) for each event trigger. The chambers, filled with an Ar-CO<sub>2</sub> gas mixture and operated between 2800 and 3000 V, had an efficiency of about 90% due to rate limitations in the readout system. Since the chambers were used only to monitor the beam profile this inefficiency was not a problem.

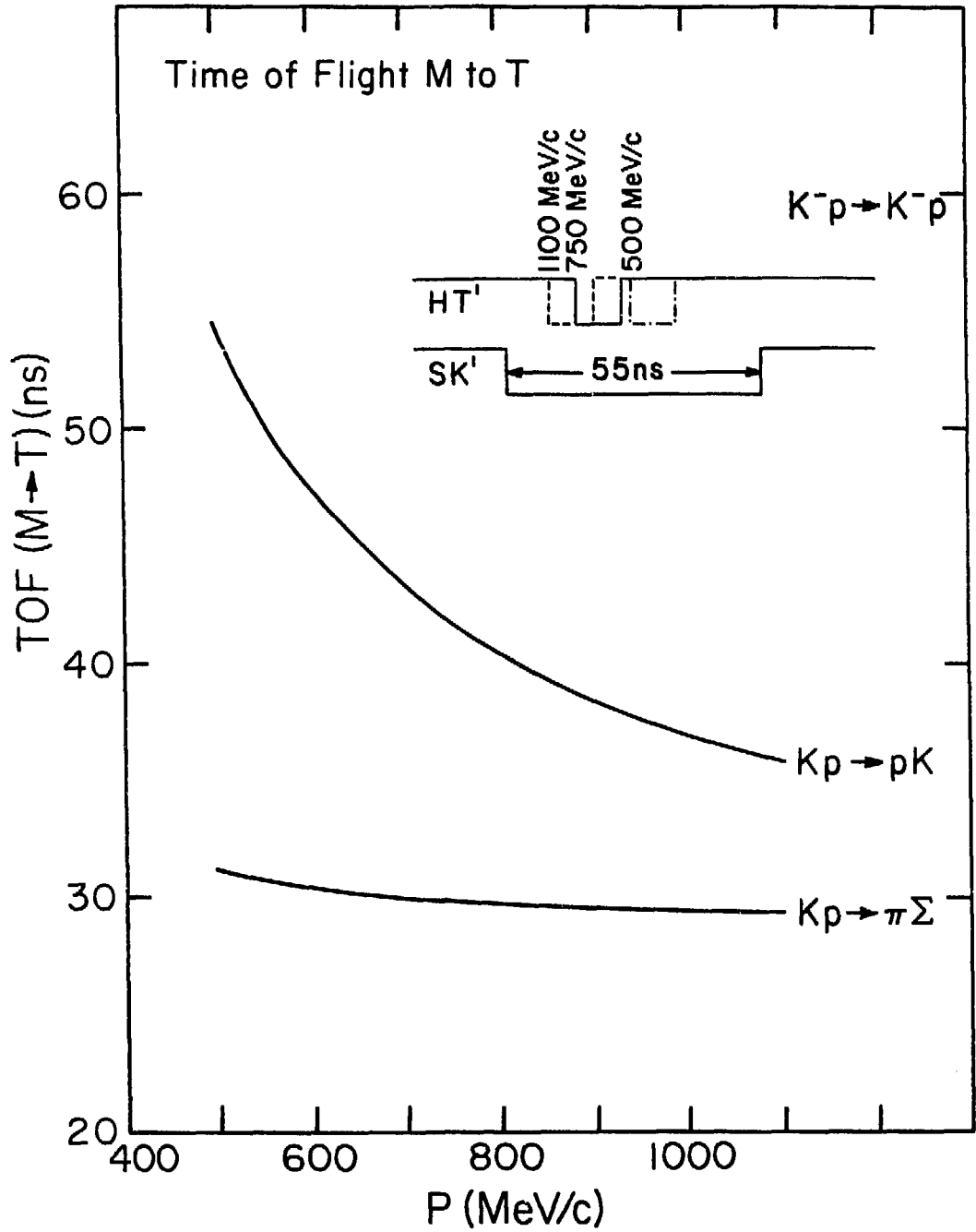
The trigger electronics are shown in Fig. 11. The logic signals from both halves of the P counter were summed to produce P which was then placed into coincidence with BK. The result, SK, indicated that an



## TRIGGER ELECTRONICS

XBL 799-11621

Figure 11



XBL 799-11622

Figure 12. Timing for  $TR = SK' \cdot HT'$

incoming kaon had produced a particle that passed through the P counter. Most of these were beam kaons that later hit the iron of Q7, Q8, and D5.

The final trigger required a count in both the hodoscope, H, and the time-of-flight array, T, to give  $HT = T \cdot H$ . This was then combined with the SK signal to produce the trigger coincidence  $TR = SK' \cdot HT'$ . Figure 12 shows the variation with beam momentum of the time difference between the arrival of a beam  $K^-$  at the M counter and the detection of a secondary proton at the hodoscope. Because of the variation, the width of  $SK'$  was made large enough (55 ns) so that as the momentum ranged from 500 to 1100 MeV/c and  $HT'$  occurred later or earlier with respect to the leading edge of  $SK'$ , the  $HT'$  pulse always fell within the  $SK'$  gate (see the timing diagram for  $TR = HT' \cdot SK'$  at three representative  $K^-$  momenta on Fig. 12). This allowed the timing to remain unchanged as the momentum was varied. However, particles other than protons with different TOF's through the spectrometer produced an  $HT'$  signal outside the  $SK'$  gate. The other electronics shown in Fig. 11 provided triggers and gates for the CAMAC interrupt register, latch boxes, TDC's, and ADC's.

The rates for each of the coincidences B, BD, BK, SK, and TR are listed at several momenta in Table III.

### II.7. Data Acquisition

At each momentum data were accumulated in a series of full and empty target runs. As mentioned in Section II.4, the spectrometer magnets were operated with higher currents for empty target runs to account for the energy loss in the  $LH_2$  by background protons from  $K^-p$  interactions upstream of the hydrogen target when it was full.

Figure 13 shows the kaon flux per  $10^{12}$  protons incident on the "C"

Table III

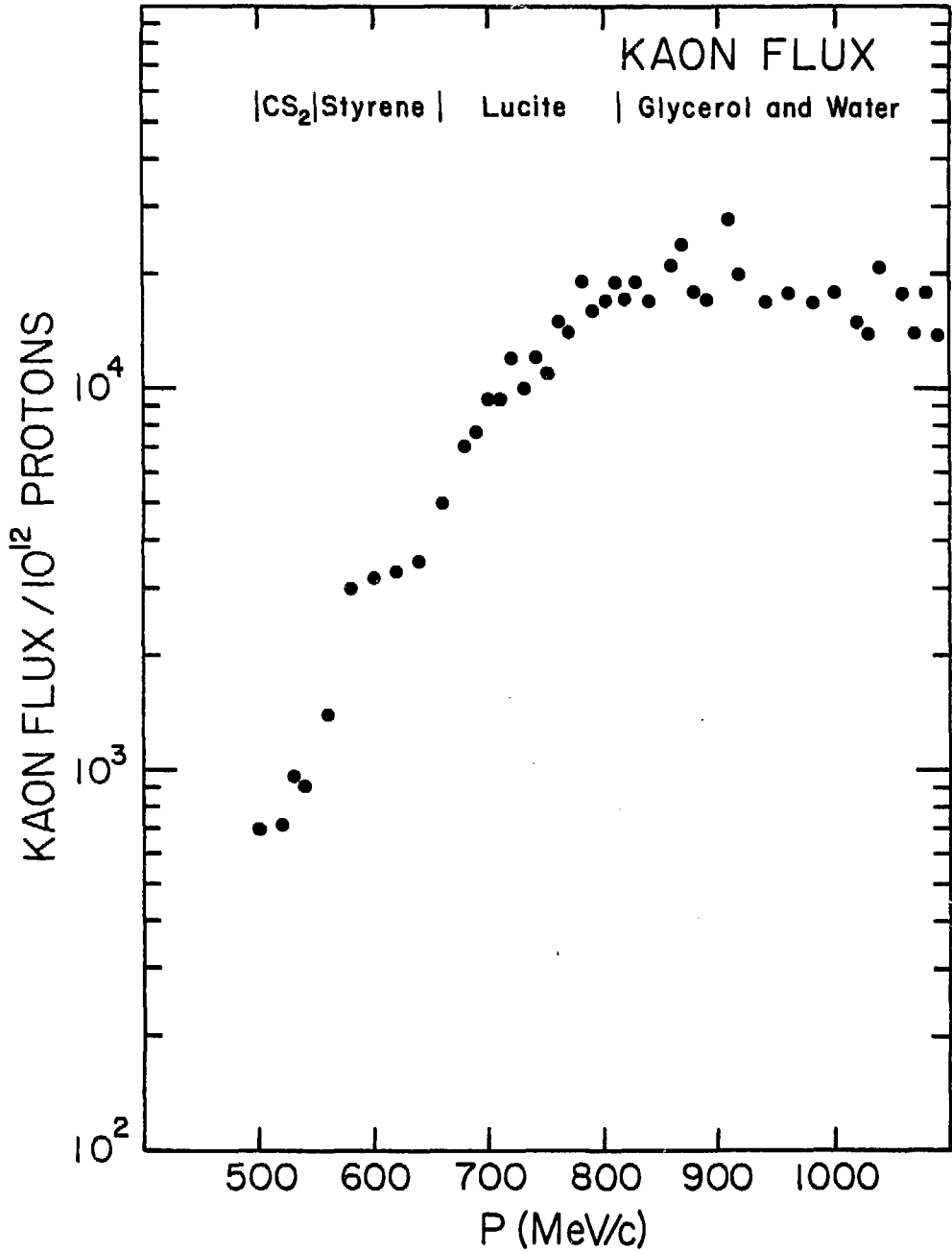
Coincidence Rates

(per  $10^{12}$  protons incident on the C target;  
typical beam was  $\sim 2 \times 10^{12}$  protons/pulse)

Coincidence	Rate		
	500 MeV/c	750 MeV/c	1050 MeV/c
B	46400	123000	246000
BD	44100	107000	181000
BK	265	12800	13100
SK	0.747	19.9	16.7
TR	0.018	0.71	1.27

Note: SK and TR are full target rates





XBL 799-11625

Figure 13.  $K^-$  flux per  $10^{12}$  protons on the "C" target as a function of the  $K^-$  beam momentum

production target as a function of the tuned value of the beam momentum. At most momenta enough event triggers were taken to yield a statistical error of only 2-3%. But, since the kaon flux drops by a factor of 30 between 800 and 500 MeV/c this was not always possible. The statistical errors are minimized if the ratio of total full target kaon flux,  $\phi_F$ , to empty target flux,  $\phi_{MT}$ , is given by

$$\frac{\phi_F}{\phi_{MT}} = \sqrt{\frac{R_F}{R_{MT}}} \quad (11)$$

where  $R_F(R_{MT})$  are the full (empty) target event rates, i.e., triggers per incident kaon. The total full and empty target flux accumulated at each momentum approximated this relation.

The data acquisition system consisted of CAMAC interfaced to a PDP 11/34 computer. All the counters in the H and T hodoscopes were fed into CAMAC latches, most of the coincidences and many of the single counters were scaled, time-of-flights were recorded in CAMAC TDC's and pulse heights for the M counter and each of the TOF counters were recorded by CAMAC ADC's. When an even trigger (TR) occurred, an interrupt was fed to the PDP 11/34 and the event information was read into the computer. Between AGS pulses, the computer performed several minor checks and conversions on the raw data (e.g., converting latch bit patterns into hodoscope channel numbers) and then wrote the data onto magnetic tape for further analysis by off-line software. In addition, the computer accumulated the data on-line and could display, on command, histograms of various quantities such as events per hodoscope channel or ADC or TDC distributions. The structure of the on-line program is outlined in Appendix 5. This facility was very useful in the setup and

Table IV  
Repeated Data Points

$P_{K^-}$ (MeV/c)	$\frac{d\sigma}{d\Omega}$ ( $\theta_{K^-} = 180^\circ$ ) (uncorrected) (mb/sr)	Special running conditions*
642	0.426 $\pm$ .023 0.414 $\pm$ .026	Lucite $\checkmark$ cell Styrene $\checkmark$ cell
663	0.381 $\pm$ .018 0.388 $\pm$ .023	
673	0.421 $\pm$ .016 0.412 $\pm$ .018	
683	0.381 $\pm$ .016 0.380 $\pm$ .026	
694	0.342 $\pm$ .016 0.398 $\pm$ .022	
704	0.413 $\pm$ .015 0.397 $\pm$ .016	$\Delta p/p = \pm 1.5\%$ $\Delta p/p = \pm 1.0\%$
714	0.415 $\pm$ .014 0.431 $\pm$ .021	
724	0.414 $\pm$ .015 0.437 $\pm$ .015 0.394 $\pm$ .020	$\Delta p/p = \pm 1.0\%$ $\Delta p/p = \pm 1.5\%$ $\Delta p/p = \pm 1.0\%$
734	0.504 $\pm$ .020 0.495 $\pm$ .016	
745	0.542 $\pm$ .018 0.517 $\pm$ .023	
805	1.041 $\pm$ .020 1.056 $\pm$ .021	
826	1.126 $\pm$ .026 1.078 $\pm$ .028	Lucite $\checkmark$ cell Glycerol + H <sub>2</sub> O $\checkmark$ cell

\* Some runs were repeated with different  $\checkmark$  Cerenkov counter cells or with the momentum jaws (see Fig. 5) set for a different  $\Delta p/p$ . Those runs are explicitly identified in this column.

Table IV (cont.)

$P_{K^-}$ (MeV/c)	$\frac{d\sigma}{d\Omega}(\theta_{K^-} = 180^\circ)$ (uncorrected) (mb/sr)	Special running conditions*
926	$1.565 \pm .038$	$\Delta p/p = 1.0\%$
	$1.627 \pm .026$	$\Delta p/p = 0.5\%$
947	$1.786 \pm .039$	
	$1.771 \pm .023$	
1007	$2.124 \pm .034$	
	$2.076 \pm .045$	
	$1.992 \pm .031$	
1051	$1.684 \pm .028$	
	$1.659 \pm .039$	

\* Some runs were repeated with different  $\gamma$  Čerenkov counter cells or with the momentum jaws (see Fig. 5) set for a different  $\Delta p/p$ . Those runs are explicitly identified in this column.

debugging of the experiment and also for on-line monitoring of the experimental operation.

As a consistency check, several momenta were repeated during the experiment. The data from these runs are compared in Table IV and, within the statistical accuracy of the data points, show no time-dependent systematic effects.

### III. DATA ANALYSIS

#### III.1 General Approach

Ideally, for determination of the  $K^-p$  backward elastic differential cross-section, one would like to measure only backward elastic events that originate in the liquid hydrogen target. Then the differential cross-section would be given by:

$$\frac{d\sigma}{d\Omega} = \frac{1}{\Delta\Omega} \frac{N}{n_p N_K} \quad (12)$$

$N$  = number of  $K^-p$  backward elastic events

$\Delta\Omega$  = solid angle acceptance in the center of mass

$n_p$  = number of protons per unit area in the  $LH_2$  target

$N_K$  = number of incident  $K^-$ 's.

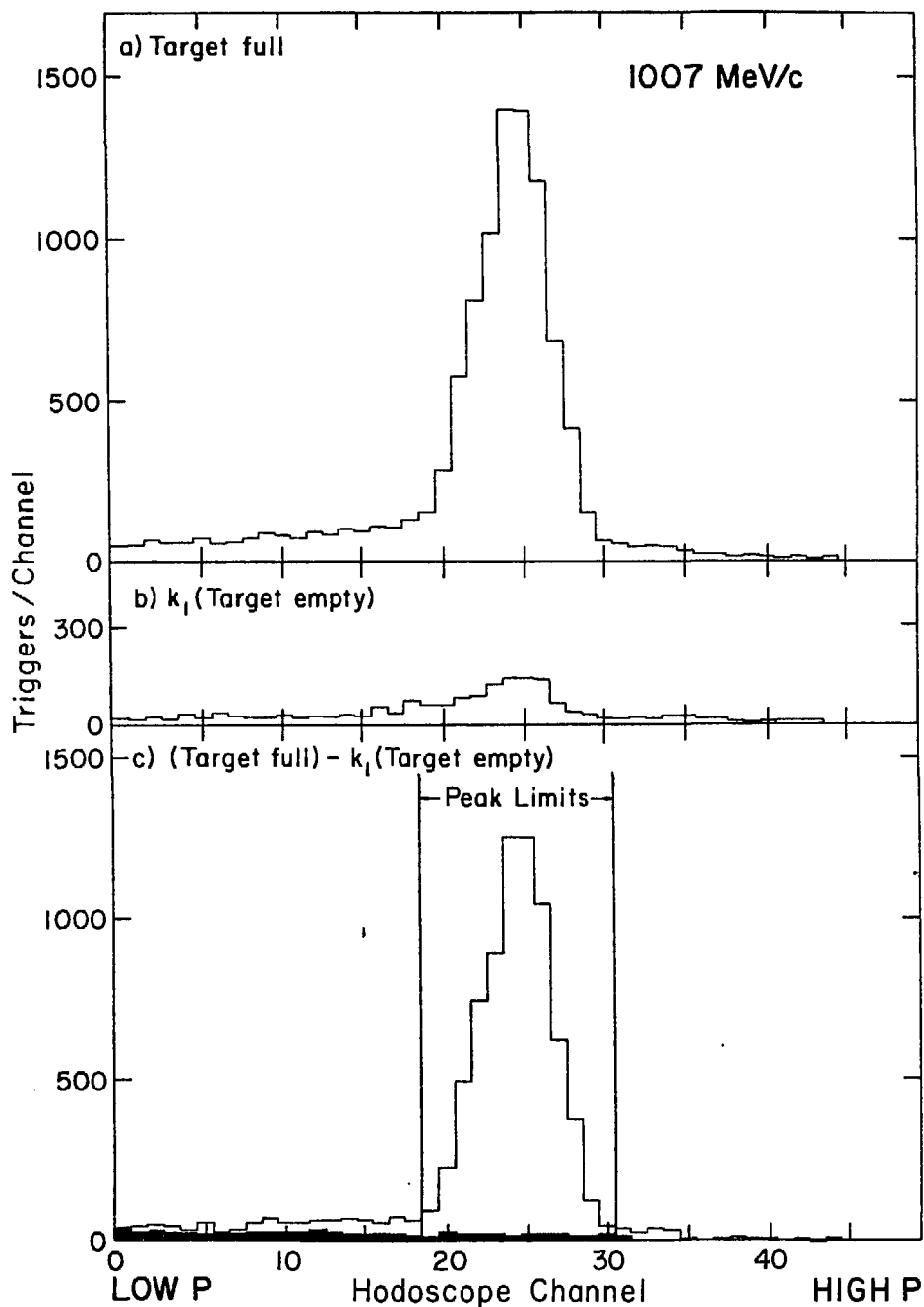
In practice, of course, the raw data must be subjected to considerable analysis in order to extract the above numbers. In addition to the usual subtraction of empty target events a number of other corrections must be made to the data, including subtraction of background events and corrections for loss of beam kaons and loss of forward scattered protons. The resulting expression for the backward differential cross-section is:

$$\frac{d\sigma}{d\Omega} = \frac{A}{\rho L N_0} \cdot \frac{1}{(BK)} \cdot \frac{d\Omega_{lab}}{d\Omega} \cdot \frac{1}{\Delta\Omega_{lab}} \cdot (\prod C_i) \cdot (F - \frac{k_1 M}{C_7} - B) \quad (13)$$

where,

- $A$  = 1.008, the atomic weight of hydrogen,  
 $\rho$  = 0.070 g/cc, the density of liquid para-hydrogen in the target after subtraction of the gas-filled empty effect (see Section II.3),  
 $L$  = 20.96 cm, the target length measured along its cylindrical axis,  
 $N_0$  = Avogadro's number,  
 $(BK)$  = the number of beam particles, electronically identified as kaons, that produced  $F$  counts when the target was full,  
 $\frac{d\Omega}{ds}_{lab}$  = the laboratory to center of mass solid angle transformation,  
 $\Delta\Omega_{lab}$  = 9.78 msr, the solid angle subtended by the P counter in the laboratory,  
 $M$  = the observed number of counts with the target empty for  $\frac{BK}{k_1}$  incident kaons,  
 $B$  = a background (see Section III.2),  
 $\prod_i C_i$  and  $C'_7$  = various correction factors of order 1 explained in Section III.3 and Appendix 4.

The large amount of hydrogenous material in the beam line, 28 cm of  $LH_2$  equivalent, contributed about 10-20% of the observed full target events. Thus, the first step in the data analysis was the channel by channel subtraction of empty target events from full target events on the hodoscope. Since only 1/3 to 1/2 as many kaons were incident on empty target runs as on full target runs, the measured number of empty target events were renormalized by a factor  $k_1 \approx 2-3$  before the subtraction. The target full, renormalized target empty, and subtracted hodoscope distributions at one momentum (1007 MeV/c) are shown in Fig. 14.



XBL 795-9818

Figure 14. Hodoscope distributions for  $K^- p + K^- p$  ( $\theta_{K^-} = 180^\circ$ ) for  $P_{K^-} = 1007$  MeV/c

- a) Target full
- b) Renormalized target empty
- c) Empty target effect subtracted; the shaded area is the background predicted by Monte Carlo calculations



The experiment was designed so that protons from backward elastic scatters fell on the central one-third of the hodoscope. For the purpose of background determination, high and low momentum cuts were made on the elastic peak with care taken to ensure that the tails of the elastic peak were not excluded (see Fig. 14). The Monte Carlo model of the experiment (described in detail in Appendices 3 and 4), which allowed for multiple scattering of protons downstream of the interaction point in the target, showed that these limits placed on the hodoscope distribution included all protons from  $K^-p$  backward scatters. The Monte Carlo program was also used in the calculation of the background,  $B$ , and some of the correction factors,  $C_i$ .

### III.2 Background Subtraction

Background protons accounted for 7-26% of the events in the data peak, with the larger contribution occurring only between 600 and 700 MeV/c where the backward elastic cross-section is small. Since particles other than protons were rejected by time-of-flight considerations, only inelastic reactions that could yield protons should have contributed to the background. Table V lists those reactions with the most significant cross-sections that yielded final state hyperons that eventually decayed to protons and other particles. From Fig. 15 it is apparent that protons from each of these reactions could have momenta that fell within the  $\pm 13\%$   $\Delta p/p$  acceptance of the hodoscope. Also shown in Fig. 15 is the maximum momentum of protons from  $K^-p \rightarrow K^-p\pi^0$ . However, these protons would have momenta too low to reach the hodoscope except above 900 MeV/c incident  $K^-$  momentum where they hit the low momentum side of the

Table V

Background Reactions

$K^-p$ Final State	Cross Section (mb)	Decay Sequence	Total branching ratio for decay to protons
$\Lambda\pi^0$	2 - 4	$\Lambda \rightarrow p\pi^-$	.642
$\Sigma^0\pi^0$	1 - 3	$\Sigma^0 \rightarrow \Lambda\gamma^-$ $\Lambda \rightarrow p\pi^-$	.642
$\Sigma^+\pi^-$	1.5 - 6	$\Sigma^+ \rightarrow p\pi^0$	.516
$\Lambda\pi\pi$	2 - 7	$\Lambda \rightarrow p\pi^-$	.642
$\Sigma^+\pi^-\pi^0$	0.1 - 1.1	$\Sigma^+ \rightarrow p\pi^0$	.516

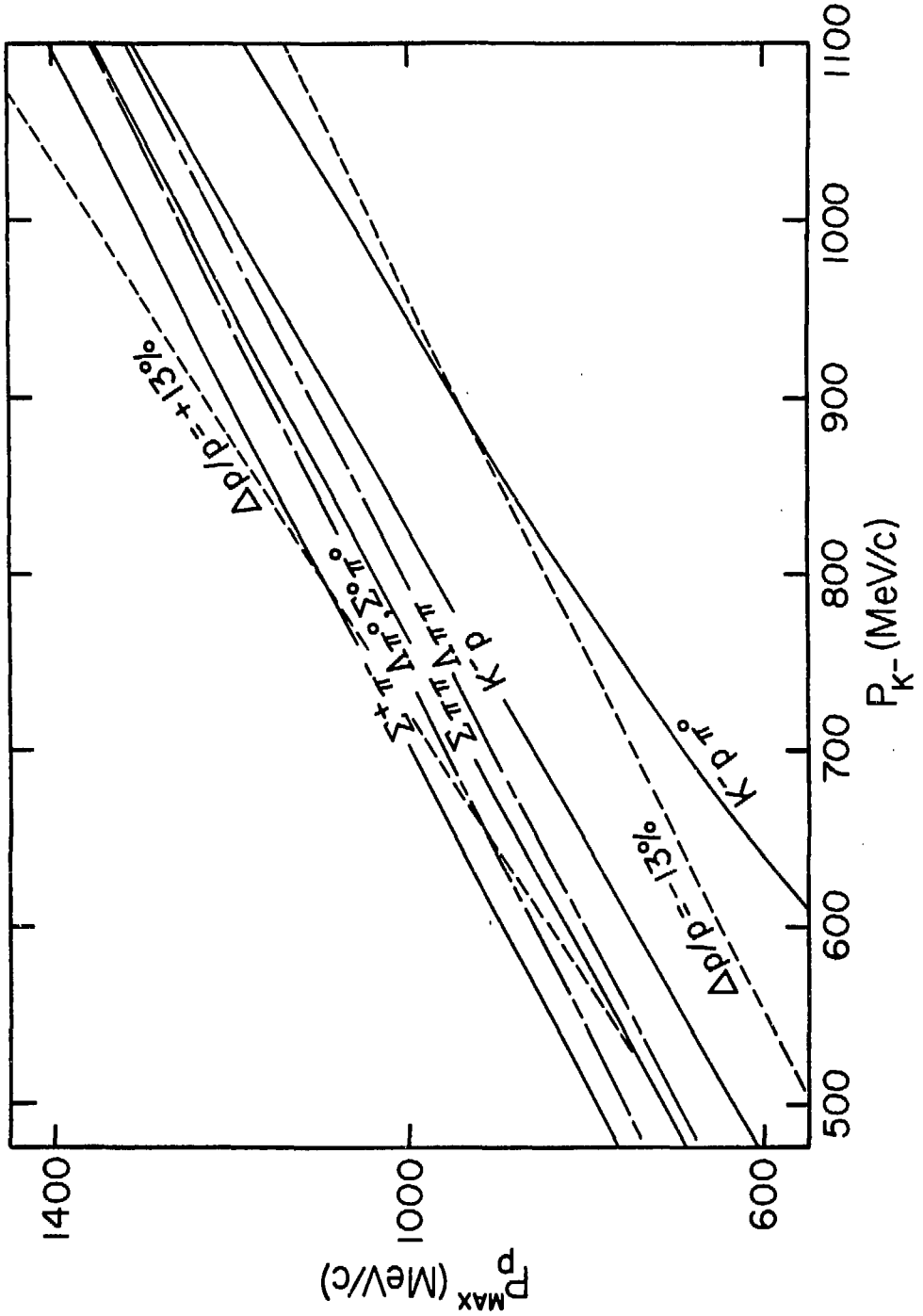


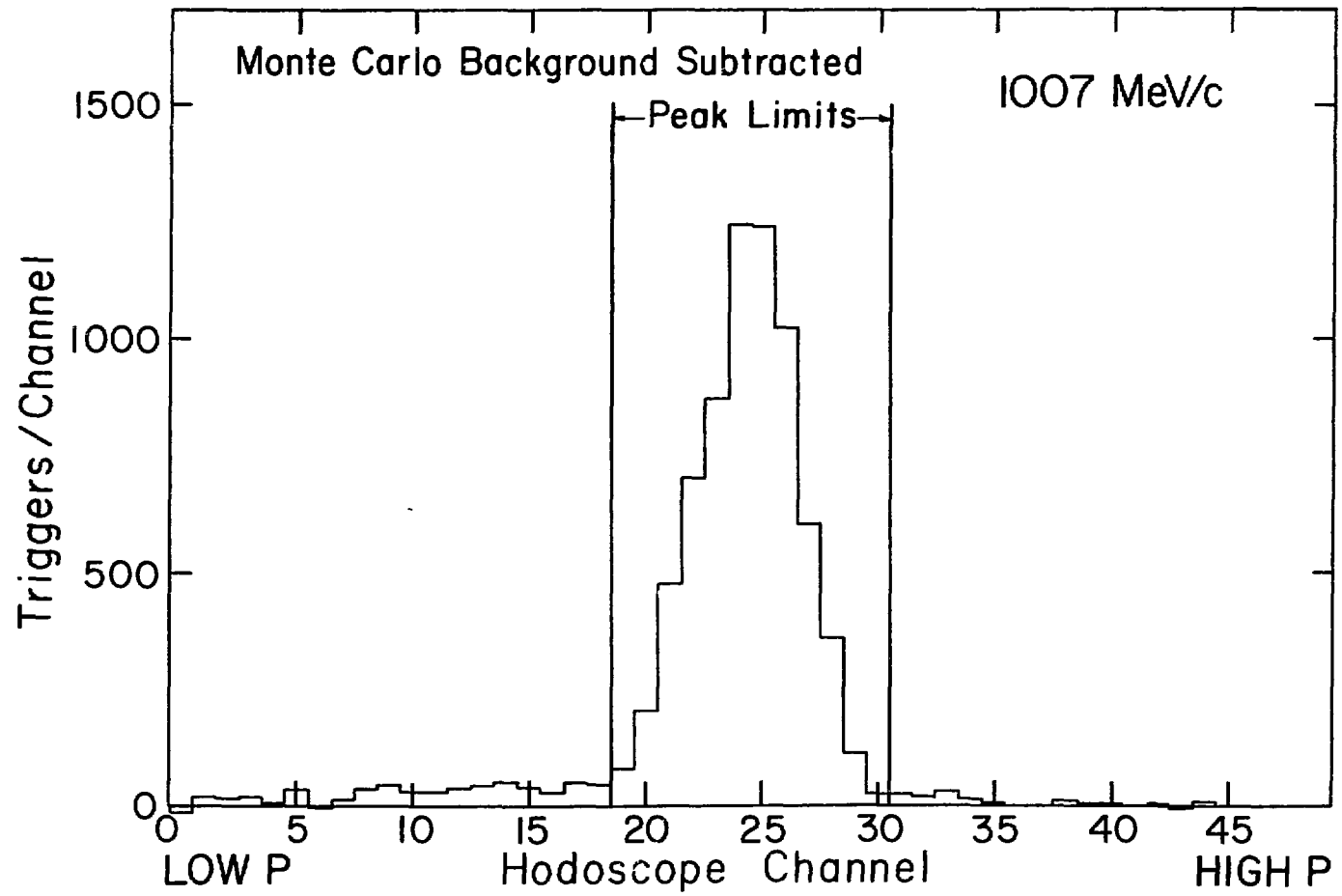
Figure 15. Maximum momentum of protons from background reactions as a function of incident  $K^-$  momentum

hodoscope well outside the elastic region.

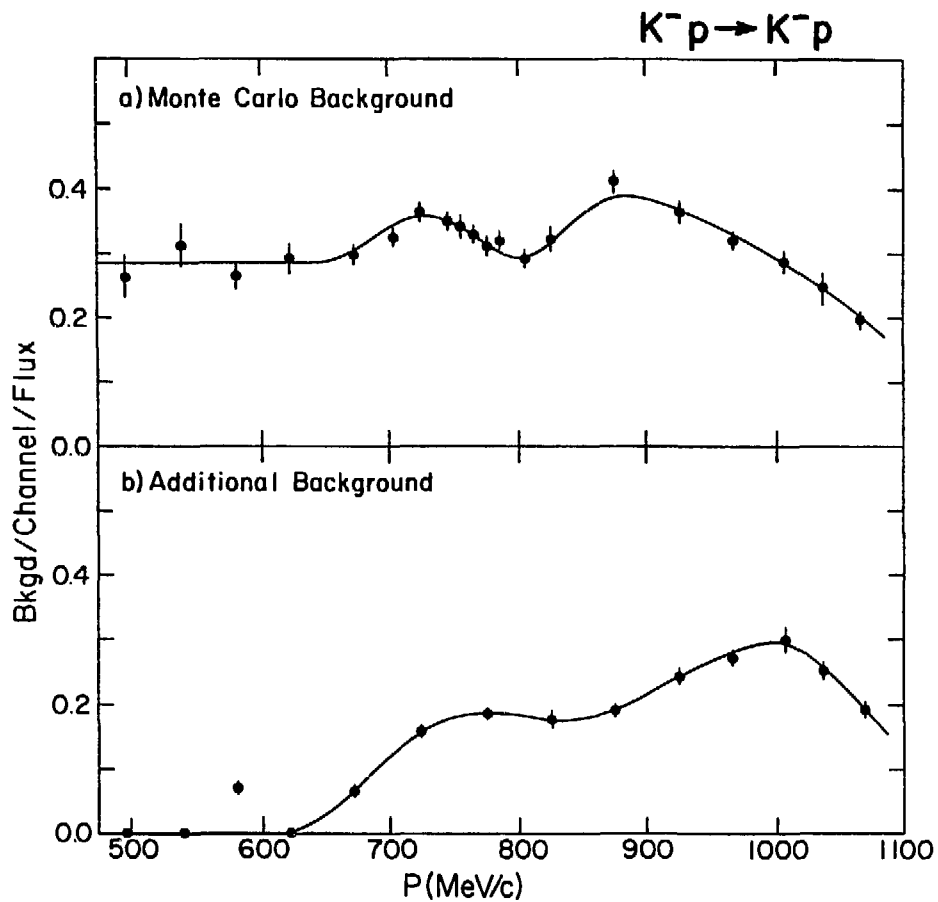
It was originally hoped that the Monte Carlo model of the above reactions would explain all the observed background. After normalization to the experimental kaon flux, the Monte Carlo values for background events were compared with the observed number of protons bin by bin in the hodoscope distributions. The area of the hodoscope outside the limits on the elastic peak provided a check on the ability of the Monte Carlo to model all the background. The Monte Carlo could then fix the structure of the background under the elastic peak. While this method worked quite well at low momenta, there was an additional unexplained background above 625 MeV/c. Fig. 14c, at 1007 MeV/c incident  $K^-$  momentum where this problem was most pronounced, shows that the Monte Carlo prediction for the background is too low. Thus a two step process was necessary for the proper subtraction of background events. First, the Monte Carlo events calculated as explained above were subtracted to give a hodoscope distribution like that in Fig. 16. The unexplained background is evidenced by the tails that remain outside the elastic peak. This additional background was subtracted by averaging its magnitude over several channels on the low momentum side of the elastic peak and similarly on the high momentum side. The background contribution to the elastic peak was then assumed to be the average of these two values.

Calculations of both the Monte Carlo and the additional background were performed as explained immediately above at several momenta. The results with their statistical errors were then plotted as background events per hodoscope channel per  $10^6$  incident kaons as shown in Fig. 17. For use in the reduction of the data at each beam momentum smooth curves

Figure 16. Hodoscope distributions for  $K^+ p + K^- p$  ( $\theta_{K^-} = 180^\circ$ ) for  $P_K^- = 1007 \text{ MeV}/c$



XBL 799-11639



XBL 793-8955

Figure 17. Background per hodoscope bin per  $10^6 K^-1 s$  as a function of the incident beam momentum

- a) Monte Carlo background
- b) Unexplained additional background

were drawn through these points. The complicated momentum structure of the Monte Carlo background is due to individual large variations in the cross-sections of each of the five reactions considered over this momentum range. The contribution of each inelastic channel to the background is discussed more fully in Appendix 3. The momentum structure of the unexplained background is reminiscent of that of the  $K^-p$  backward elastic cross-section (see Fig. 2). This suggests that the unexplained background is made up of protons that are scattered at too wide an angle to hit the P counter directly but instead are deflected through P by the pole faces of D4 and then reach the hodoscope. Although this effect is not easily calculated, any contribution to the overall systematic error should be small since unexplained background events never comprised more than 6% of the elastic peak.

### III.3 Corrections

The correction factors,  $\prod_i C_i$ , include two different kinds: (1) corrections to the beam flux and to the path length in the target and (2) corrections for the loss of scattered secondary protons. As can be seen from Table VI, no correction factor was ever larger than a few per cent giving a total overall correction factor averaging 15% (9% coming from corrections of type (1) and 6% from corrections of type (2)). The momentum dependence of each correction factor is plotted in Fig. 18. A complete discussion of the evaluation of each of these correction factors may be found in Appendix 4. All Monte Carlo calculations were carefully cross checked by hand.

### III.4 Summary

Figure 19 shows the raw data and the overall correction factor

Table VIa

K <sup>-</sup> beam intensity and path length corrections			
		$\underline{C_i}$	$\underline{\delta C_i}$
C <sub>1</sub>	Beam contamination ( $\pi, \mu, e$ )	1.0001 - 1.021	$\pm 0.001$
C <sub>2</sub>	Decays of beam K <sup>-</sup> between Čerenkov and S <sub>2</sub> counter	1.0098	$\pm 0.0002$
C <sub>3</sub>	Interactions of beam K <sup>-</sup> in counter S <sub>2</sub>	1.0041	$\pm 0.0005$
C <sub>4</sub>	Decays of beam K <sup>-</sup> between counter S <sub>2</sub> and downstream end of target	1.0204 - 1.0469	$\pm 0.0001$
C <sub>5</sub>	Interactions of beam K <sup>-</sup> in target	1.0148 - 1.0225	$\pm 0.0001$
C <sub>6</sub>	Target length (end profile averaged over beam distribution)	1.0230	$\pm 0.0005$



Table VIb

## Losses of secondaries

	$K^-p \rightarrow K^-p$		$K^-p \rightarrow \Sigma^- \pi^+$	
	$C_i$	$\delta C_i$	$C_i$	$\delta C_i$
$C_7$ Absorption in hydrogen, acceptance of spectrometer (apertures)	1.041 - 1.060	$\pm 0.002$	1.033 - 1.067	$\pm 0.002$
$C_7'$ Absorption of secondaries in hydrogen (difference for target full vs. empty)	1.020 - 1.037	$\pm 0.0004$	1.013 - 1.052	$\pm 0.0015$
$C_8$ $\pi^+$ decay ( $\Sigma^- \pi^+$ only)	1.000		1.120 - 1.299	$\pm 0.002$
$C_9$ Backward $K^-$ vetoes ( $K^-p$ only) Backward $\Sigma^-$ vetoes ( $\Sigma^- \pi^+$ only)	1.0002 - 1.0011	$\pm 0.0004$	1.000	
$C_{10}$ Absorption in P counter and air column in spectrometer	1.014	$\pm 0.002$	1.016	$\pm 0.002$

NOTE: Correction factors for loss of  $\pi^+$ 's ( $K^-p \rightarrow \Sigma^- \pi^+$ ) are discussed in Appendix 6.

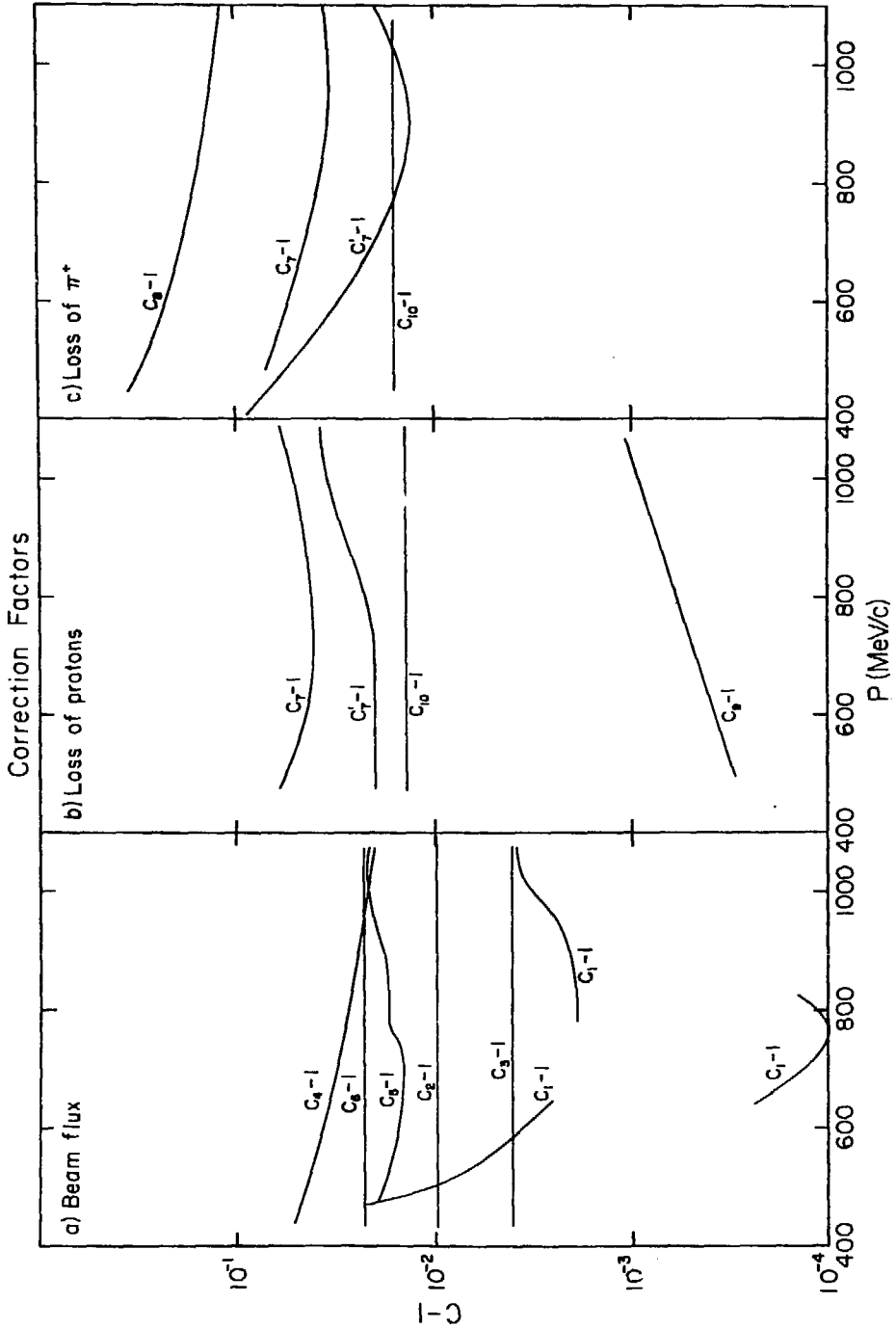


Figure 18. Momentum dependence of correction factors

NOTE: Correction factors for loss of  $\pi^+$ 's ( $K^-p \rightarrow \Sigma^- \pi^+$ ) are discussed in Appendix 6.

used in the final calculation of the  $K^-p$  backward elastic differential cross-section. The statistical accuracy of the data is typically 2.5% while the errors on each correction factor are always less than 0.2%. It is important to note that the contributions of the background (Fig. 17) and the overall correction factor (Fig. 19) are small and vary smoothly with the incident kaon momentum. As mentioned before, the dominant systematic error comes from uncertainties in the background determination and is estimated to lead to less than a 1% error in the overall normalization of the final results. This comes from assuming that the additional background under the data peak, rather than being the average of the low and high momentum backgrounds as above, is equal to either the low or high momentum background only.

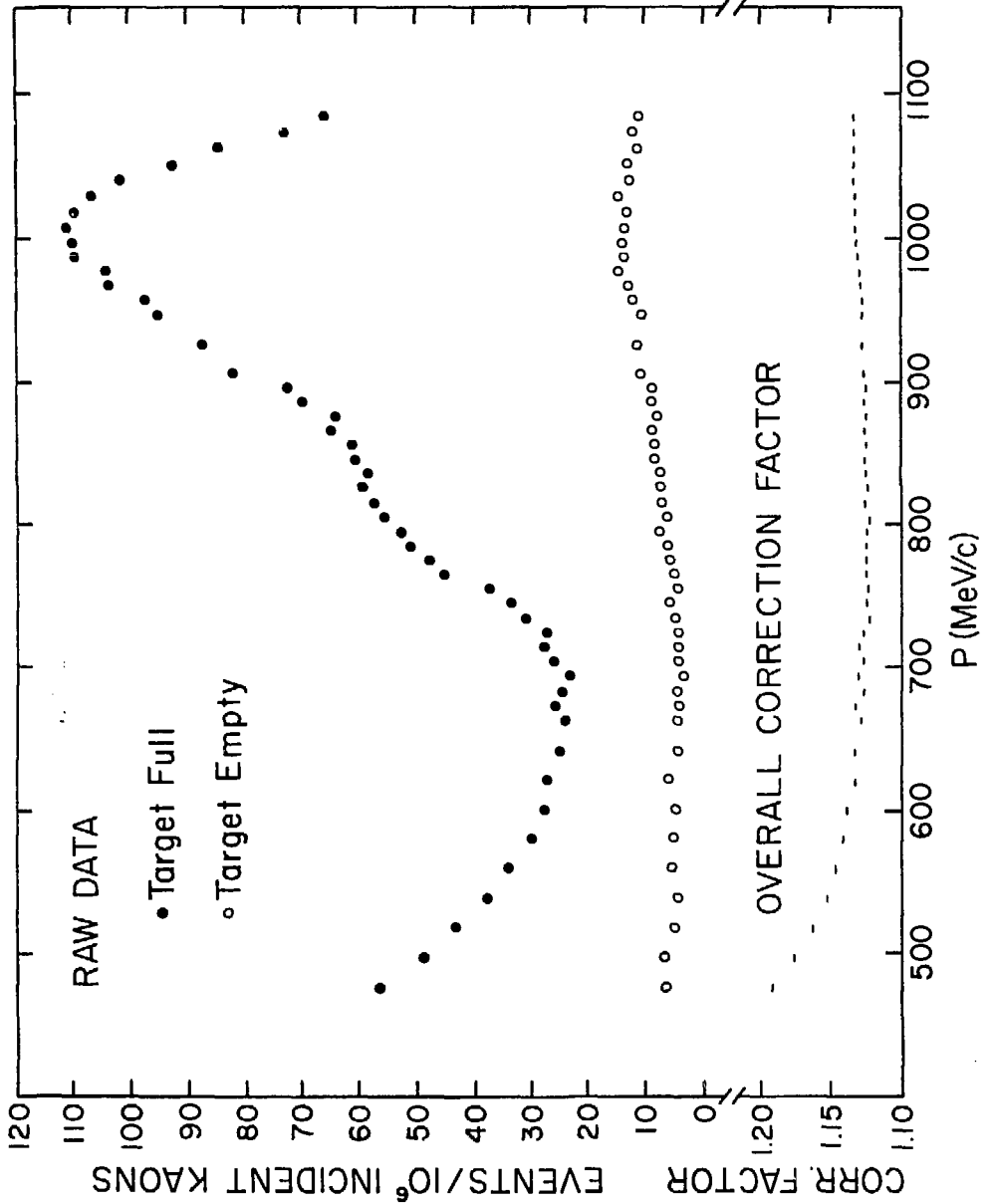


Figure 19. Raw data and overall correction factor used in calculating  $\frac{d\sigma}{d\Omega}(\theta_{K^-} = 180^\circ)$  for  $K^- p \rightarrow K^- p$

## IV. RESULTS AND CONCLUSIONS

### IV.1 The New Data

The fully corrected results of the measurement of the  $K^-p$  backward elastic cross-section are listed in Table VII and presented in Fig. 20. Figures 21 and 22 compare these data with the results of previous experiments and partial wave analyses. The errors shown in the figures are purely statistical and are typically 2.5% which is a factor of 10 improvement over the previous data.

The new  $K^-p$  backward elastic results agree only fairly well with the previous data but show good agreement with the RLIC and LBL partial wave analyses,<sup>(21,23)</sup> except above 850 MeV/c. In particular, in the region between 550 and 650 MeV/c both analyses have suggested that the differential cross-section should be larger than that measured by the earlier experiments. The new measurement confirms this behavior. The new data show clearly the rapid rise in the backward cross-section at the  $\Lambda\eta$  threshold (725 MeV/c) as expected from the cusp-like behavior of the S-wave amplitude in this region (see Section I.1). Similar behavior at the  $\Sigma\eta$  threshold (889 MeV/c) is not so apparent because the cross-section is already rising steeply due to the presence of a number of resonances (indicated on Fig. 20).

Above 950 MeV/c the new data differ significantly from the old. In attempting to fit the older data the previous PWA's all give a lower cross-section in this region. There is no apparent explanation for this discrepancy between the new and old data, but the new LBL analysis discussed below requires only an increase in higher angular momentum partial wave amplitudes and not the introduction of new resonances to fit the

Table VII

Differential cross section at  $180^\circ$  for the elastic scattering  
 $K^-p \rightarrow K^-p$  as a function of incident  $K^-$  beam momentum ( $P_{K^-}$ )

$P_{K^-}$ (MeV/c)	$\frac{d\sigma}{d\Omega}(180^\circ)$ (mb/sr)	$P_{K^-}$ (MeV/c)	$\frac{d\sigma}{d\Omega}(180^\circ)$ (mb/sr)
476	$1.487 \pm .085$	826	$1.240 \pm .021$
497	$1.211 \pm .067$	836	$1.220 \pm .022$
518	$1.068 \pm .057$	846	$1.197 \pm .025$
539	$0.895 \pm .051$	856	$1.229 \pm .023$
560	$0.745 \pm .031$	866	$1.289 \pm .023$
581	$0.626 \pm .030$	876	$1.319 \pm .022$
601	$0.566 \pm .029$	886	$1.424 \pm .024$
622	$0.513 \pm .030$	896	$1.507 \pm .026$
642	$0.477 \pm .019$	906	$1.677 \pm .020$
663	$0.433 \pm .016$	926	$1.811 \pm .024$
673	$0.472 \pm .013$	947	$2.000 \pm .022$
683	$0.429 \pm .015$	957	$2.044 \pm .045$
694	$0.408 \pm .015$	967	$2.178 \pm .024$
704	$0.457 \pm .012$	977	$2.140 \pm .036$
714	$0.474 \pm .013$	987	$2.300 \pm .034$
724	$0.472 \pm .011$	997	$2.295 \pm .037$
734	$0.560 \pm .014$	1007	$2.329 \pm .023$
745	$0.599 \pm .015$	1018	$2.305 \pm .034$
755	$0.746 \pm .019$	1029	$2.200 \pm .035$
765	$0.932 \pm .020$	1040	$2.117 \pm .032$
775	$0.982 \pm .021$	1051	$1.898 \pm .025$
785	$1.063 \pm .024$	1062	$1.738 \pm .028$
795	$1.090 \pm .021$	1073	$1.435 \pm .026$
805	$1.176 \pm .017$	1084	$1.279 \pm .034$
815	$1.221 \pm .023$		

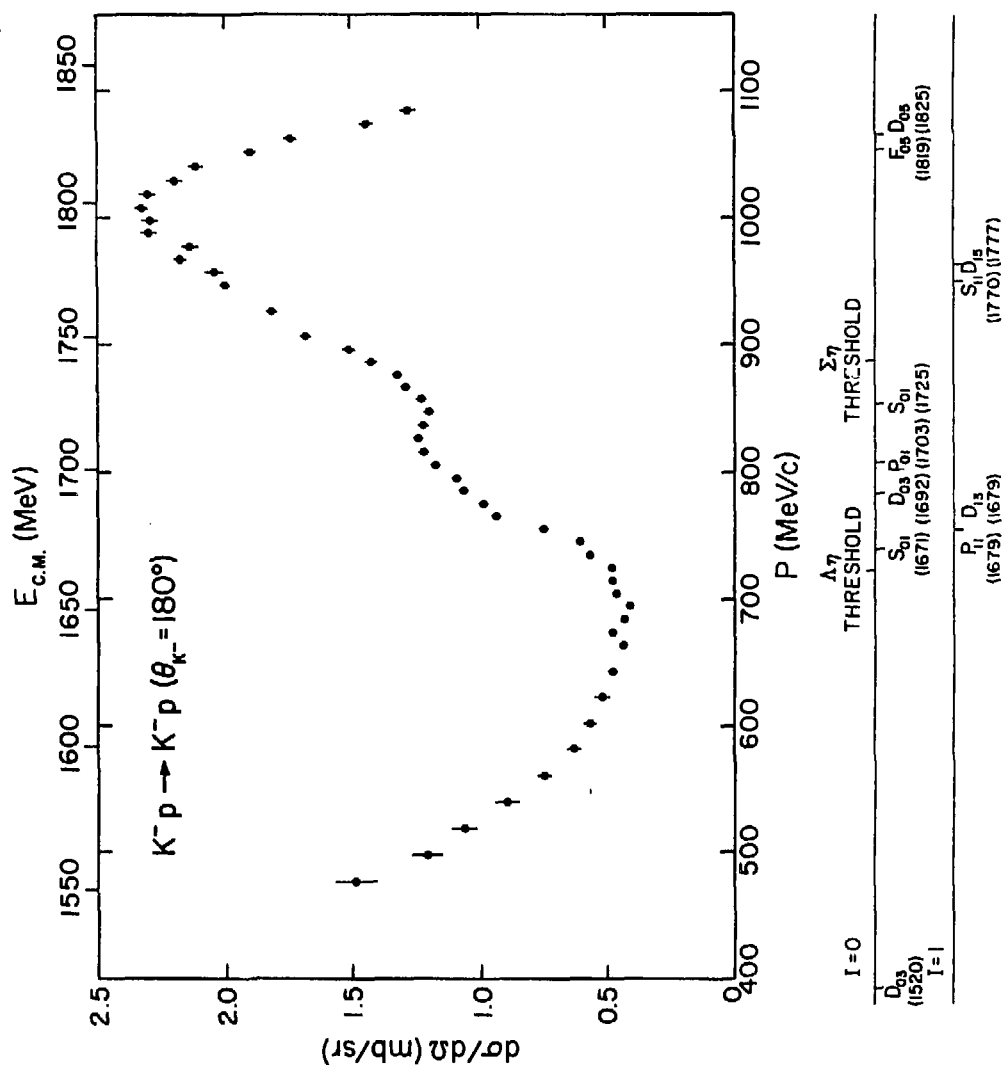
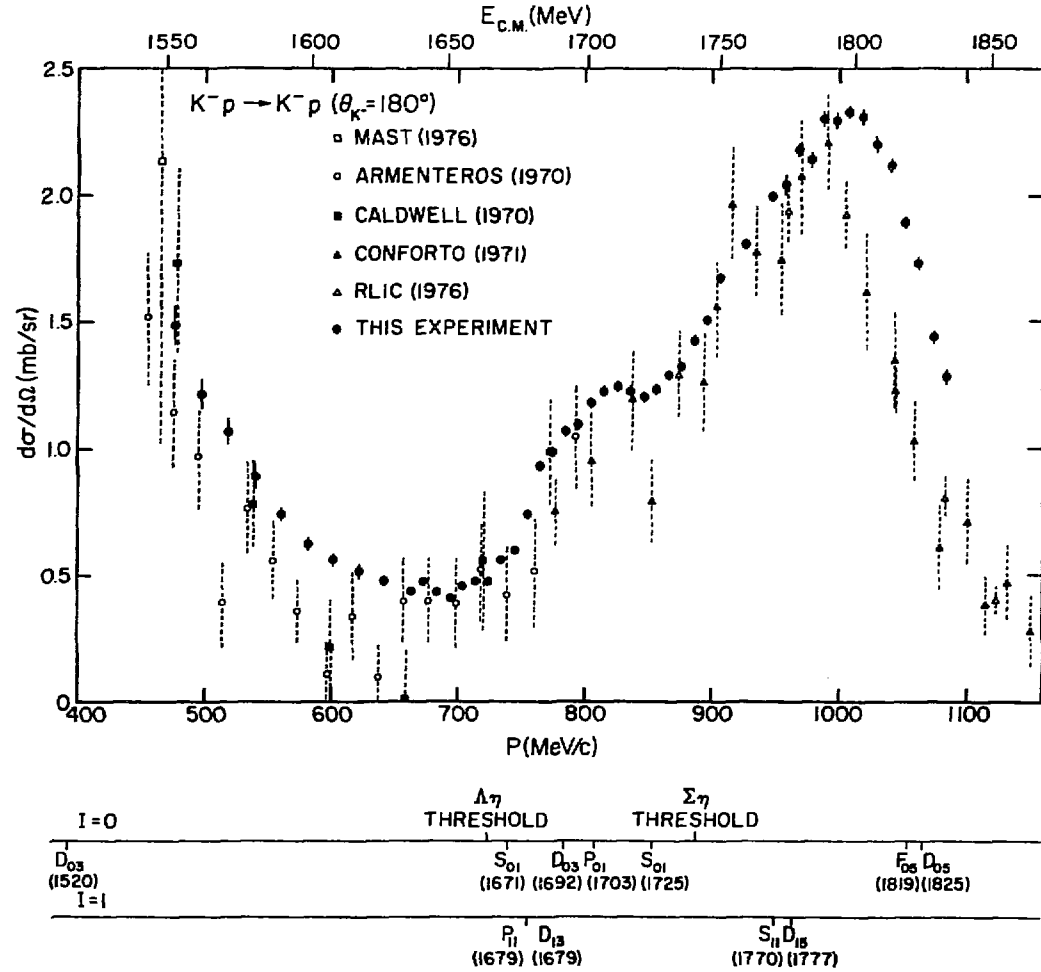


Figure 20. Results of this experiment for the  $K^- p$  backward elastic differential cross-section

Figure 21. Comparison of data from this experiment with data from previous experiments (Refs. 11-13, 16, 18)



XBL 799-11629



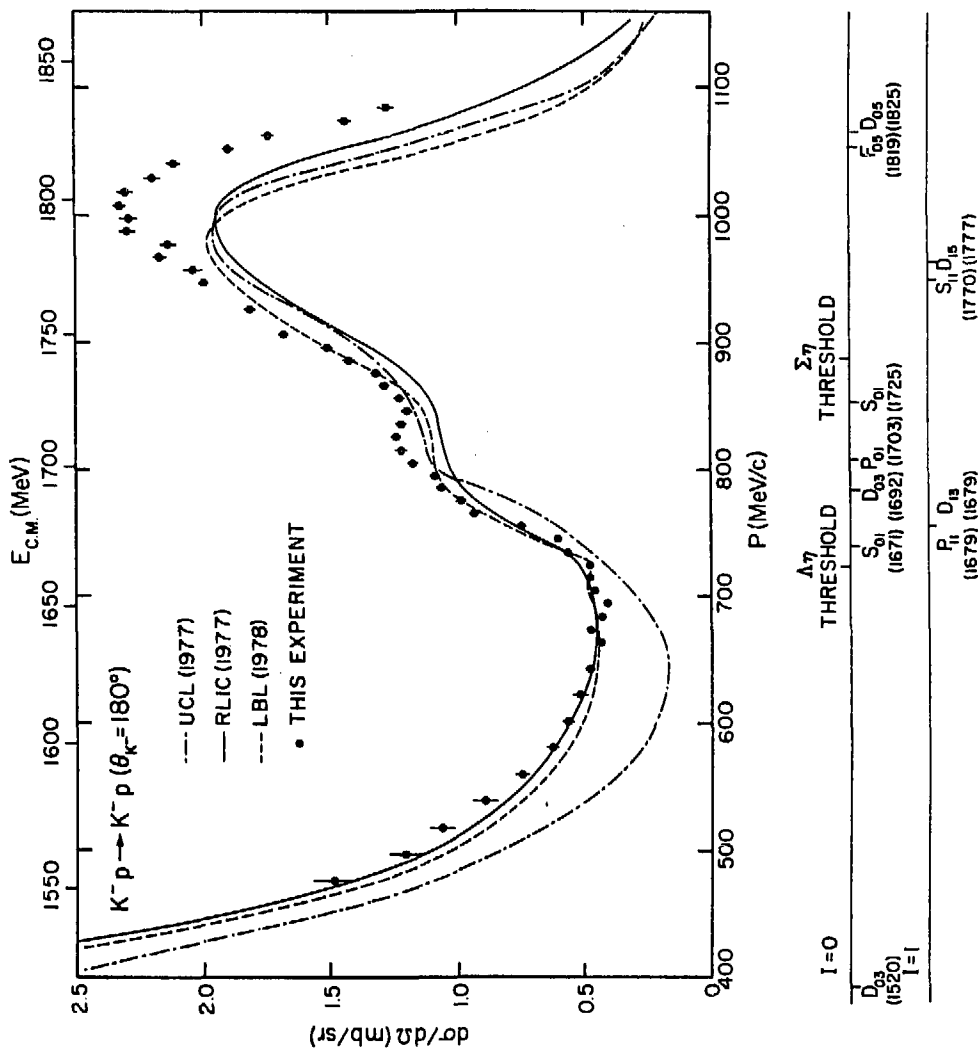


Figure 22. Comparison of data from this experiment with previous PWA's (Refs. 9, 21-23)

new results. The most significant feature of the new data is the enhancement between 800 and 850 MeV/c. Earlier PWA's do not exhibit this behavior while the previous data in that region are too sparse to give any indication of such structure. This is the same region where new structure was found in the high statistics charge exchange experiment<sup>(19)</sup> and the  $I=1$  cross-sections of Carroll et al.<sup>(38)</sup>

#### IV.2 Discussion of Partial Wave Analysis

To examine this enhancement in detail the LBL (1978) analysis<sup>(23)</sup> was extended to include the results of this experiment. Little change in the resonance parameters of the earlier analysis was required by the larger cross-sections above 950 MeV/c. Instead the background amplitudes were enlarged in the higher angular momentum partial waves whose contribution is small at low momentum and important only at the higher momenta. Hence an increase in these higher partial waves served both to maintain the good fit to the backward elastic  $K^-p$  data below 800 MeV/c while accommodating the larger cross-sections around 1000 MeV/c without the introduction of new resonances. The result of this new partial wave analysis without the addition of any new resonances is compared with the new data on the backward elastic cross-section in Fig. 23.

#### IV.3 Search for New Resonances

Resonant amplitudes were assumed to have the usual Breit-Wigner form:

$$T_R = \frac{\Gamma_e}{2(M-E) - i\Gamma} \quad (14)$$

where  $E$  is the center of mass energy,  $M$  the mass of the resonance,  $\Gamma_e$  its elastic width, and  $\Gamma$  its total width. Both the mass,  $M$ , and the elasticity  $x = \Gamma_e/\Gamma$  were free parameters.

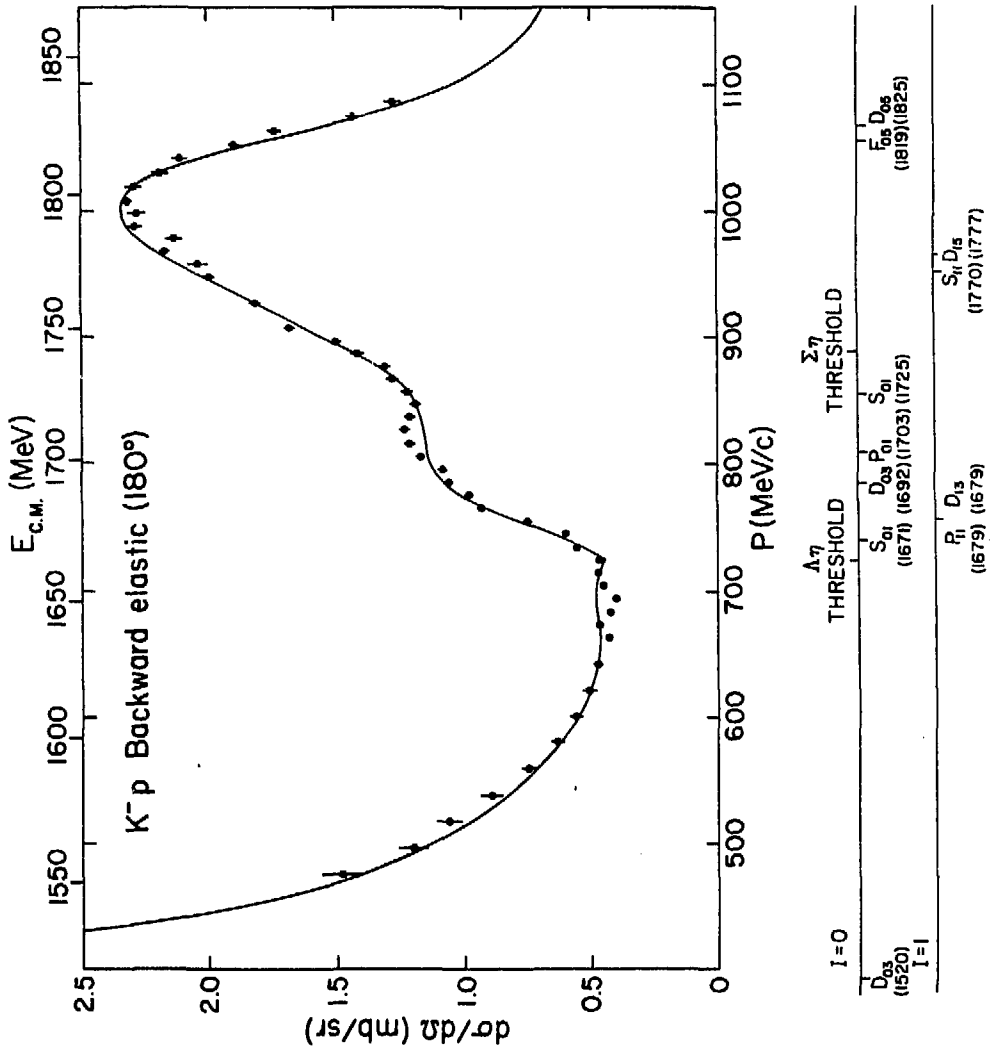


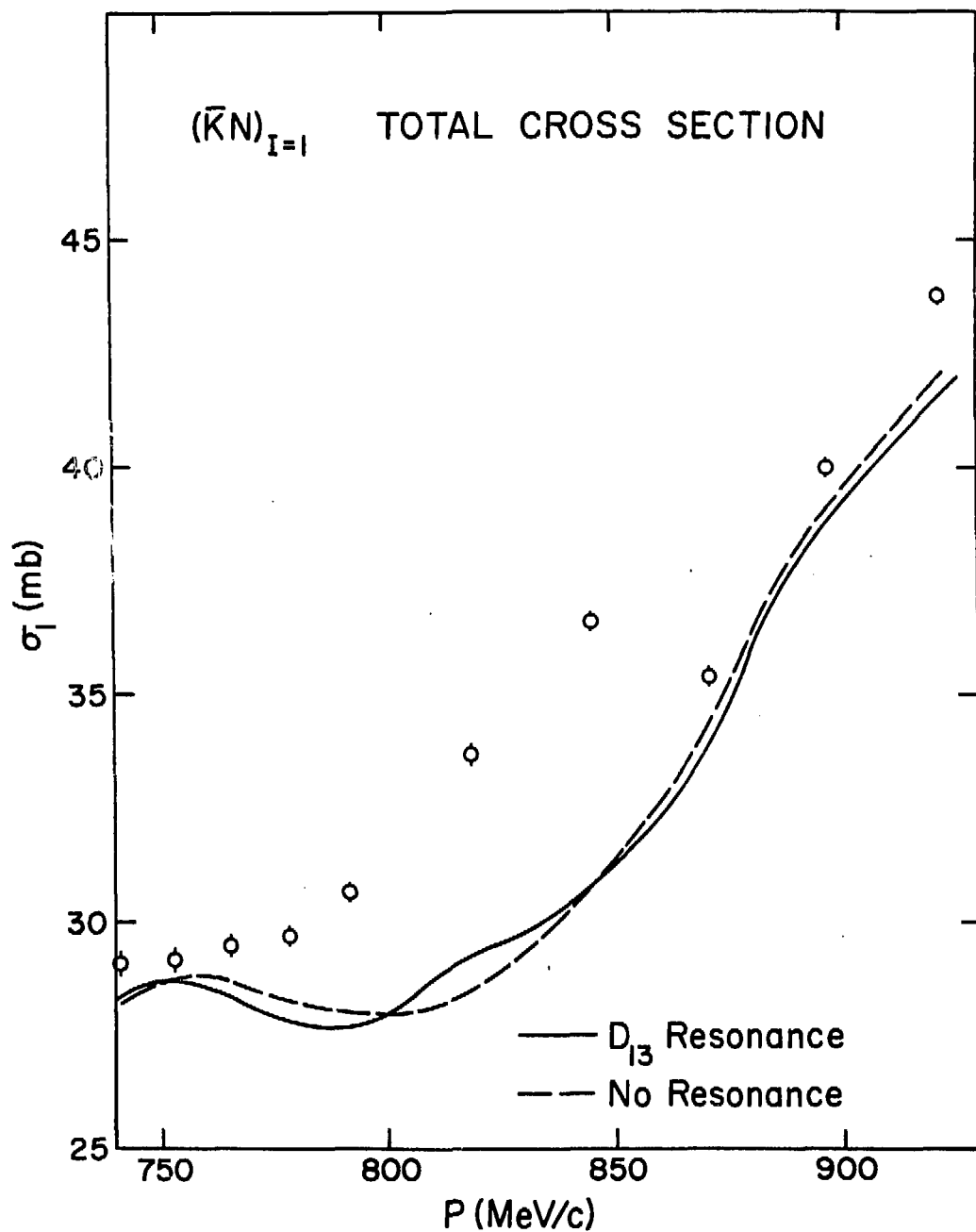
Figure 23. Results of this experiment and the new PWA (without the addition of new resonances) for  $\frac{d\sigma}{d\Omega} (\theta_{K^-} = 180^\circ)$  ( $K^-p \rightarrow K^-p$ )

As mentioned in Section I.1 a resonance in an even angular momentum partial wave produces an enhancement in the  $180^\circ$  cross-section while one in an odd partial wave produces a depression. Attempts were made to fit the structure between 800 and 850 MeV/c with resonances of both parities. Since the  $I=1$  total cross-section<sup>(38)</sup> (see Fig. 24) exhibits similar behavior in this region, only  $I=1$  resonances were considered. Of the three spin-parity ( $J^P$ ) assumptions tried ( $S_{11}$ ,  $P_{11}$ ,  $D_{13}$  where the notation is  $L_{I2J}$  as explained in Section I.1) only the  $D_{13}$  resonance gave a  $\chi^2$  lower than with no resonance but only marginally so ( $\chi^2(D_{13})=2933$ ,  $\chi^2$  (no resonance)=3017 with 1652 data points and 88 parameters). The results of the new analysis both with and without the inclusion of a  $D_{13}$  resonance are compared with the new backward elastic cross-section data in expanded detail in Fig. 25 for incident  $K^-$  momenta between 750 and 900 MeV/c.

As was the case in the earlier analysis, the  $I=1$  cross-sections are still poorly fit (see Fig. 24) despite the introduction of the new resonance. This analysis gives a mass of 1708 MeV for the  $D_{13}$  resonance while that of Carroll et al.<sup>(38)</sup> gives 1715 MeV on the basis of their  $I=1$  results. The  $I=0$  cross-sections are also poorly fit by the new analysis but the  $K^-p$  total cross-section which is the average of both isospin channels is fit quite well. The new analysis in particular does not require the introduction of any of the other resonances claimed by Carroll et al.<sup>(38)</sup>

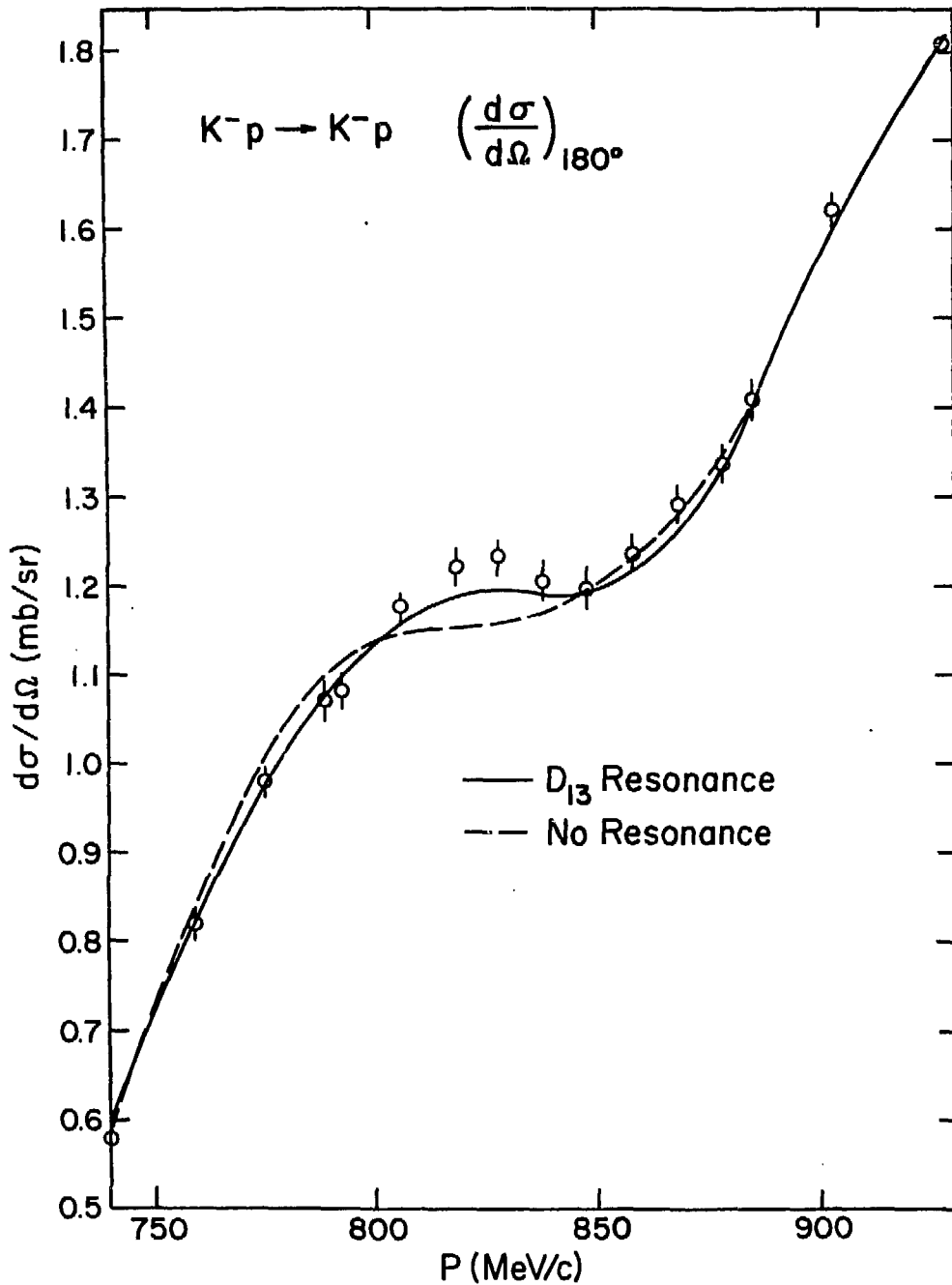
#### IV.4 Conclusions

The factor of 10 improvement in statistical precision in the measurement of the  $K^-p$  backward elastic cross-section achieved by this



XBL 798-11010

Figure 24. Comparison of the results of the new PWA and the  $I=1$   $\bar{K}N$  total cross-sections of Carroll et al. (Ref. 38) with and without a resonance between 800 and 850 MeV/c



XBL 798-11013

Figure 25. Results of the new PWA, with and without the inclusion of a  $D_{13}$  resonance, compared with the new backward elastic cross-section data

experiment now more clearly reveals the contributions of the previously known  $S = -1$  baryon resonances in this energy region (see Fig. 23). Furthermore, the enhancement between 800 and 850 MeV/c indicates that there no doubt is a new  $I=1$   $\bar{K}N$  resonance with a mass between 1700 and 1725 MeV as suggested by the total cross-section<sup>(38)</sup> and charge exchange<sup>(19)</sup> studies. Since the  $I=1$  total cross-section data are still not fit well by a partial wave analysis in the region of this resonance, its confirmation and an accurate determination of its parameters must await a remeasurement of the  $K^-p$  and  $K^-d$  total cross-sections using the higher intensity  $K^-$  beams and more suitable apparatus now available.

As mentioned in Section I.1, it now seems clear that the  $S = -1$  baryon resonances studied in this experiment are the excited states of the ground state  $\Lambda$  and  $\Sigma$ , which are bound states of a strange quark and up and down quarks. The new resonance between 1700 and 1725 MeV further enriches this spectrum. Hopefully, QCD or its successor will one day be able to calculate the masses of these resonances just as QED has determined the many energy levels of atoms.

APPENDIX 1  
DIFFRACTIVE SCATTERING

At large distances  $r$  from the scattering center a plane wave may be expanded in terms of Legendre polynomials as follows:

$$e^{ikz} = \frac{1}{2ikr} \sum_{\ell=0}^{\infty} (2\ell+1) P_{\ell}(\cos\theta) [e^{ikr} - (-1)^{\ell} e^{-ikr}] \quad (15)$$

The implied time dependence is  $e^{-i\omega t}$  so that the  $e^{ikr}$  term represents a spherical outgoing wave and the  $e^{-ikr}$  term an incoming wave. A diffractive scattering process modifies the outgoing wave by absorbing a positive real fraction  $\alpha_{\ell}$  of the outgoing wave in each angular momentum channel  $\ell$ . Physically this absorbed amplitude goes into inelastic channels. If a number of inelastic channels are open, as in  $K^{-}p$  scattering, this model describes the qualitative features of the scattering amplitudes quite well. The total outgoing wave is given by:

$$\psi_{\text{out}} = \frac{e^{ikr}}{2ikr} \sum_{\ell=0}^{\infty} (2\ell+1) (1-\alpha_{\ell}) P_{\ell}(\cos\theta) \quad (16)$$

The scattered wave is obtained by subtracting the unscattered outgoing part of the plane wave  $e^{ikz}$  from  $\psi_{\text{out}}$ :

$$\psi_{\text{scat}} = \frac{e^{ikr}}{r} \frac{1}{k} \sum_{\ell=0}^{\infty} (2\ell+1) \frac{i\alpha_{\ell}}{2} P_{\ell}(\cos\theta) \quad (17)$$

Comparing Eq. (17) with the usual definition

$$\psi_{\text{scat}} = f(\theta) \frac{e^{ikr}}{r} \quad (18)$$

gives

$$f(\theta) = \frac{1}{k} \sum_{\ell=0}^{\infty} (2\ell+1) \left(-\frac{i\alpha_{\ell}}{2}\right) P_{\ell}(\cos\theta) \quad (19)$$



which shows that for diffractive scattering the partial wave amplitudes  $T_\ell = \frac{i\alpha_\ell}{2}$  are positive imaginary. The Legendre polynomials add constructively only at  $\cos\theta = +1$  (where  $P_\ell(1) = 1$ ) so that at larger angles where the polynomials may have opposite signs (and thus add destructively)  $|f(\theta)|$  is small. As a result the differential cross-section, which is found from

$$\frac{d\sigma}{d\Omega} = |f(\theta)|^2. \quad (20)$$

is strongly peaked in the forward direction for diffractive scattering.

## APPENDIX 2

## MOMENTUM CALIBRATION

The actual momentum of the beam was checked with a measurement of the time-of-flight of anti-protons over a distance of 361.5 cm.<sup>(40)</sup> Pions and kaons were not used because they decay along the flight path and thus distort the time-of-flight measurement. The apparatus used for this calibration consisted of a fixed scintillation counter, M, and another scintillation counter, T, which could be moved from one end of the flight path to the other, trailing its coax cables so that their lengths remained unaltered. The time difference between a signal from M and one from T was measured with a TAC-PHA system calibrated by a time mark generator to one part in  $10^5$ .

After tuning the beam on anti-protons with a given nominal momentum, the zero point was found by measuring the time-of-flight from M to T with T placed closest to M. Then T was moved downstream by 361.5 cm and the measurement taken again to determine the time interval for the anti-proton to traverse that distance.

Table VIII gives the results of measurements at ten different "nominal momenta" that span the momentum range examined by this experiment. The "measured momentum" is the momentum of the anti-proton at the center of the 361.5 cm flight path as determined by the TOF calibration with corrections for  $dE/dx$  in the air. The "calculated momentum" is arrived at by subtracting the total momentum lost by the anti-protons in traversing the material upstream of this central point from the tuned "nominal momentum" at the mass slit. It is apparent from the table that the two values agree within a few tenths of a per cent. This is as

Table VIII

## Results of momentum calibration

Nominal Momentum (MeV/c)	Calculated Momentum	Measured Momentum	Percentage Error
440	366	363	+ .8%
480	422	419	+ .7%
520	474	472	+ .4%
560	520	521	- .2%
600	567	568	- .2%
700	676	679	- .6%
800	781	786	- .6%
900	884	886	- .3%
1000	986	990	- .4%
1080	1067	1071	- .4%

expected since previous momentum calibrations of this beam<sup>(33)</sup> were used to obtain the magnet current set points for the given nominal momentum.

All momentum values quoted in the main text are the mean interaction momenta of  $K^-$ 's in the liquid hydrogen target and are determined by subtracting  $dp/dx$  losses from the tuned nominal momentum as described above.

## APPENDIX 3

## DETAILS OF MONTE CARLO BACKGROUND DETERMINATION

The Monte Carlo program calculated the background proton rate from the decay of final state hyperons in the inelastic reactions  $K^-p \rightarrow \Lambda\pi^0, \Sigma^+\pi^-, \Sigma^0\pi^0, \Sigma\pi\pi, \text{ and } \Lambda\pi\pi$ . The program began by generating incident kaons at a randomly selected point in counter S1 from which they traveled a straight line to the target through another randomly selected point in counter S2 (see Section II.1 and Fig. 4). The momentum of the kaon was chosen from a triangular distribution that fell to zero for  $\Delta p/p = \pm 2\%$  about the nominal beam momentum being studied.

The distribution of interaction points of kaons in the target reflected the attenuation of the incident kaon beam due to decay and nuclear interactions in the liquid hydrogen. After recomputing the momentum of the  $K^-$  to account for  $dp/dx$  losses in the target to the interaction point, the kinematics for the  $K^-p$  interaction were generated in the center of mass using Legendre polynomial parameterizations of the distributions obtained from the RLIC partial wave analysis<sup>(21)</sup> for  $\Lambda\pi$  and  $\Sigma\pi$  and isotropic production of  $\Sigma(1385)\pi$  ( $\Lambda(1520)\pi$ ) followed by isotropic decay of the resonance to  $\Lambda\pi$  ( $\Sigma\pi$ ) for  $\Lambda\pi\pi$  ( $\Sigma\pi\pi$ ). The decays of the hyperons,  $\Lambda \rightarrow p\pi^-, \Sigma^+ \rightarrow p\pi^0, \text{ and } \Sigma^0 \rightarrow \Lambda\gamma$  followed by  $\Lambda \rightarrow p\pi^-,$  were all generated isotropically in the rest frame of the decaying particle. The resulting proton was then followed through the rest of the apparatus allowing for momentum loss and absorption in the target. Protons that hit the P-counter were tracked through the spectrometer by means of the usual first order matrix representation for beam optics.<sup>(36,41)</sup> The final distribution of protons on the hodoscope took into account multiple scattering in the material downstream of the interaction point.

It was observed experimentally that the center of the elastic peak was not always the central bin of the hodoscope distributions. Since the Monte Carlo program was designed so that elastically scattered  $0^0$  protons from on-momentum  $K^-$ 's hit the central bin, it was necessary to shift the Monte Carlo background distributions several bins toward the low or high momentum sides of the hodoscope to approximate the experimental situation as closely as possible. Finally, since every  $K^-$  generated by the Monte Carlo interacted in the target, the number of Monte Carlo events,  $N_{MC}$ , was chosen to correspond to the experimental  $K^-$  flux:

$$N_{MC} = BK \cdot n_p \cdot \sigma_r \cdot b \quad (21)$$

$BK$  = number of incident kaons

$n_p$  =  $8.563 \times 10^{-4}$  protons/mb in the  $LH_2$  target

$\sigma_r$  = the integrated cross-section for the reaction

$b$  = branching ratio for the hyperon decay to a proton

Because events were generated over the full  $4\pi$  solid angle, it was necessary to use the integrated cross-sections,  $\sigma_r$  (obtained from the RLIC<sup>(21)</sup> analysis for  $\Sigma\pi$  and  $\Lambda\pi$  and from a smooth fit to the data for  $\Lambda\pi\pi$  and  $\Sigma\pi\pi$ ), in the above calculation. Figure 26 is a breakup of the total Monte Carlo background into the contributions from each reaction channel plotted as events versus hodoscope channel at 1007 MeV/c. Most background protons come from  $K^-p \rightarrow \Lambda\pi^0$  while the contribution of the  $\Sigma\pi\pi$  channel is essentially negligible. The size of the background falls rapidly on the high momentum side of the hodoscope since the phase space available for production of protons near the maximum allowed momentum is small.

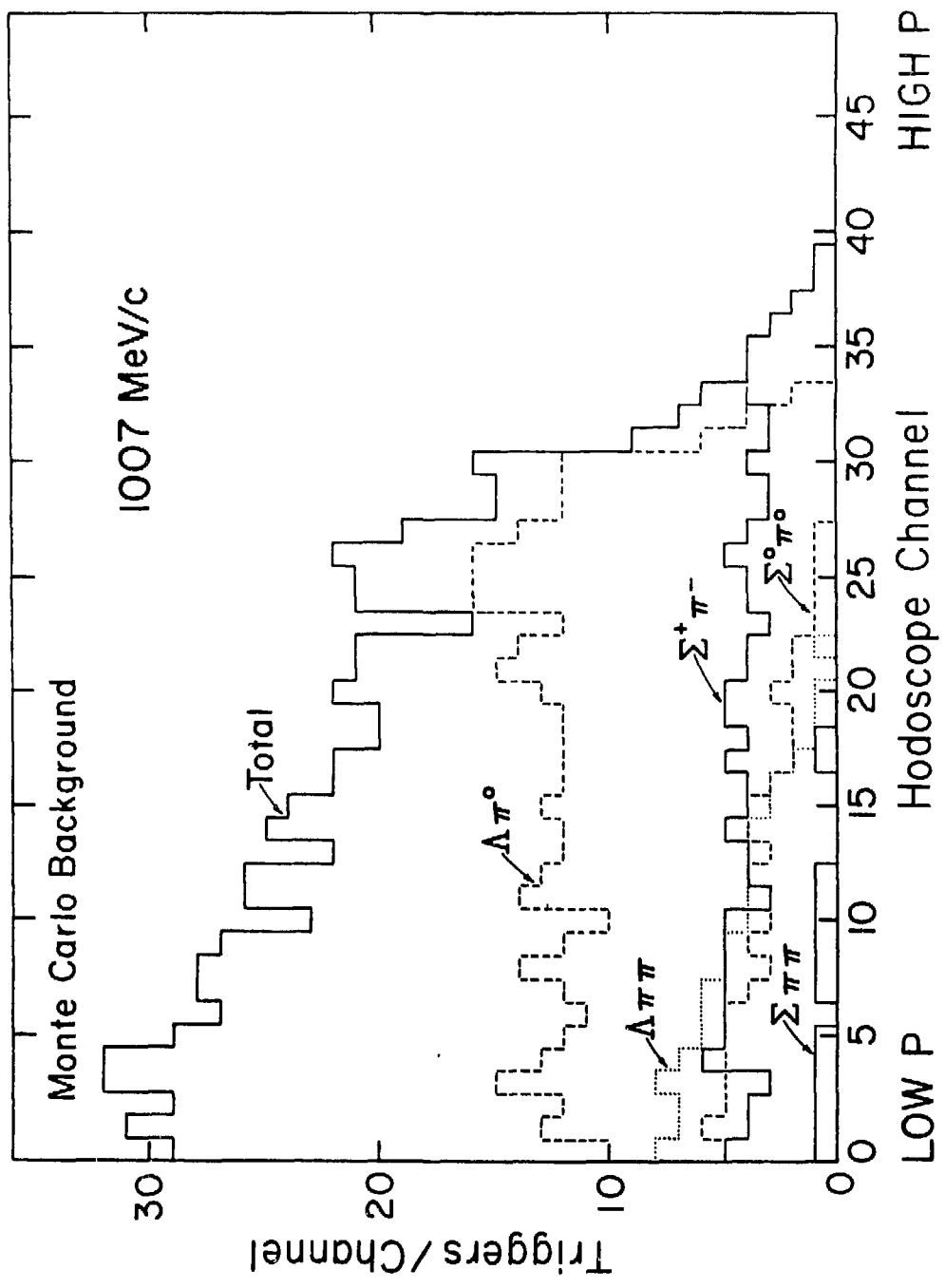


Figure 26. Monte Carlo predicted background for reactions  $\Lambda\pi^0$ ,  $\Lambda\pi\pi$ ,  $\Sigma^+\pi^-$ ,  $\Sigma^0\pi^0$ , and  $\Sigma\pi\pi$  normalized to the experimental beam flux (in units of  $10^6$  K<sup>-</sup>'s) at 1007 MeV/c

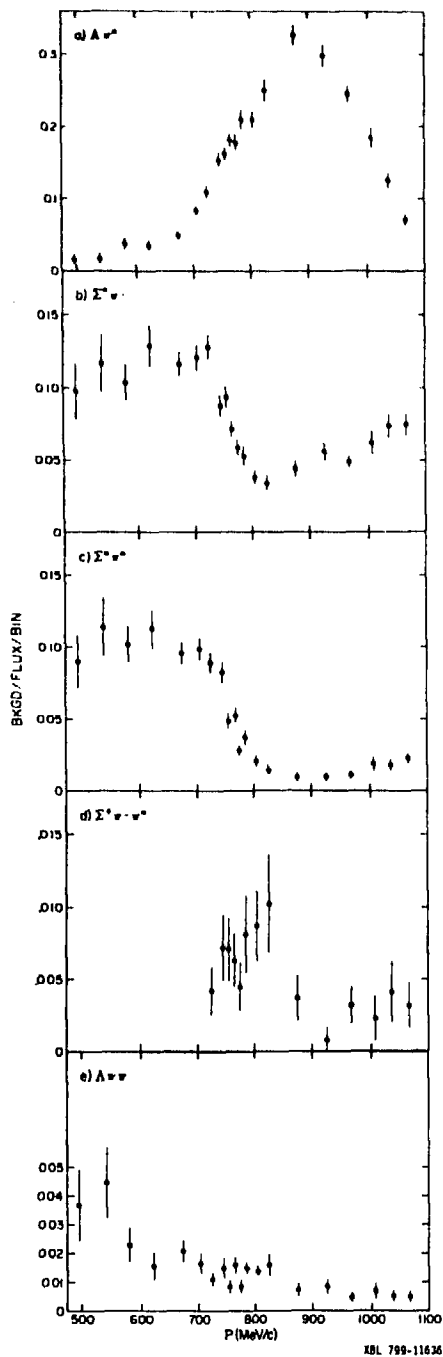


Figure 27. Contribution of each reaction channel to the Monte Carlo background as a function of incident  $K^-$  momentum



The complicated momentum dependence of the Monte Carlo background has already been mentioned. Figure 27, which shows the momentum dependence of the background from each reaction channel, indicates that the reason for this is the large variations of the background contributions from individual reactions over the momentum range.

## APPENDIX 4

### CORRECTIONS

The correction factors discussed here account for a number of small effects, none of which exceeded a few per cent in magnitude. Many of these factors introduced changes in the final answer that were less than the statistical errors on the data so that rigorous calculational techniques were not required.

#### A. Background scattering in target ( $C_7'$ )

Equation (13) singled out the correction factor  $C_7'$  from all others, it being required in the target-empty subtraction. All other correction factors were multiplicative. The factor  $C_7'$  accounted for the scattering in hydrogen of background secondaries, nearly all of which were produced upstream of the liquid hydrogen target. Thus the counting rate observed when the target was empty was not a true representation of the corresponding background component of the counting rate when the target was full because those particles in the background coming from upstream of the hydrogen target were scattered in the filled hydrogen target and some did not reach the hodoscope.  $1/C_7'$  is given by the usual expression for attenuation of the secondary proton beam in the 20.96 cm of LH<sub>2</sub>:

$$1/C_7' = \exp(-n_p \sigma_T) \quad (22)$$

$n_p = 8.563 \times 10^{-4}$  protons/mb for the LH<sub>2</sub> target used in this experiment.

$\sigma_T = K^-p$  total cross-section from references 42 and 43.

The momentum dependence of  $C_7'$ , which ranged from 1.020-1.037, is displayed in Fig. 18. The effect of  $C_7'$  was ignored in the background determination because its small value was masked by larger statistical

fluctuations in the number of background events.

## B. Corrections to beam flux and $K^-$ track length in the target

### 1. Beam Contamination ( $C_1$ )

Since the Cerenkov counter was not 100% efficient in rejecting  $\pi$ 's and  $\mu$ 's in the beam, a correction had to be made for beam contamination. Protons from  $\pi p$  backward elastic scatters had momenta too high to fall inside the  $K^- p$  elastic peak on the hodoscope while protons from wider angle  $\pi p$  scatters missed the P counter. Thus beam contamination did not affect the number of events and the cross-section was scaled upward to account only for overcounting of the incident kaon flux.

If the pion rejection,  $R$ , and kaon identification efficiency,  $\epsilon_K$ , of the Cerenkov counter are known, the contamination can be calculated from the measured beam particle to beam "kaon" ratio,  $BD/BK$ , as follows:

$$N_\pi + N_K = BD$$

$$\frac{N_\pi}{R} + \epsilon_K N_K = BK$$

$$\text{so, } \pi \text{ contamination} = \frac{N_\pi/R}{BK} = \frac{\epsilon_K}{R\epsilon_K - 1} \left( \frac{BD}{BK} - \frac{1}{\epsilon_K} \right) \quad (23)$$

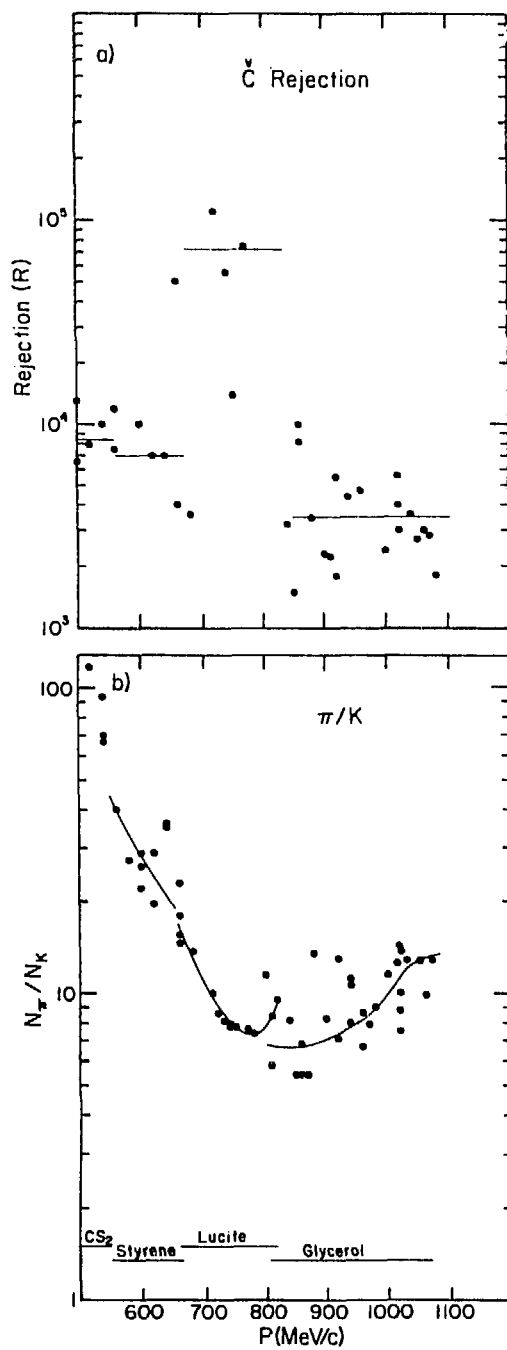
$$\text{for } R \gg 1 \quad \approx \frac{1}{R} \left( \frac{BD}{BK} - \frac{1}{\epsilon_K} \right)$$

where,

$N_\pi (N_K)$  = Actual number of pions (kaons) in the beam

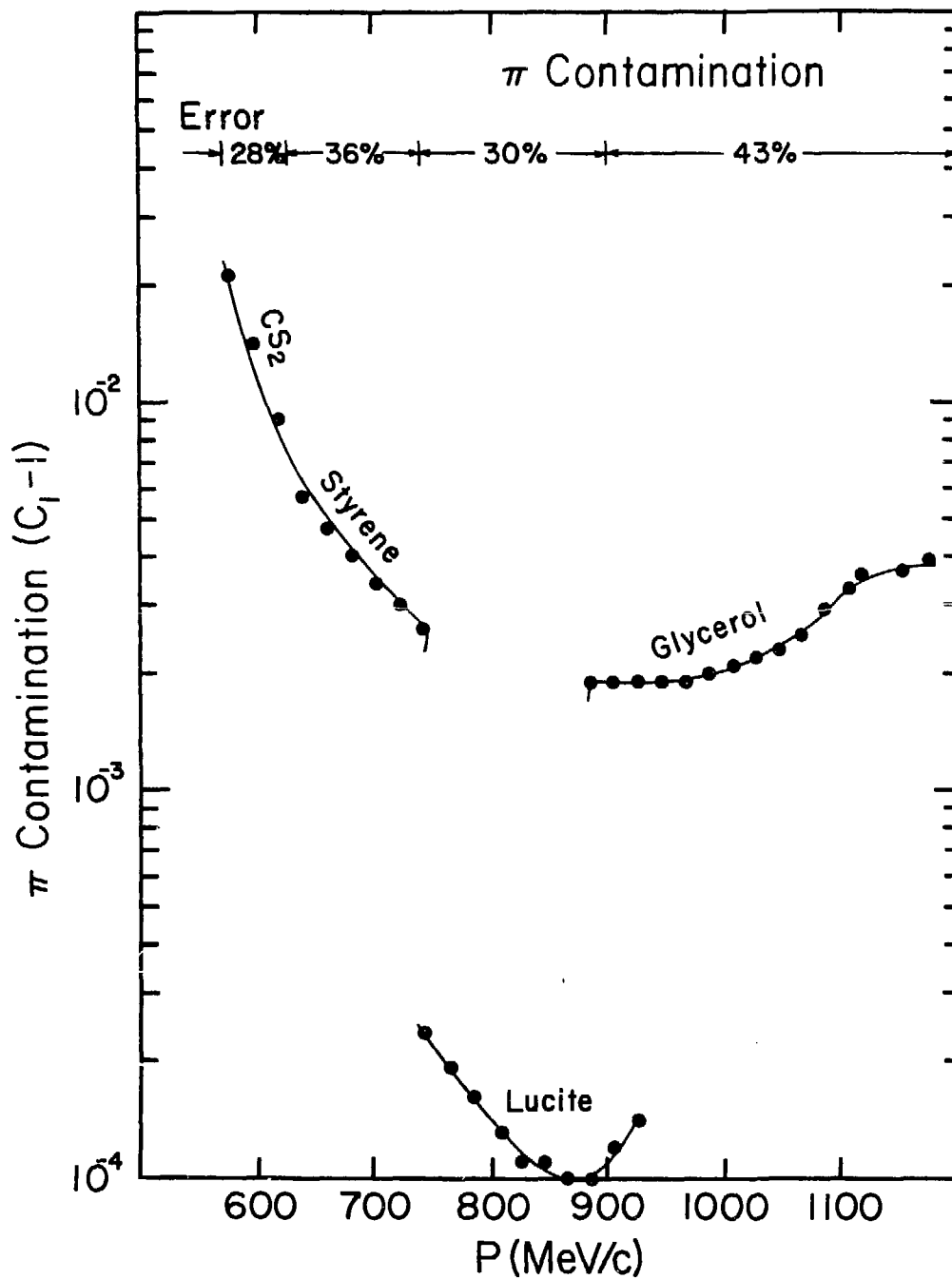
$BD(BK)$  = Measured number of incident beam particles (kaons).

The pion rejection was measured at a number of the momenta by tuning the beam separator for pions and observing how many  $\pi$ 's were misidentified as by  $K$ 's by the Cerenkov counter. Figure 28 shows the results of those



XBL 799-11624

Figure 28. Measured  $\pi$  rejection and  $N_\pi/N_K$  ratios



XBL 799-11616

Figure 29. Correction for  $\pi^-$  contamination of  $K^-$  beam

measurements as well as the measured  $N_{\pi}/N_K \approx BD/BK-1$  ratios. Figure 29 displays the calculated values for the  $\pi$  contamination. The sharp discontinuities from one momentum region to the next are the result of using different Čerenkov cells in different momentum regions as noted on the figure. The smooth curve fits to the  $N_{\pi}/N_K$  ratio and the rejection were used to obtain the final values for the beam contamination. The errors on the  $N_{\pi}/N_K$  ratio and rejection values are estimates of the scatter of the data in each momentum range and were added in quadrature to obtain the final error on the contamination. Although these errors are quite large  $\sim 30\%$ , the effect on the final cross-section results is minimal because the contamination correction is typically only a few tenths of a percent or less except at the lowest momenta (see Fig. 29).

## 2. Kaon decay between Čerenkov and $S_2$ counters ( $C_2$ )

From 6-12% (depending on the momentum) of the kaons identified as such by the Čerenkov counter decayed before reaching  $S_2$ . If any of their charged decay products ( $\pi$ 's or  $\mu$ 's) hit both M and  $S_2$  (or just  $S_2$  if the decay took place between M and  $S_2$ ) they would be wrongly identified as beam kaons. As a result BK is an overestimate of the kaon flux and the measured cross-section must be increased by a factor:

$$C_2 = [1 - \Delta/N_K]^{-1} \quad (24)$$

where  $\Delta$  is the number of charged particles from kaon decays that fake a beam kaon if  $N_K$  kaons are identified by the Čerenkov counter.

The Monte Carlo program mentioned in Section III.1 generated  $N_K=10^5$  kaons at the Č counter exit and decayed them between Č and  $S_2$  according

to:

$$dN_K = \frac{N_K}{\eta c \tau} \exp(-z/\eta c \tau) dz \quad (25)$$

where,

$dN_K$  = the number of kaons that decay in the interval  $dz$  a distance  $z$  downstream of the  $\checkmark$  counter

$$\eta = P_K^- / m_K^-$$

$$c\tau = 370.9 \text{ cm for } K^- \text{'s}$$

Only the decay modes  $\mu^- \bar{\nu}$ ,  $\pi^- \pi^0$ , and  $\pi^- \pi^+ \pi^-$  were considered. The paths of the charged decay products were followed and if they produced a signal in M and/or  $S_2$  the number  $\Delta$  was incremented. Kaons that decayed downstream of  $S_2$  comprise the correction factor  $C_4$ .  $C_4$  was discovered to have a constant value of  $1.0098 \pm .0002$  over the entire momentum range (see Fig. 18).

### 3. Kaon interaction in counter $S_2$ ( $C_3$ ).

Kaons that interacted in counter  $S_2$  and were lost would still give a signal and thus be counted in the incident flux  $\Delta$ . Consequently, the measured cross-section had to be scaled upward by a factor

$$C_3 = \exp \left( \frac{\rho L}{A} N_0 \sigma_{K,S} \right) \quad (26)$$

to account for the attenuation of the kaon beam in  $S_2$ . The factor  $\frac{\rho L}{A} N_0$  is explained after Eq. (13) (see Section III.1). The absorption cross-section for kaons on scintillator material,  $\sigma_{K,S}$ , was estimated to be 271 mb over the whole momentum range by first subtracting the cross-section for small angle diffractive scattering from the total cross-section for kaons on carbon<sup>(39,44)</sup> and then scaling the result to

scintillator which contains both carbon and hydrogen. It was also possible for kaons to interact in M and send charged particles into  $S_2$  and thus fake an incident beam kaon. However, since  $S_2$  subtends a solid angle of only 200 msr at M this effect is negligible. The correction factor,  $C_3$ , was found to be only  $1.0041 \pm 0.0005$ .

#### 4. Kaon decay from $S_2$ through hydrogen target ( $C_4$ )

The correction  $C_2$  already takes into account the decay of kaons between  $\check{C}$  and  $S_2$ . This correction,  $C_4$ , merely reflects the attenuation of the kaon beam due to decays downstream of the last beam defining counter,  $S_2$ . For  $N_K$  kaons emerging from  $S_2$  the number of  $K^-p$  backward elastic scatters in the hydrogen target,  $N_{SC}$ , is given by

$$\begin{aligned}
 N_{SC} &= \int_{\ell'}^{\ell} dz N_K e^{-z/\eta c\tau} \frac{\rho}{A} N_o \frac{d\sigma}{d\Omega} \Delta\Omega \\
 &= N_K \left[ \frac{\eta c\tau}{\ell - \ell'} (e^{-\ell'/\eta c\tau} - e^{-\ell/\eta c\tau}) \right] \frac{\rho(\ell - \ell')}{A} N_o \frac{d\sigma}{d\Omega} \Delta\Omega
 \end{aligned} \tag{27}$$

In this equation  $z$  represents the distance along the beam line downstream of  $S_2$  so that the factor  $e^{-z/\eta c\tau}$  accounts for the attenuation of the incident kaon beam due to decays (where  $\eta = P/m$  is the ratio of the  $K^-$ 's momentum to its mass and  $c\tau = 370.9$  cm for kaons). The integrand is the number of the backward scatters in the interval  $dz$  in the target while the limits of integration,  $\ell' = 6.27$  cm and  $\ell = 26.59$  cms, are, respectively, the distances of the upstream and downstream target flask windows from  $S_2$ . Comparison with Eq. (12) shows that the measured  $d\sigma/d\Omega$  must be corrected by

$$C_4 = \frac{\ell - \ell'}{\eta c\tau} \left[ e^{-\ell'/\eta c\tau} - e^{-\ell/\eta c\tau} \right]^{-1} \tag{28}$$



The momentum dependence of this correction factor, which ranged between 1.02 and 1.05, is shown in Fig. 18.

### 5. Kaon interactions in the hydrogen target ( $C_5$ )

This factor corrects for the loss of incident kaon flux due to  $K^-p$  interactions in the liquid hydrogen target. The derivation of the formula for  $C_5$  involves the same considerations involved in calculating  $C_4$  with the beam attenuation determined by  $\frac{\rho N_0}{A} \sigma_T(K^-p)$  instead of  $1/\eta\sigma_T$ . The result is

$$C_5 = \frac{N_0 L}{A} \sigma_T \left[ 1 - \exp\left(-\frac{\rho N_0 L}{A} \sigma_T\right) \right]^{-1} \quad (29)$$

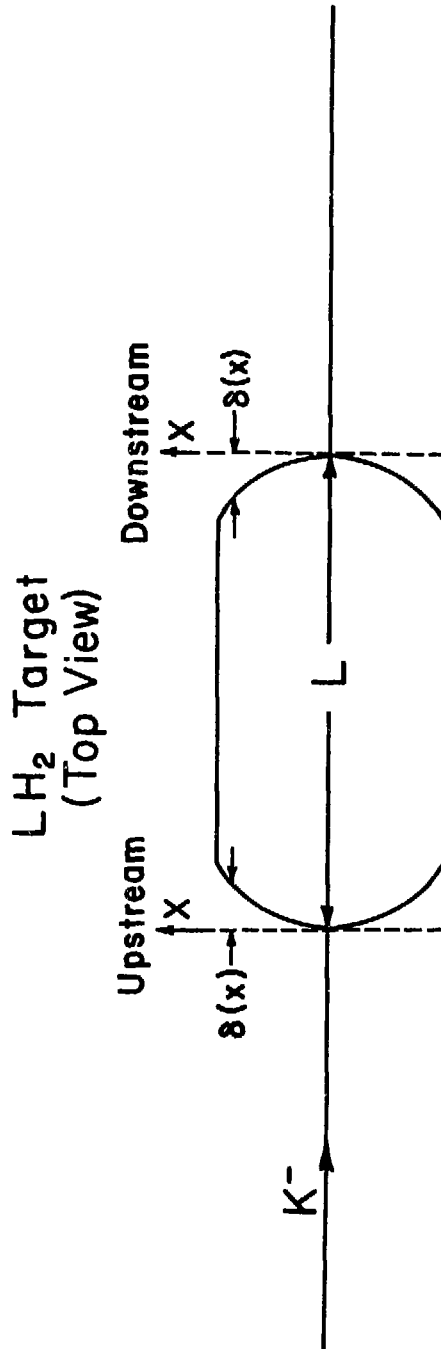
where  $\sigma_T$  is obtained from the smooth fit to the available  $K^-p$  total cross-section data<sup>(45)</sup> and the other factors are defined after Eq. (13).  $C_5$  is plotted in Fig. 18 and varies between 1.015 and 1.023 over the whole momentum range.

### 6. Effective target length ( $C_6$ )

Since the ends of the cylindrical hydrogen target were curved, particles that entered the target off axis traversed a distance shorter than the axial length  $L$  used in Eq. (13). To a good approximation (due to the small vertical extent of the beam at the target) the difference between  $L$  and the effective target length due to the curvature of one end of the target is given by

$$\langle \delta \rangle = \int_H I(x) \delta(x) dx / \int_H I(x) dx + \int_V I(y) \delta(y) dy / \int_V I(y) dy \quad (30)$$

where the first integral is over the horizontal extent of the beam spot and the second over the vertical.  $\delta(x)$  as defined in Fig. 30, which shows the profile of the target flask, was measured on an accurate X-ray



XBL 799-11617

Figure 30. Sketch of target showing parameters used in determining its effective length

photograph of the target flask. The horizontal distributions of beam kaons,  $I(x)$ , were obtained by projecting the trajectories (as determined by the wire chambers for each  $K^-$  that produced a trigger) to the upstream and downstream ends of the target. Since the vertical half-width of the beam spot at the target was only .95 cm and since the wire chambers provided no information on the vertical beam profile, the vertical distributions,  $I(y)$ , were assumed to be triangular with a base half width of .95 cm. The value  $\langle \delta \rangle$  was calculated by numerical integration at both ends of the target taking into account the different horizontal distributions at each end. The overall deviation of the effective length from the axial length is then given by the sum of the upstream and downstream end calculations:

$$\Delta = \langle \delta_u \rangle + \langle \delta_d \rangle \quad (31)$$

The resulting correction scales the cross-section upward by a factor:

$$C_6 = [ 1 - \Delta/L ]^{-1} \quad (32)$$

$C_6$  was calculated at several momenta and found to have a constant value of  $1.0230 \pm 0.0005$  as expected from the fact that the same focusing conditions at the target were used at each momentum.

### C. Loss of protons

#### 1. Geometric acceptance of spectrometer and loss of protons due to scatters in the target. (C<sub>7</sub>)

In order to maximize the counting rate, the P counter, which defined the solid angle  $\Delta\Omega_{1ab}$  in Eq. (13), was made slightly larger than the geometric acceptance of the spectrometer. As a result some of the forward scattered protons were lost due to scraping at the spectrometer magnet apertures. This was particularly true at low momenta.

To calculate this correction the Monte Carlo program generated elastic  $K^-p$  collisions in the target for center of mass angles between the incident and final kaon of  $150^\circ$  to  $180^\circ$ . Angles less than  $150^\circ$  were not considered because protons from such wide angle scatters missed the P counter. By using a probability distribution that depended on the proton-proton total cross-section and the path length of the scattered proton in the liquid hydrogen, a check was made to see if the proton interacted in the target. Protons that did were assumed to be lost. Of course, some of these "lost" protons were protons that would have hit the P counter had they not interacted in the hydrogen. This fact was taken into account in the final calculation of  $C_7$  as explained below.

The trajectories of all protons that hit the P counter were followed through the spectrometer to the hodoscope and those protons that failed to meet the aperture requirements at the entrance or exit of each magnet were lost. The resulting correction factor for loss of secondary protons is

$$C_7 = (P + \frac{P}{N} S)/H \quad (33)$$

where,

$N$  = the number of Monte Carlo generated  $K^-p$  collisions, typically  $10^5$ ,

$P$  = the number of protons from those  $N$  events that hit the P counter,

$S$  = the number of protons lost due to interactions in the hydrogen target,

$H$  = the number of protons that ultimately reach the hodoscope.

This relation assumes, as a good approximation, that the same fraction,  $P/N$ , of protons that were lost through interactions in the target would

have hit the P counter as were generated.  $C_7$  was found to vary smoothly between 1.04 and 1.06 over the whole momentum range (see Fig. 18).

### 2. $\pi^+$ decays in $K^-p \rightarrow \Sigma^-\pi^+$ ( $C_8$ )

This correction applies only to the measurement of the differential cross-section for  $K^-p \rightarrow \Sigma^-\pi^+$  and is described in Appendix 6. For backward elastic  $K^-p$  scattering  $C_8$  is exactly unity.

### 3. Self veto ( $C_9$ )

The lead collimator and the high threshold M counter veto circuit (see Sections II.2 and II.6) were designed to reduce the vetoes of beam particles that produced backscattered  $K^-$ 's. Such  $K^-$ 's or their decay products, pions and muons, could, in principle, reach the Čerenkov counter and veto good  $K^-p \rightarrow K^-p$  events by producing a false "pion" signal and thereby lead to a cross-section value that was too small. To make sure that this effect was indeed small, the Monte Carlo program was run with several simplifying assumptions incorporated to make the problem tractable.

The Monte Carlo program not only followed the paths of forward scattered protons from  $K^-p \rightarrow K^-p$  but could also determine the fate of the backscattered  $K^-$  as well. The energy deposited in the M counter by a backward going  $K^-$  was checked and if found to be greater than 2.5 times that for a minimum ionizing  $K^-$  it was assumed that the high threshold M counter veto circuit fired and the good  $K^-p \rightarrow K^-p$  event was not vetoed. However, any  $K^-$ 's that missed M or any that decayed before reaching M to  $\pi$ 's and  $\mu$ 's that are always essentially minimum ionizing would not trigger the veto circuit and could potentially cause trouble if not stopped by the lead wall.

For the Monte Carlo calculation the lead wall was assumed to be infinitesimally thin but with a density of  $115 \text{ g/cm}^2$ , of infinite extent with a  $10.16 \text{ cm} \times 5.08 \text{ cm}$  hole, and located at the upstream end of the actual lead wall. All backscattered  $K^-$ 's that hit the lead were assumed to stop because their low energy gave them insufficient range to penetrate the lead wall.  $\pi$ 's and  $\mu$ 's that hit the lead were assumed to lose energy corresponding to the traversal of  $115 \text{ g/cm}^2$  of lead.

Particles that penetrated the lead or passed through the hole and hit the  $\checkmark$ erenkov cell were considered to be normally incident to the cell surface. As a check on the systematic error of the calculation two conditions for producing a false veto in the  $\checkmark$ -counter were considered: (1) all particles with a velocity large enough to produce  $\checkmark$  light in the cell caused a veto and (2) only those particles that produced  $\checkmark$  light at an angle sufficiently large to be internally reflected (see the description of the  $\checkmark$ -counter in Section II.2) caused a veto. Figure 31 shows the Monte Carlo results for both conditions. It was found that no false vetoes were produced by kaons and that what few vetoes did occur were caused mainly by the small number of  $\pi$ 's and  $\mu$ 's from  $K^-$  decay that went through the hole in the lead.

For the sake of calculation it was estimated that all particles of type (2) (as defined above) vetoed good events while only 10% of type (1) did so. The result of this estimate of  $C_g$  is shown as the solid line in Fig. 31. All values of  $C_g$  shown in Fig. 31 were obtained from

$$C_g = [1 - \Delta/N]^{-1} \quad (34)$$

where  $\Delta$  is the number of false vetoes resulting from  $N$  backward elastic  $K^-p$  events. It is important to note that in no case is the correction

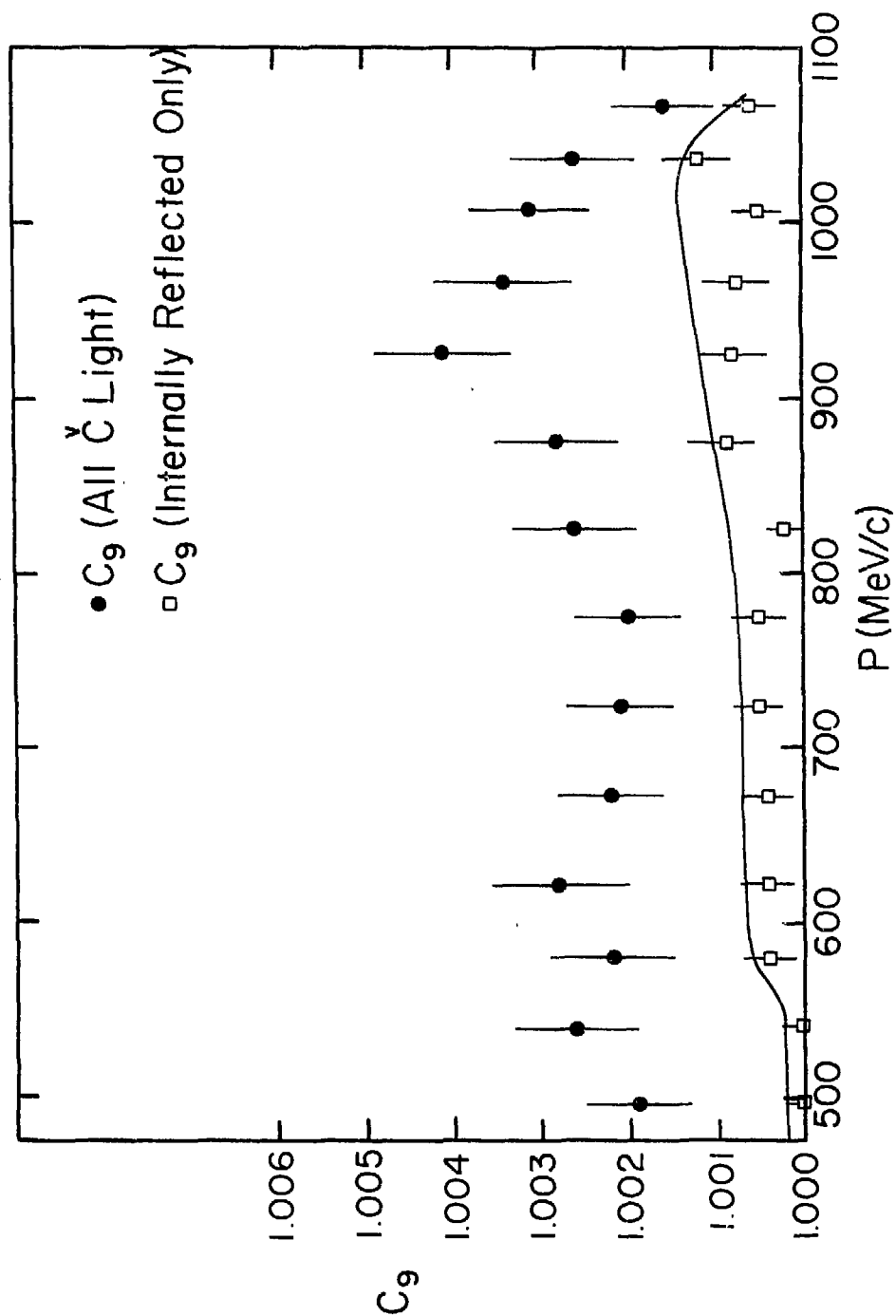


Figure 31. Correction factor  $C_9$  calculated under the two conditions described in Appendix 4.C.3

factor larger than a few tenths of one per cent so that any systematic error in its evaluation is masked by the much larger statistical errors in the data.

#### 4. Interactions of protons in the P counter and the air column in the spectrometer ( $C_{10}$ ).

This correction accounts for the absorption of forward scattered protons in the material downstream of the target in the same way that  $C_3$  corrects for absorption of the  $K^-$  beam. To calculate this correction the absorption cross-sections for protons in air and scintillator were assumed to be constant over the whole momentum range of the experiment. The scintillator cross-section was estimated to be 240 mb by scaling the  $pC^{12}$  cross-section <sup>(39)</sup> while the cross-section in air was chosen to be 260 mb from  $pN^{14}$  data. <sup>(39)</sup> The constant value of  $C_{10}$  was found to be 1.014.



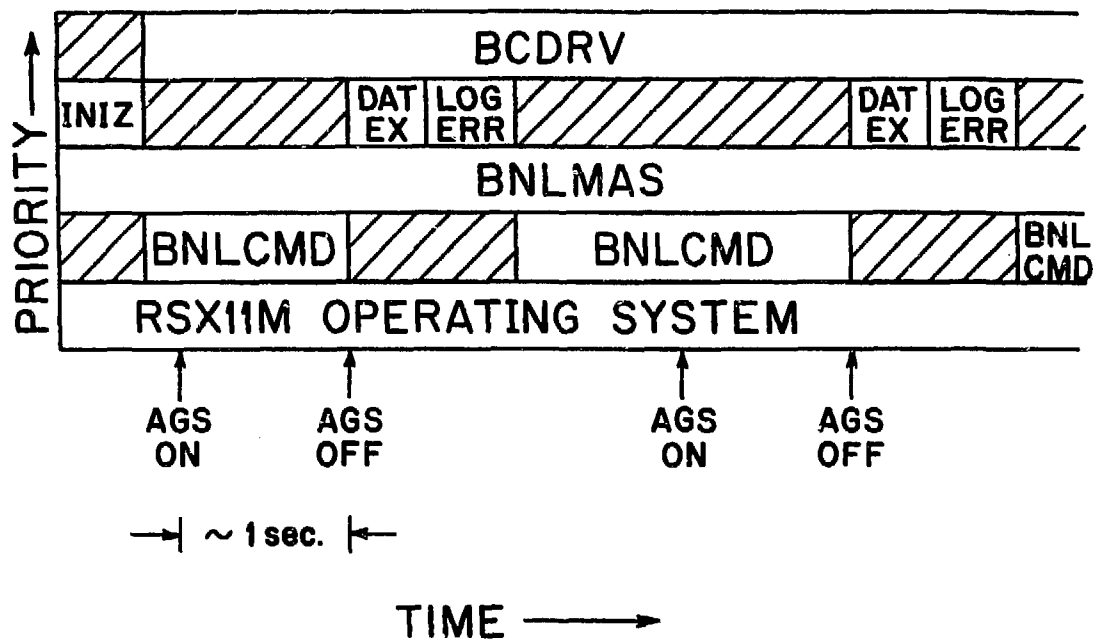
## APPENDIX 5

## ON-LINE COMPUTER PROGRAM

The data acquisition for this experiment was handled by a PDP-11/34 computer using the RSX11M operating system.<sup>(46)</sup> The structure of the data acquisition program was constrained by the features of the operating system and the fact that this particular 11/34 only had 48 K of memory of which 20 K was occupied by the operating system. To provide some help to those laboring under similar constraints, this structure is outlined here.

The entire data-taking system (a multi-task structure) consisted of several programs<sup>(47)</sup> that appear in Fig. 32 on a diagram of the priority of the program versus the time it was run relative to the spill times from the AGS. The program BNLMAS was in core at all times and scheduled the running of the other tasks. When the system was first loaded, the task INIZ initialized the global storage area.

The routine BNLCMD ran next and processed all commands entered by the experimenters at the terminal (e.g., start and stop data-taking, display histograms, etc.). Once data-taking was initiated the software interface to CAMAC, BCDRV, was activated and could interrupt any other task whenever the CAMAC modules contained data to be read into the computer. Any one of three such signals could generate an interrupt: (1) the start of the AGS flat-top which caused BCDRV to prepare the data buffers for incoming data; (2) an event trigger on which BCDRV read the TDC, ADC, hodoscope latchbox, and wire chamber information into memory, and (3) an AGS off pulse which prompted the reading of the CAMAC scalers. After interrupt (3) had occurred and the scalers were read, the program



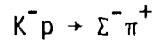
- BCDRV - I/O driver or software interface to CAMAC
- INIZ - Initialization routine for program and CAMAC
- DATEX - Data examination, organization, and output to tape
- LOGERR - Prints out error messages
- BNLMAS - Master routine, synchronizes scheduling of all routines
- BNLCMD - Processes commands from terminal, prints out histograms, etc.
- RSX11M - Operating system

Figure 32. Diagram of data-taking system used on the PDP 11/34

DATEX was scheduled to process the data and no other task could run.

DATEX took the raw data from CAMAC and converted it to a more useful form before writing it to tape. This included converting a binary encoded hit pattern from the wire chambers to the actual numbers of the wires hit and also converting the signals from the 23 hodoscope scintillator slats to the number(s) corresponding to which of the 45 hodoscope channels contained an event (see Section II.5). If either BCDRV or DATEX detected an error the task LOGERR was scheduled by BNLMAS, interrupted any output to the terminal, and printed the error message. Once DATEX (and LOGERR if run) was complete, data-taking resumed and BNLCMD could again accept input from the experimenters.

## APPENDIX 6

A. General discussion

The same apparatus used for the measurement of the  $K^- p$  backward elastic cross-section can also be used to study other two-body final states provided one of the particles has a lifetime sufficiently long to reach the hodoscope. In order to avoid a large contamination of the trigger signal by unscattered beam particles, one is limited to particles of charge opposite in sign to the beam. Hence the reaction  $K^- p \rightarrow \Sigma^- \pi^+$  where the  $\pi^+$  emerges at  $0^\circ$  was also investigated.

Figure 33 displays the data for this reaction that existed prior to this experiment, which, as in the case of the  $K^- p$  backward elastic data, has a statistical precision of only 30%. The figure also displays the results of RLIC partial wave analysis (PWA)<sup>(21)</sup> for this channel. Both the PWA and the three experiments referenced in the figure<sup>(11,13,17)</sup> are discussed in Section I.2. The data do not exhibit as much structure as in  $K^- p \rightarrow K^- p$  but some gross features are apparent. The high energy tail of the  $\Lambda(1520)$  resonance accounts for the larger cross-section below 500 MeV/c while several resonances ( $\Lambda(1671)$ ,  $\Lambda(1692)$ ,  $\Sigma(1679)$  ( $P_{11}$ ) and  $\Sigma(1679)$  ( $D_{13}$ )) are responsible for the broad enhancement between 650 and 800 MeV/c. The rise in the cross-section above 1000 MeV/c is attributable to the  $\Lambda(1819)$  and  $\Lambda(1825)$  resonances but is not as prominent as the bump in the elastic cross-section (see Section I.2) because the  $\Sigma(1770)$  and  $\Sigma(1777)$  have only a small branching ratio for the  $\Sigma\pi$  channel.

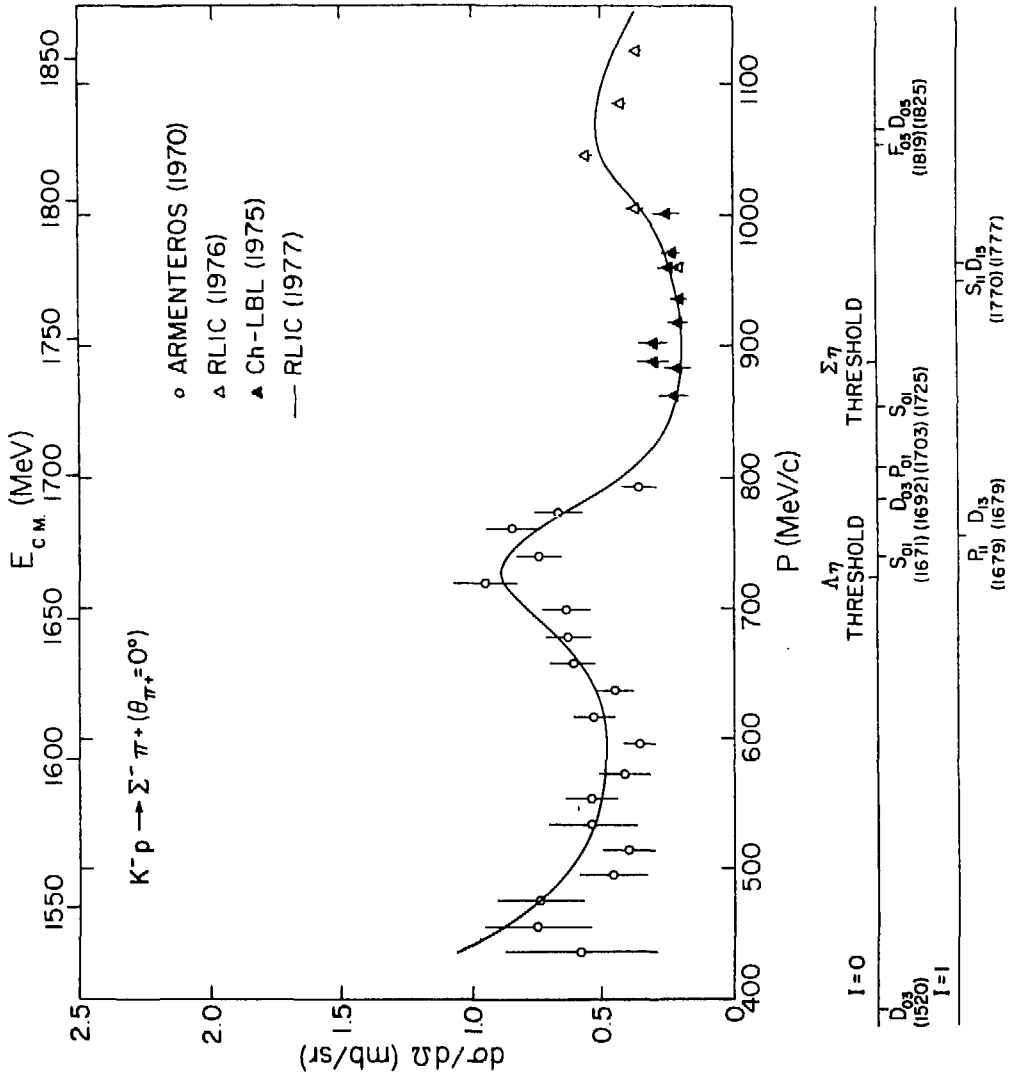


Figure 33. Previous measurements of  $\frac{d\sigma}{d\Omega} (\theta_{\pi} = 0^\circ)$  for  $K^- p \rightarrow \Sigma^- \pi^+$  (Refs. 11,13,17) and the RLIC (1977) <sup>(21)</sup> PWA fit to the data

## B. Experimental Description

The only difference in the experimental set up for  $K^-p \rightarrow \Sigma^- \pi^+$  as opposed to  $K^-p \rightarrow K^-p$  was in the timing of the final trigger coincidence,  $TR=HT' \cdot SK'$ , described in Section II.6 (see Fig. 12). Figure 12 gives the time difference between the arrival of a beam  $K^-$  at the M counter and the detection of a secondary proton or pion at the hodoscope as a function of the incident  $K^-$  momentum. For  $K^-p$  elastic scattering the width of the  $SK'$  gate was set to span the full range of proton flight times shown in the figure so as to avoid changing the fast logic timing as the momentum was changed. If the same timing scheme were used for  $K^-p \rightarrow \Sigma^- \pi^+$ , it was found experimentally that such a wide  $SK'$  gate would accept other unwanted  $HT'$  signals in addition to those from  $K^-p \rightarrow \Sigma^- \pi^+$  events. Hence the  $SK'$  gate was reduced to 12 ns and the  $HT'$  pulse to 5 ns to provide very tight timing that eliminated the undesired background. Since the flight time of pions varied by only 2 ns over the whole momentum range no adjustment of the trigger logic was required when changing momentum.

## C. Correction Factors

The analysis of the  $K^-p \rightarrow \Sigma^- \pi^+$  data proceeded in much the same fashion as described in Section III and only the differences will be explained here. The major problem in unraveling the raw data was the fact that the secondary  $\pi^+$ 's could decay while traversing the spectrometer.

Due to the small  $\pi$ - $\mu$  mass difference, forward going muons from the decay of  $0^0 \pi^+$ 's in the reaction  $K^-p \rightarrow \Sigma^- \pi^+$  fell well within the momentum acceptance of the hodoscope. Depending on the angle of decay of the  $\mu^+$  in the  $\pi^+$  center of mass and the position of the  $\pi^+$  decay in the spectrometer, muons could hit anywhere on the hodoscope, miss the hodoscope

entirely, or be lost due to scraping on the magnet apertures. To scale the number of experimentally determined events under the data peak to the number of  $\pi^+$ 's that would have hit the hodoscope had the  $\pi^+$ 's been stable, it was necessary to run two versions of the Monte Carlo program. In one version, all pions from  $K^-p \rightarrow \Sigma^- \pi^+$  were assumed to be stable. In the other version pions were allowed to decay along the spectrometer flight path and the muon's trajectory through the spectrometer was followed to see if it hit the hodoscope. Approximately 30% of the muons from the decay of  $\pi^+$ 's that would have hit the hodoscope had they been stable, were found to hit the hodoscope under the data peak.

Forward going  $\pi^+$ 's from  $K^-p \rightarrow \Sigma^- \pi^+$  were generated by the Monte Carlo in essentially the same manner as described in Appendices 3 and 4.C.1. The ratio, R, of good  $\pi^+$  events that decay to "stable"  $\pi^+$ 's that hit the hodoscope within the data peak limits was obtained from the two versions of the Monte Carlo at several momenta. Figure 34a is a plot of these results with the following fit to the momentum dependence superimposed:

$$R = 1 - \exp(-A/P_{\pi^+}) \quad (35)$$

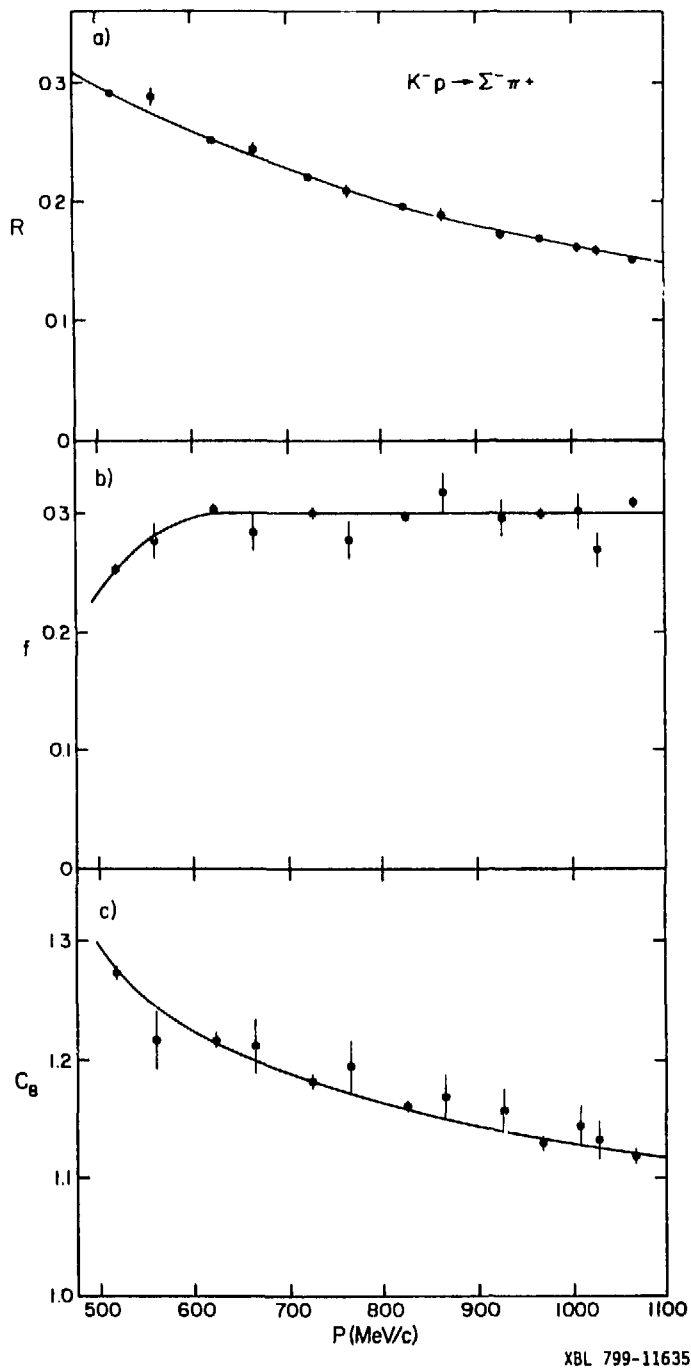
where,

$A = 148.02 \pm .47$  as determined by the fit,

$P_{\pi^+}$  = momentum of the  $0^0 \pi^+$  in  $K^-p \rightarrow \Sigma^- \pi^+$  for the given incident  $K^-$  momentum.

This form reflects the fact that fewer  $\pi^+$ 's decay along the spectrometer flight path as the momentum is increased.

The Monte Carlo also yielded the fraction, f, of muons from  $\pi^+$  decay that were actually counted as good events. The momentum dependence of f



XBL 799-11635

Figure 34. a) The ratio,  $R$ , of good  $\pi^+$  events that decay to the number of  $\pi^+$ 's that would have hit the hodoscope within the data peak limits had the  $\pi^+$ 's been stable  
 b) The fraction,  $f$ , of  $\mu$ 's from  $\pi^+$  decay that reach the hodoscope inside the elastic peak limits  
 c) Correction factor  $C_8$



is plotted in Fig. 34b and was found to be constant at 30% above 625 MeV/c. These two factors,  $R$  and  $f$ , were combined to give  $C_8$ :

$$C_8 = [1 - (1-f)R]^{-1} \quad (36)$$

The final result for  $C_8$  as a function of the incident  $K^-$  momentum is shown in Fig. 34c.

The other corrections applied to the data are described in Section III.3 and Appendix 4. Correction factors  $C_1$  through  $C_6$  are identical for  $K^-p \rightarrow \Sigma^- \pi^+$  and  $K^-p \rightarrow K^-p$  because they modify only the incident  $K^-$  flux. Factors  $C_7$  and  $C_7'$  and  $C_{10}$  which account for the absorption of  $\pi^+$  secondaries were calculated using absorption cross-sections for  $\pi^+$ 's instead of protons as in the calculation of the corresponding  $K^-p$  elastic scattering corrections. In calculating  $C_7$  the version of the Monte Carlo program in which the pions were assumed to be stable was used.

The only other correction,  $C_9$  (see Appendix 4.C.3), which allows for  $\pi^+$ 's from  $\Sigma^-$  decays traveling upstream through the  $\chi$  counter and vetoing good  $K^-p \rightarrow \Sigma^- \pi^+$  events, is found to be unity because such  $\pi^+$ 's have insufficient velocity to produce  $\chi$ erenkov light which is internally reflected in the cell. The values of the correction factors for the  $0^\circ \pi^+$  differential cross-section for the reaction  $K^-p \rightarrow \Sigma^- \pi^+$  are given in Table VI and displayed in Fig. 18 (see Section III).

#### D. Background subtraction

It will be remembered from the above discussion that the correction factor  $C_8$  accounted for the 1/3 of the  $\mu^+$ 's from the decay of the  $0^\circ \pi^+$ 's that hit the hodoscope within the limits of the data peak. The other  $\mu^+$ 's hit the iron of the spectrometer magnets, missed the hodoscope entirely, or hit the hodoscope outside the data peak on the low or high

momentum sides which were used to determine the background. For a proper evaluation of the background (using the methods described in Section III.2 and Appendix 3), it was necessary to use the Monte Carlo program to subtract the contribution to the wings of the hodoscope distributions of the  $\mu^+$ 's from the decays of forward scattered  $\pi^+$ 's before calculating the background in the data peak.

Only the reaction  $K^-p \rightarrow K_S^0 n$  followed by the decay  $K_S^0 \rightarrow \pi^+ \pi^-$  produced background pions within the momentum range accepted by the spectrometer. Monte Carlo calculations for this reaction were performed for four different values of the incident  $K^-$  momentum but, as in the  $K^-p$  backward elastic analysis, an additional background of about 4% was not accounted for. Since the  $K_S^0 \rightarrow \pi^+ \pi^-$  background was distributed uniformly over the hodoscope, it proved more convenient to estimate the total  $K^-p \rightarrow \Sigma^- \pi^+$  background using the procedure described in Section III.2 for the  $K^-p \rightarrow K^-p$  additional background. This total  $\pi^+$  background is plotted versus the incident  $K^-$  momentum in Fig. 35. The smooth curve was used to obtain the background values used in the analysis. Just as for  $K^-p \rightarrow K^-p$  the  $\pi^+$  background exhibits the same momentum dependence as the  $0^0 K^-p \rightarrow \Sigma^- \pi^+$  cross-section except above 900 MeV/c where the  $K_S^0 \rightarrow \pi^+ \pi^-$  background dominates. As noted in Section III.2 this suggests that the unexplained background may come from secondary  $\pi^+$ 's that scatter off the pole faces of D4 (the first bending magnet in the spectrometer) through the P counter and into the hodoscope. However this effect is highly model dependent and hence difficult to calculate.

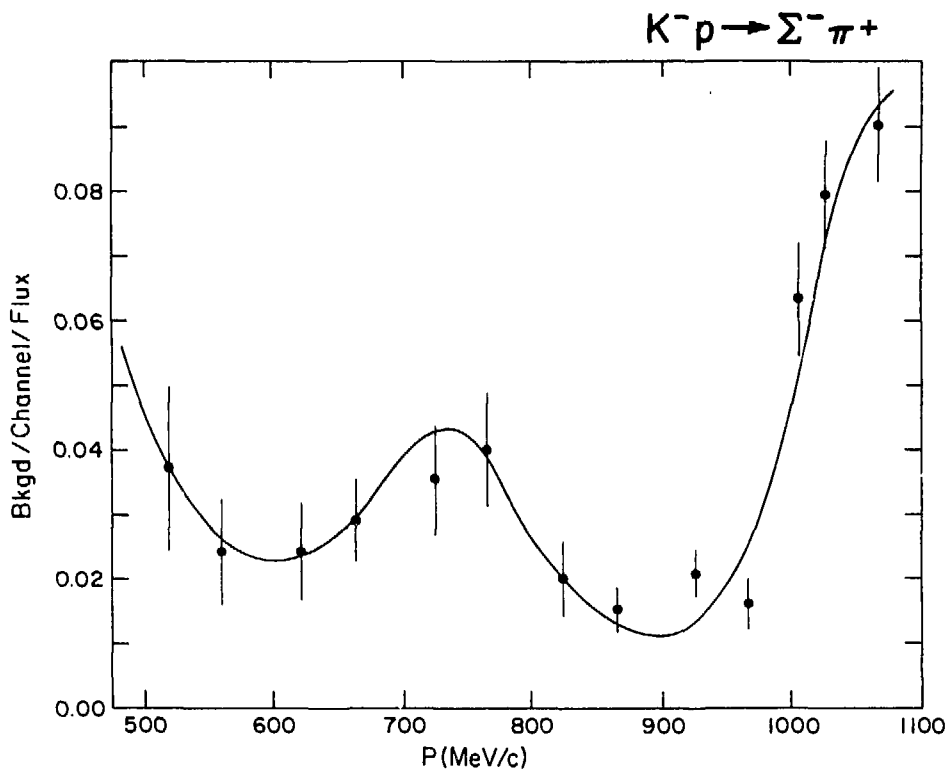


Figure 35. Total background per hodoscope channel for  $K^-p \rightarrow \Sigma^- \pi^+$  ( $\theta_{\pi^+} = 0^\circ$ ) as a function of beam momentum and normalized to  $10^6$  incident kaons

### E. Results

The final results of this measurement of forward  $\pi^+$ 's from  $K^-p \rightarrow \Sigma^- \pi^+$  are listed in Table IX and displayed in Fig. 36. Figure 37 which compares these data with previous results shows the factor of 10 statistical improvement. The new results agree very well with the RLIC partial wave analysis<sup>(21)</sup> (see Fig. 38) except for an overall normalization below 900 MeV/c. No new structure is revealed in this channel.

Table IX

Differential cross section for the reaction  $K^-p \rightarrow \Sigma^- \pi^+$  for  $\theta_\pi = 0^\circ$  in the c.m. as a function of incident  $K^-$  momentum ( $P_{K^-}$ )

$P_{K^-}$ (MeV/c)	$\frac{d\sigma}{d\Omega}(0^\circ)$ (mb/sr)	$P_{K^-}$ (MeV/c)	$\frac{d\sigma}{d\Omega}(0^\circ)$ (mb/sr)
497	$0.798 \pm 0.071$	785	$0.738 \pm 0.025$
518	$0.689 \pm 0.050$	805	$0.577 \pm 0.019$
539	$0.701 \pm 0.044$	826	$0.456 \pm 0.011$
560	$0.628 \pm 0.037$	846	$0.329 \pm 0.011$
581	$0.624 \pm 0.036$	866	$0.248 \pm 0.010$
601	$0.597 \pm 0.033$	886	$0.200 \pm 0.012$
622	$0.653 \pm 0.034$	896	$0.194 \pm 0.010$
642	$0.693 \pm 0.022$	906	$0.188 \pm 0.009$
663	$0.736 \pm 0.023$	926	$0.191 \pm 0.008$
683	$0.865 \pm 0.038$	947	$0.193 \pm 0.009$
704	$0.988 \pm 0.026$	967	$0.234 \pm 0.011$
714	$1.160 \pm 0.029$	987	$0.279 \pm 0.011$
724	$1.136 \pm 0.033$	1007	$0.310 \pm 0.015$
734	$1.160 \pm 0.034$	1029	$0.385 \pm 0.016$
745	$1.121 \pm 0.031$	1051	$0.494 \pm 0.016$
765	$1.007 \pm 0.029$	1073	$0.561 \pm 0.016$

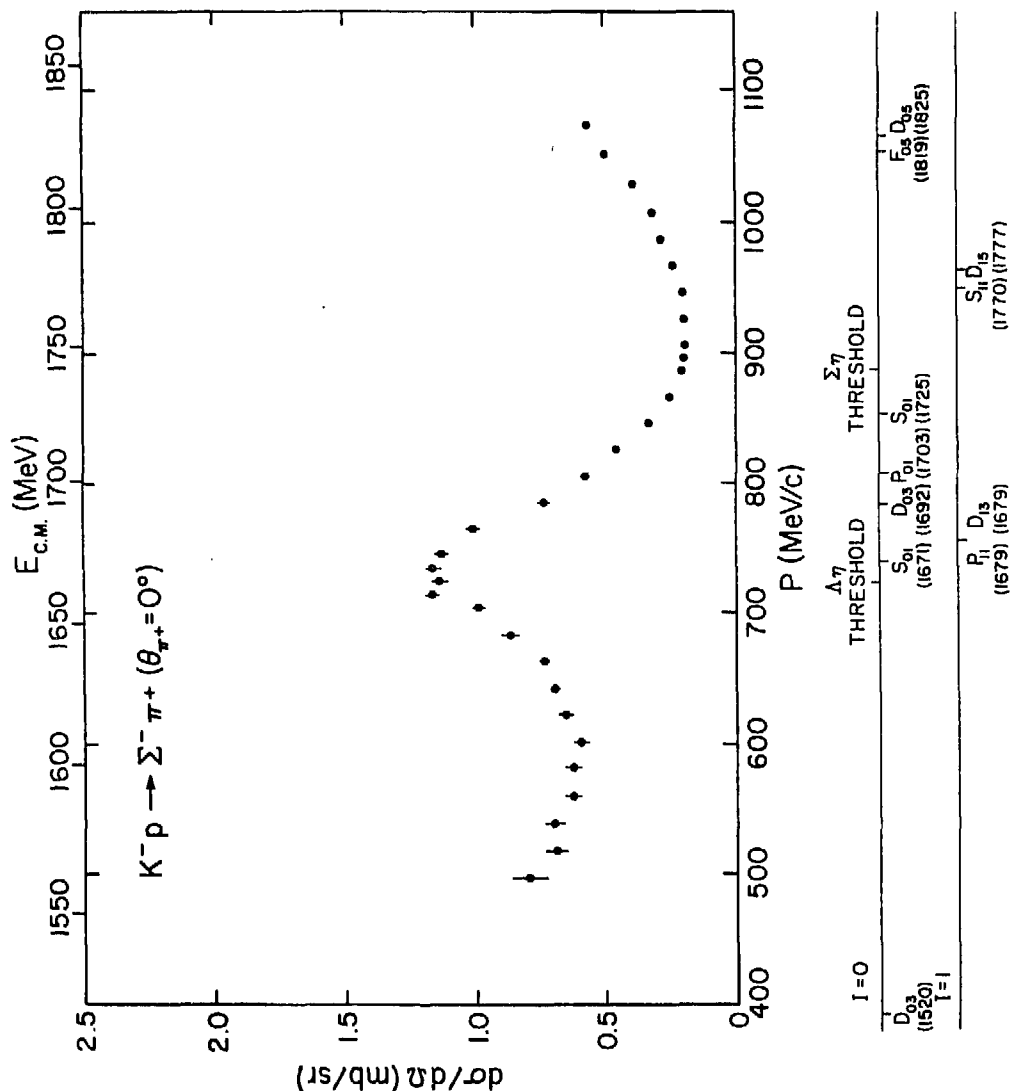


Figure 36. Results of this experiment for  $\frac{d\sigma}{d\Omega} (\theta_{\pi^+} = 0^\circ)$  for  $K^- p \rightarrow \Sigma^- \pi^+$

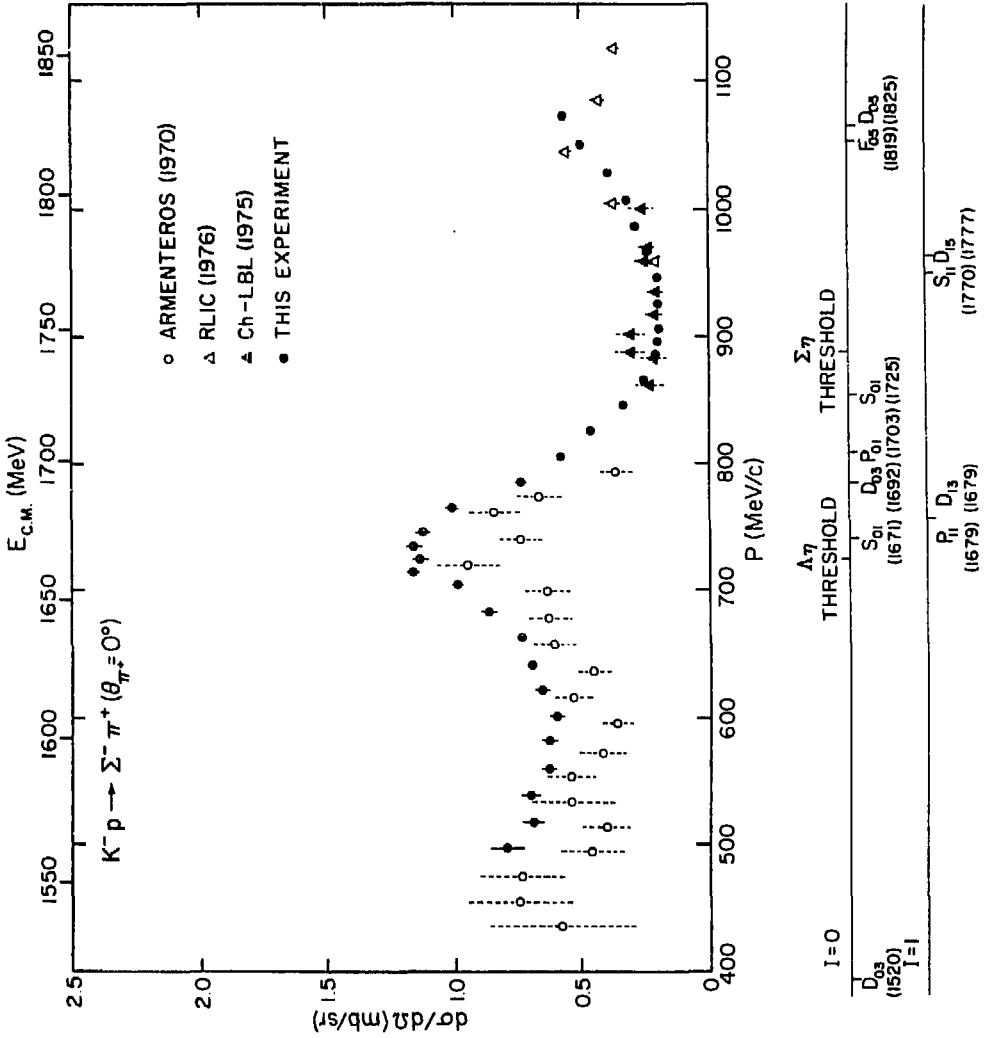


Figure 37. Comparison of  $K^-p \rightarrow \Sigma^- \pi^+ (\theta_{\pi^+} = 0^\circ)$  data from this experiment with data from previous experiments (Refs. 11,13,17)

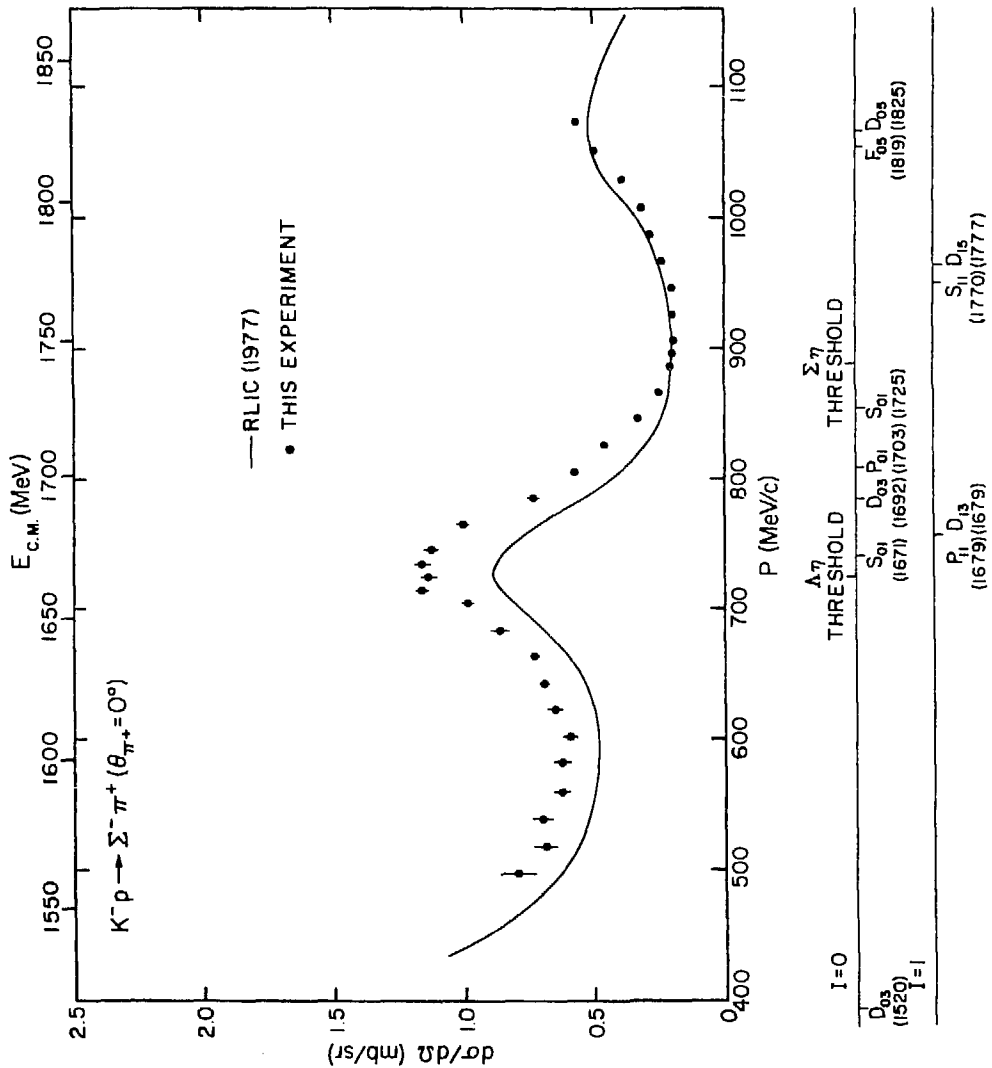


Figure 38. Comparison of  $K^- p \rightarrow \Sigma^- \pi^+ (\theta_{\pi^+} = 0^\circ)$  data from this experiment with the RLIC (1977) (21) partial wave analysis



## REFERENCES AND FOOTNOTES

1. For the purpose of classifying hadronic states in terms of the quark model it is only necessary to consider the "valence" quark composition of the hadrons. This, of course, ignores the contribution of the so-called "sea" of virtual pairs of quarks and anti-quarks which consists not only of  $\bar{u}u$  and  $d\bar{d}$  pairs but also of  $s\bar{s}$  (strange),  $c\bar{c}$  (charm),  $b\bar{b}$  (bottom), and any higher mass quarks that may exist.
2. M. Gell-Mann and Y. Ne'eman, The Eightfold Way, (Benjamin, New York, 1964).
3. Actually, in QCD the magnitude of  $\alpha_S$  depends on the square of the four momentum ( $Q^2$ ) of the gluon exchanged between two quarks. For large  $Q^2$ ,  $\alpha_S$  is small and perturbation theory is applicable. However, for the hadronic resonances considered in this thesis  $Q^2$  is small so that  $\alpha_S$  is large and one gluon exchange is no longer a good approximation.
4. R. H. Dalitz, Proc. Topical Conf. on baryon resonances, Oxford, 1976.
5. R. Tripp, "Baryon Resonances" in the Proceedings of the International School of Physics "Enrico Fermi", (1966), p. 70.
6. A. Barbaro-Galtieri, "Baryon Resonances" in Advances in Particle Physics, R. L. Cool and R. E. Marshak, Eds. (John Wiley and Sons, New York, 1968), Vol. 2, p. 175.
7. M. L. Perl, High Energy Hadron Physics, (J. Wiley & Sons, New York, 1974).
8. N. M. Queen and G. Violini, Dispersion Theory in High-Energy Physics, (J. Wiley & Sons, New York, 1974).
9. UCL: B. R. Martin and M. K. Pidcock, Nucl. Phys. B126 266 (1977).

10. See, for example: W. Kormanyos et al., Phys. Rev. Lett. 16, 709 (1966); E. Rothschild et al., Phys. Rev. D 5, 499 (1972); W. F. Baker et al., Phys. Rev. Lett. 32, 251 (1974).
11. CHS: R. Armenteros et al., Nucl. Phys. B21, 15 (1970); Ibid., B8, 233 (1968).
12. CH: B. Conforto et al., Nucl. Phys. B34, 41 (1971).
13. RLIC: B. Conforto et al., Nucl. Phys. B105, 189 (1976).
14. G. J. Adams et al., Nucl. Phys. B96, 54 (1975).
15. W. R. Holley et al., Phys. Rev. 154, 1273 (1967).
16. P. K. Caldwell et al., Phys. Rev. D 2, 1 (1970).
17. M. Jones et al., Nucl. Phys. B90, 349 (1975).
18. T. S. Mast et al., Phys. Rev. D 14, 13 (1976).
19. M. Alston-Garnjost et al., Phys. Rev. D 17, 2216 (1978).
20. M. Alston-Garnjost et al., Phys. Rev. D 17, 2226 (1978).
21. RLIC: G. P. Gopal et al., Nucl. Phys. B119, 362 (1977).
22. UCL: B. R. Martin and M. K. Pidcock, Nucl. Phys. B126, 285 (1977); Ibid., B127, 349 (1977).
23. M. Alston-Garnjost et al., Phys. Rev. D 18, 182 (1978).
24. LMMO: A. T. Lea et al., Nucl. Phys. B56, 77 (1973).
25. R. D. Ehrlich et al., Phys. Lett. 71B, 455 (1977).
26. J. Fox, BNL Accelerator Dept. EP&S Note #7 (1967).
27. J. Fox, BNL Accelerator Dept. EP&S Note #20 (1968).
28. M. Zeller, BNL Summer Study on AGS Utilization (BNL-16000), 193 (1970).
29. A. Carroll, BNL Accelerator Dept. EP&S Note #54 (1972).
30. A. Carroll, BNL Accelerator Dept. EP&S Note #64 (1973).

31. D. Pollard, Private communication.
32. CAMAC, A Modular Instrumentation System for Data Handling, AEC Report TID-25875.
33. D. Pollard, thesis, Lawrence Berkeley Laboratory Report LBL-5522 (1976), (unpublished).
34. J. Fox, EP&S Note No. 47 (1972).
35. R. J. Tapper, NIRL/R/95.
36. A. C. Paul, Lawrence Berkeley Laboratory Report LBL-2697 (1975), (unpublished).
37. S. R. Olson et al., Lawrence Berkeley Laboratory Report LBL-2445 (1973), (unpublished).
38. A. S. Carroll et al., Phys. Rev. Lett. 37, 806 (1976).
39. V. S. Barashenkov et al., Fortschr. Phys. 17, 683 (1969).
40. H. Nicholson and R. Kenney, Private communication.
41. K. L. Brown, Stanford Linear Accelerator Center Report No. 75 (1967).
42. E. Bracci et al., CERN/HERA 72-1 (1972).
43. E. Bracci et al, CERN/HERA 73-1 (1973).
44. R. J. Abrams et al., Phys. Rev. D 4, 3235 (1971).
45. E. Bracci et al., et al., CERN/HERA 72-2 (1972).
46. Digital Equipment Corporation, Maynard, Mass.
47. The original idea for the multi-task system described here came from C. McParland, Private communication.